REPORT DOCUMENTATION PAGE

1. AGENCY USE ONLY (Leave blank)	2. REPORT DATE Sep 95	3. REPORT TYPE AND DATES COVERED

4. TITLE AND SUBTITLE
The Nearly Instantaneous Global Pattern of Auroral
Electron Precipitation For AE 100 nT

5. FUNDING NUMBERS

6. AUTHOR(S)

David W. Hembroff

7. PERFORMING ORGANIZATION NAME(S) AND ADDRESS(ES)

AFIT Student Attending:

University of Alaska Fairbanks

8. PERFORMING ORGANIZATION REPORT NUMBER

96-012

9. SPONSORING/MONITORING AGENCY NAME(S) AND ADDRESS(ES)

DEPARTMENT OF THE AIR FORCE
AFIT/CI
2950 P STREET, BLDG 125
WRIGHT-PATTERSON AFB OH 45433-7765

10. SPONSORING/MONITORING AGENCY REPORT NUMBER

11. SUPPLEMENTARY NOTES

12a. DISTRIBUTION/AVAILABILITY STATEMENT

Approved for Public Release IAW AFR 190-1
Distribution Unlimited
BRIAN D. GAUTHIER, MSgt, USAF
Chief Administration

12b. DISTRIBUTION CODE

13. ABSTRACT (Maximum 200 words)

19960531 083

14. SUBJECT TERMS			15. NUMBER OF PAGES 112
			16. PRICE CODE

17. SECURITY CLASSIFICATION OF REPORT	18. SECURITY CLASSIFICATION OF THIS PAGE	19. SECURITY CLASSIFICATION OF ABSTRACT	20. LIMITATION OF ABSTRACT

GENERAL INSTRUCTIONS FOR COMPLETING SF 298

The Report Documentation Page (RDP) is used in announcing and cataloging reports. It is important that this information be consistent with the rest of the report, particularly the cover and title page. Instructions for filling in each block of the form follow. It is important to *stay within the lines* to meet *optical scanning requirements*.

Block 1. Agency Use Only *(Leave blank).*

Block 2. Report Date. Full publication date including day, month, and year, if available (e.g. 1 Jan 88). Must cite at least the year.

Block 3. Type of Report and Dates Covered. State whether report is interim, final, etc. If applicable, enter inclusive report dates (e.g. 10 Jun 87 - 30 Jun 88).

Block 4. Title and Subtitle. A title is taken from the part of the report that provides the most meaningful and complete information. When a report is prepared in more than one volume, repeat the primary title, add volume number, and include subtitle for the specific volume. On classified documents enter the title classification in parentheses.

Block 5. Funding Numbers. To include contract and grant numbers; may include program element number(s), project number(s), task number(s), and work unit number(s). Use the following labels:

C	-	Contract	PR -	Project
G	-	Grant	TA -	Task
PE	-	Program Element	WU -	Work Unit Accession No.

Block 6. Author(s). Name(s) of person(s) responsible for writing the report, performing the research, or credited with the content of the report. If editor or compiler, this should follow the name(s).

Block 7. Performing Organization Name(s) and Address(es). Self-explanatory.

Block 8. Performing Organization Report Number. Enter the unique alphanumeric report number(s) assigned by the organization performing the report.

Block 9. Sponsoring/Monitoring Agency Name(s) and Address(es). Self-explanatory.

Block 10. Sponsoring/Monitoring Agency Report Number. *(If known)*

Block 11. Supplementary Notes. Enter information not included elsewhere such as: Prepared in cooperation with...; Trans. of...; To be published in.... When a report is revised, include a statement whether the new report supersedes or supplements the older report.

Block 12a. Distribution/Availability Statement. Denotes public availability or limitations. Cite any availability to the public. Enter additional limitations or special markings in all capitals (e.g. NOFORN, REL, ITAR).

DOD	-	See DoDD 5230.24, "Distribution Statements on Technical Documents."
DOE	-	See authorities.
NASA	-	See Handbook NHB 2200.2.
NTIS	-	Leave blank.

Block 12b. Distribution Code.

DOD	-	Leave blank.
DOE	-	Enter DOE distribution categories from the Standard Distribution for Unclassified Scientific and Technical Reports.
NASA	-	Leave blank.
NTIS	-	Leave blank.

Block 13. Abstract. Include a brief *(Maximum 200 words)* factual summary of the most significant information contained in the report.

**Block 14.** Subject Terms. Keywords or phrases identifying major subjects in the report.

Block 15. Number of Pages. Enter the total number of pages.

Block 16. Price Code. Enter appropriate price code *(NTIS only).*

Blocks 17. - 19. Security Classifications. Self-explanatory. Enter U.S. Security Classification in accordance with U.S. Security Regulations (i.e., UNCLASSIFIED). If form contains classified information, stamp classification on the top and bottom of the page.

Block 20. Limitation of Abstract. This block must be completed to assign a limitation to the abstract. Enter either UL (unlimited) or SAR (same as report). An entry in this block is necessary if the abstract is to be limited. If blank, the abstract is assumed to be unlimited.

DISCLAIMER NOTICE
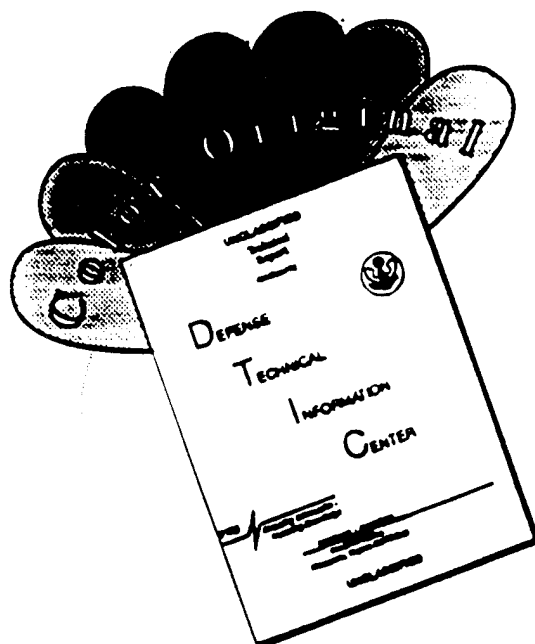
THIS DOCUMENT IS BEST QUALITY AVAILABLE. THE COPY FURNISHED TO DTIC CONTAINED A SIGNIFICANT NUMBER OF COLOR PAGES WHICH DO NOT REPRODUCE LEGIBLY ON BLACK AND WHITE MICROFICHE.

DISCLAIMER NOTICE
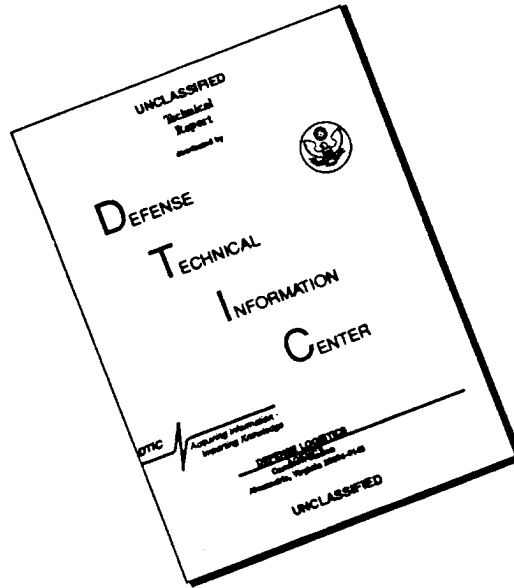
THIS DOCUMENT IS BEST QUALITY AVAILABLE. THE COPY FURNISHED TO DTIC CONTAINED A SIGNIFICANT NUMBER OF PAGES WHICH DO NOT REPRODUCE LEGIBLY.

THE NEARLY INSTANTANEOUS GLOBAL PATTERN OF AURORAL

ELECTRON PRECIPITATION FOR AE < 100 nT

By

David W. Hembroff

RECOMMENDED:

_____
Committee Member

_____
Committee Member
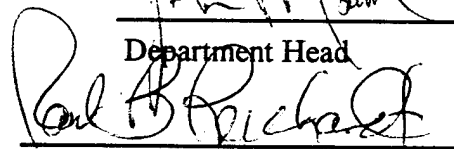
_____
Committee Member

_____
Committee Chair

_____
Department Head
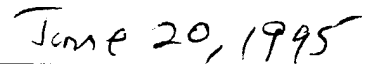
APPROVED:

_____
Dean, College of Natural Sciences

_____
Dean of the Graduate School

_____
June 20, 1995
Date

THE NEARLY INSTANTANEOUS GLOBAL PATTERN OF AURORAL

ELECTRON PRECIPITATION FOR AE < 100 nT

A

THESIS

Presented to the Faculty

of the University of Alaska Fairbanks

in Partial Fulfillment of the Requirements

for the Degree of

MASTER OF SCIENCE

By

David W. Hembroff, B.S.

Fairbanks, Alaska

September, 1995

ABSTRACT

The nearly instantaneous global pattern of the auroral electron precipitation is determined for quiet periods using auroral images from the spacecraft Dynamics Explorer 1. The use of global-scale images to determine these patterns provides improved temporal and two-dimensional spatial resolution not possible with highly localized and less frequent *in situ* particle measurements made with low-altitude, polar-orbiting spacecraft. The analysis is of far-ultraviolet images at wavelengths 120-160 nm obtained during periods when the magnetic index AE is less than 100 nT and decreasing with time. The orientation of the interplanetary magnetic field is also considered in this analysis. Analysis of the patterns for magnetically quiet intervals is a necessary first step in determining the global precipitation pattern for the growth, expansion, and recovery phases of auroral substorms. These nearly instantaneous patterns will provide improved estimates of the energy input on a global scale for investigations of thermospheric storms and related aeronomic phenomena by other researchers.

TABLE OF CONTENTS

LIST OF FIGURES

LIST OF TABLES

LIST OF APPENDICES

ACKNOWLEDGMENTS

I would like to thank John D. Craven, my thesis advisor and committee chairman, for the many comments, suggestions, and inputs to my research and graduate study. I am also very appreciative to the other members of my committee, John V. Olson, Thomas J. Hallinan and Hans C. Stenbaek-Nielsen, for their comments and suggestions.

"...all the wealth that comes from the full assurance of understanding, resulting in a true knowledge of God's mystery, that is, Christ Himself..." Col 2:2; NAS.

CHAPTER 1

INTRODUCTION AND PREVIOUS WORK

Introduction

Since man first set eyes on the aurora he has been trying to explain its origin. Early man explained the aurora with gods and demons, and even today some native children are told that the aurora snatches bad little children like the bogeyman [Davis, 1992]. Numerous other explanations have been put forth by scholars for the lights in the night sky. As late as the early and middle 1700s several theories were put forth explaining that the aurora was caused by sunlight reflecting from ice on the Arctic ocean or from ice crystals in the Earth's atmosphere [Eather, 1980]. More plausible theories came about as man gained a better understanding of the world around him. Summaries of the history of auroral lore and knowledge have been compiled by many authors (e.g., Eather [1980], Davis [1992], and Stringer and Schreurs [1975]). Highlights are given in this introduction.

In 1774, Jean Jaques Dortous de Mairan of France first related the aurora to solar activity. Sweden's Anders Jonas Angstrom showed, through the use of a prism, in 1868, that auroral light differs from sunlight. In 1910, Carl Störmer used triangulation to measure the height of the aurora, showing the aurora to be much higher in the atmosphere than was earlier believed. He found the lower border of the aurora to be at an average height of 110 km, that it is rarely seen below 90 km, and it could occur as high as 250 km

1

[Eather, 1980]. Measurements made in 1930 by Veryl Fuller then showed that auroras occur at the same altitudes all along the auroral zone [Stringer and Schreurs, 1975].

Extensive studies of the aurora took place during the International Geophysical Year (IGY) of 1957 and 1958. All-sky camera networks simultaneously recorded auroral displays throughout the high-latitude northern hemisphere to form some of the first large-scale continuous images of the auroral oval at various levels of activity [Eather, 1980]. Data from the IGY led to a new and better understanding of the aurora, and to more and improved experimental techniques to measure the auroral phenomena. Since then, advances in computer technology, spacecraft measurements (both *in situ* and remote) and other observation techniques have supported new and better theories and models of the aurora [Stringer and Schreurs, 1975].

One of the simplest physical systems used today as an analogy with which to explain the aurora is a television set. The system that generates the aurora is said to be like a gigantic picture tube with particles that are released by the Sun streaming outwards toward the Earth -- the solar wind. The Earth's magnetic field, interacting with the interplanetary magnetic field (IMF) from the Sun, works to focus and direct the solar particles into narrow 'beams' that impact the Earth's upper atmosphere. This in turn acts like the screen, to create the phenomenon we call the aurora [Davis, 1992]. The mechanism of acceleration near the Earth is not well understood. This analogy works well as far as it goes, but implies that the 'screen', the upper atmosphere, is flat and unchanging.

We know that the particles don't just stream directly from the Sun into the Earth's upper atmosphere. The Earth's magnetosphere acts like a filter, amplifier and a focusing device for the particles. The number of particles that reach the upper atmosphere is dependent on the solar activity, the state of the magnetosphere, and the energies of the particles. The particles that enter the Earth's upper atmosphere and that are responsible

for the aurora range in energy from a few electron volts (eV) to several hundred kiloelectron volts (keV). Particles that meet or exceed a given energy threshold excite specific constituents of the atmosphere. From these particle-constituent interactions light at specific wavelengths is radiated as the constituents return to their ground states. The wavelength of an emission is directly related to the atomic structure of the constituent and the distribution of wavelengths in the aurora is related to the average energies of the particles and composition of the atmosphere [Rees, 1989]. By monitoring the auroral emissions one can estimate the amount of energy being deposited in the upper atmosphere by the energetic particles.

The Ionosphere

The upper atmosphere is not simply a flat screen like that of a television set, but has both depth and structure. Figure 1.1 shows schematically the average structure of the Earth's atmosphere for temperature, and for ion and neutral densities [Rees, 1989]. The major molecular constituents of the upper atmosphere are N_2 and O_2. The major atomic constituent is O, produced mainly through the dissociation of O_2 by solar UV photons and energetic particle impact [Rees, 1989]. Below about 150 km, N_2 and O_2 are the dominant species. With further increase in altitude, atomic oxygen becomes more prominent than the O_2, and then above 200 to 250 km atomic oxygen becomes the dominant constituent. These general transitions of the number densities for the dominant upper atmosphere constituents are for a model atmosphere. The precise number densities and atmospheric profiles vary considerably.

A plot of ion density verses altitude shows a different vertical structure to the atmosphere that is also of importance to the auroral researcher. Although a qualitative summary, the region defined as the ionosphere becomes apparent in Figure 1.1. A more
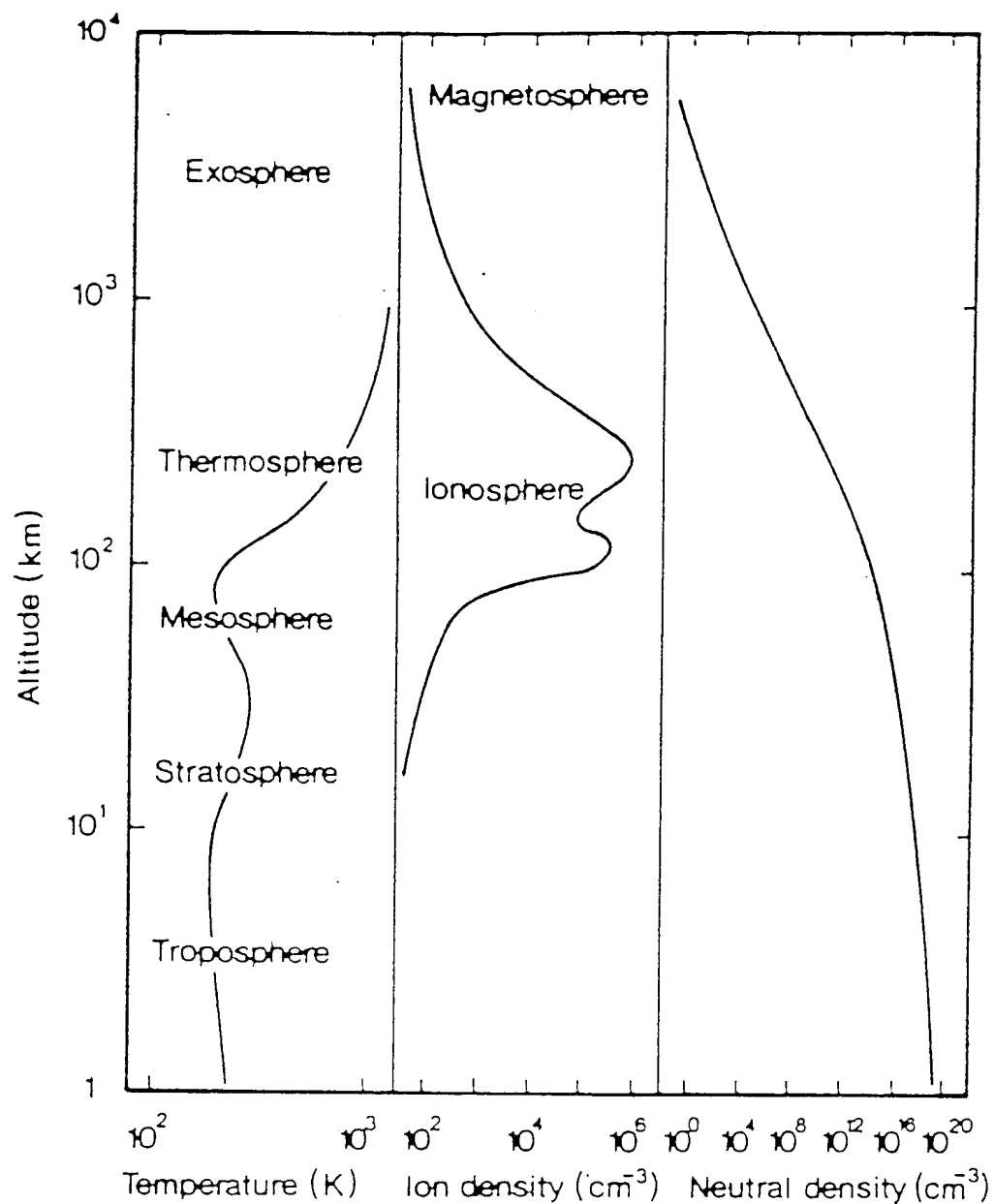
Figure 1.1 Schematic representation of the thermal structure, the ion density and the neutral density of the Earth's atmosphere. The approximate altitude regimes of various named regions are indicated. [Rees, 1989]

exacting profile of the ionosphere can be found by plotting the electron density verses altitude. Such a plot is seen in Figure 1.2 [Wallace and Hobbs, 1977].

From Figure 1.2 we can see that the electron density increases rapidly above an altitude of about 85 km to a peak at between 250 and 300 km. The irregularities in the plot are labeled the D and E regions of the ionosphere. These regions have a strong diurnal dependence as seen in Figure 1.2, with most of the electrons recombining with positive ions in the nightside of the ionosphere [Wallace and Hobbs, 1977]. This shows that these regions are strongly dependent on solar photoionization as the source of their free electrons. These diurnal effects are due to recombination of photoionized atmospheric constituents. Recombination rates are highly dependent on the rates of collision. In the E region, atmospheric density is such that the collision rate is high and therefore the recombination rate is high. Thus when the E region is no longer exposed to sunlight the rate of recombination dominates and the electron density decreases rapidly. Although the F region is also solar produced, its diurnal variability is weaker than that of the E region because the atmospheric density is low and hence the collision rate is low. The diurnal variations are often masked by other fluctuations in the electron density. These non-diurnal fluctuations are caused by phenomena other than direct solar photoionization. It must be noted here that these profiles presented in Figure 1.1 and 1.2 are of the mean ionosphere. There are latitudinal, seasonal, and other variations that occur in the ionosphere on many different time scales. The instantaneous profile of the ionosphere, when measured, may be drastically different from the mean view at any given time and latitude.

One source of electron density fluctuations in the F region is energetic particle interactions with the neutral and ionic constituents of the upper atmosphere. This precipitation of energetic magnetospheric particles into the ionosphere at high latitudes is
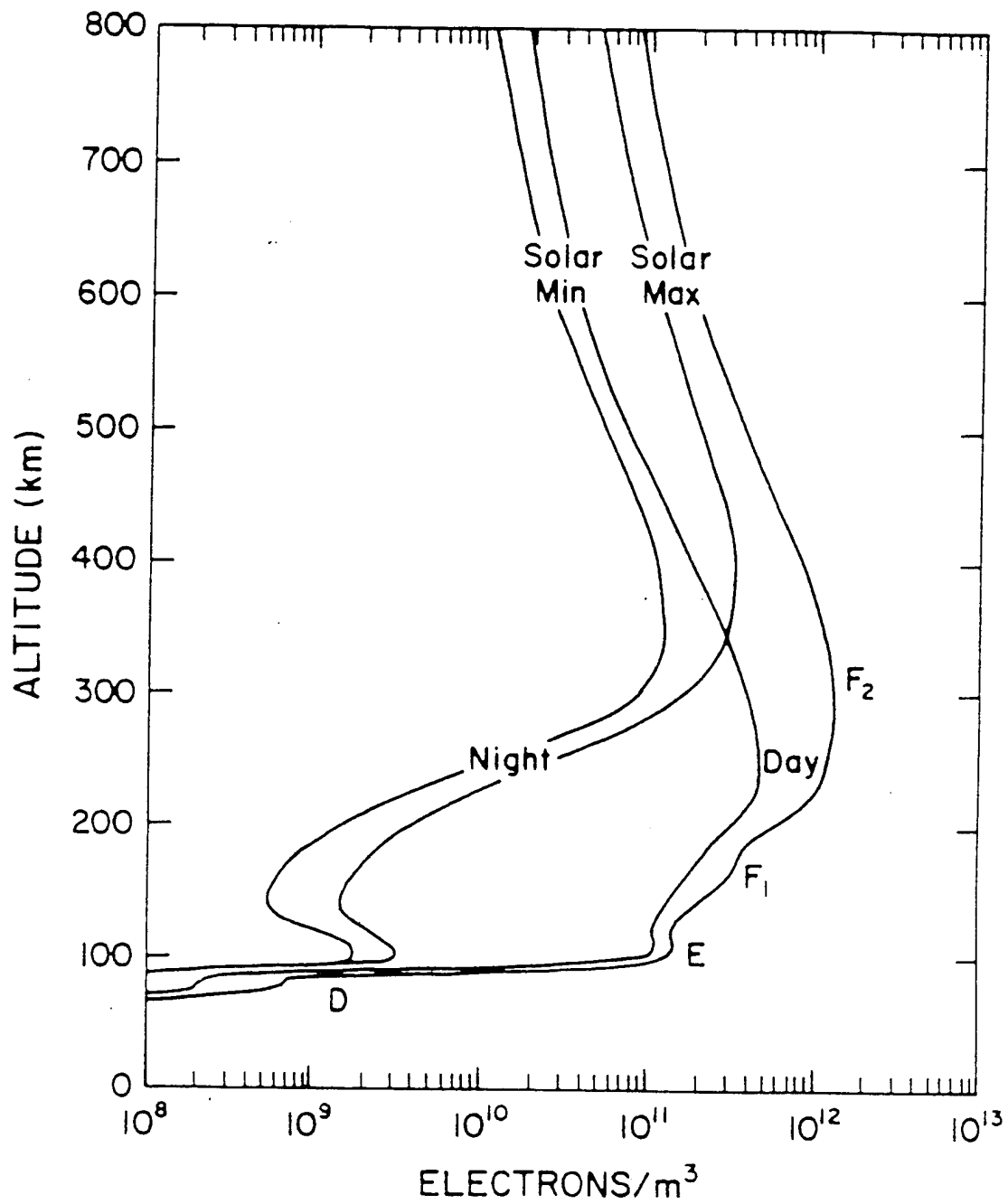
Figure 1.2 Typical mid-latitude electron density profiles for sunspot maximum and minimum, day and night. Different regions of the ionosphere are labelled D, E, F1, and F2. [Wallace and Hobbs, 1977]

the source of auroral emissions [Eather, 1980]. Such interactions are not exclusive to the F-region altitudes, with higher energy particles penetrating deeper into the atmosphere. Figure 1.3 shows the volume emission rate for the OI triplet at about 130.4 nm, in the far ultraviolet (FUV), as created by precipitating electrons from three assumed Maxwellian distributions. Characteristic energies of the distributions are E_0 = 0.1, 1 and 6 keV. Note that the lower boundary of penetration for the 0.1-keV electrons is at about 150 km, while the lower boundaries for the 1- and 6-keV electrons are 100 and 90 km, respectively. A major feature that one should see in Figure 1.3 is that there appears to be a lower altitude limit to the penetration of the energetic particles. For the higher energy particles the emission rate profiles with respect to altitude are similar. The lower limit may reach 85 km, with a peak in the rate near the base of the profile, and the rate decreases exponentially with increasing altitude. While Figure 1.3 is concerned with only one particular wavelength of auroral emissions, qualitatively similar results are obtained for emissions at other wavelengths. Such profiles give us a cross-sectional region of the upper atmosphere to which we can confine our investigation, generally above 85 km.

The spectrum of auroral emissions ranges from the infrared to the extreme ultraviolet and x-ray bands. Figure 1.4 shows a small portion of the auroral emission spectrum from 117.5 to 152.5 nm. This spectrum was recorded with a rocket-borne photometer at altitudes of 160-180 km [Feldman and Gentieu, 1982]. While Figure 1.4 is the spectrum for one particular aurora, it is typical of most auroral emissions in this particular range of wavelengths. Specific emissions detected by instruments are determined by the energy and type of the precipitating particle and the atmospheric constituents with which the particle interacts. Many ground-based all-sky cameras use filters in the visible region of the spectrum. Spacecraft may carry several
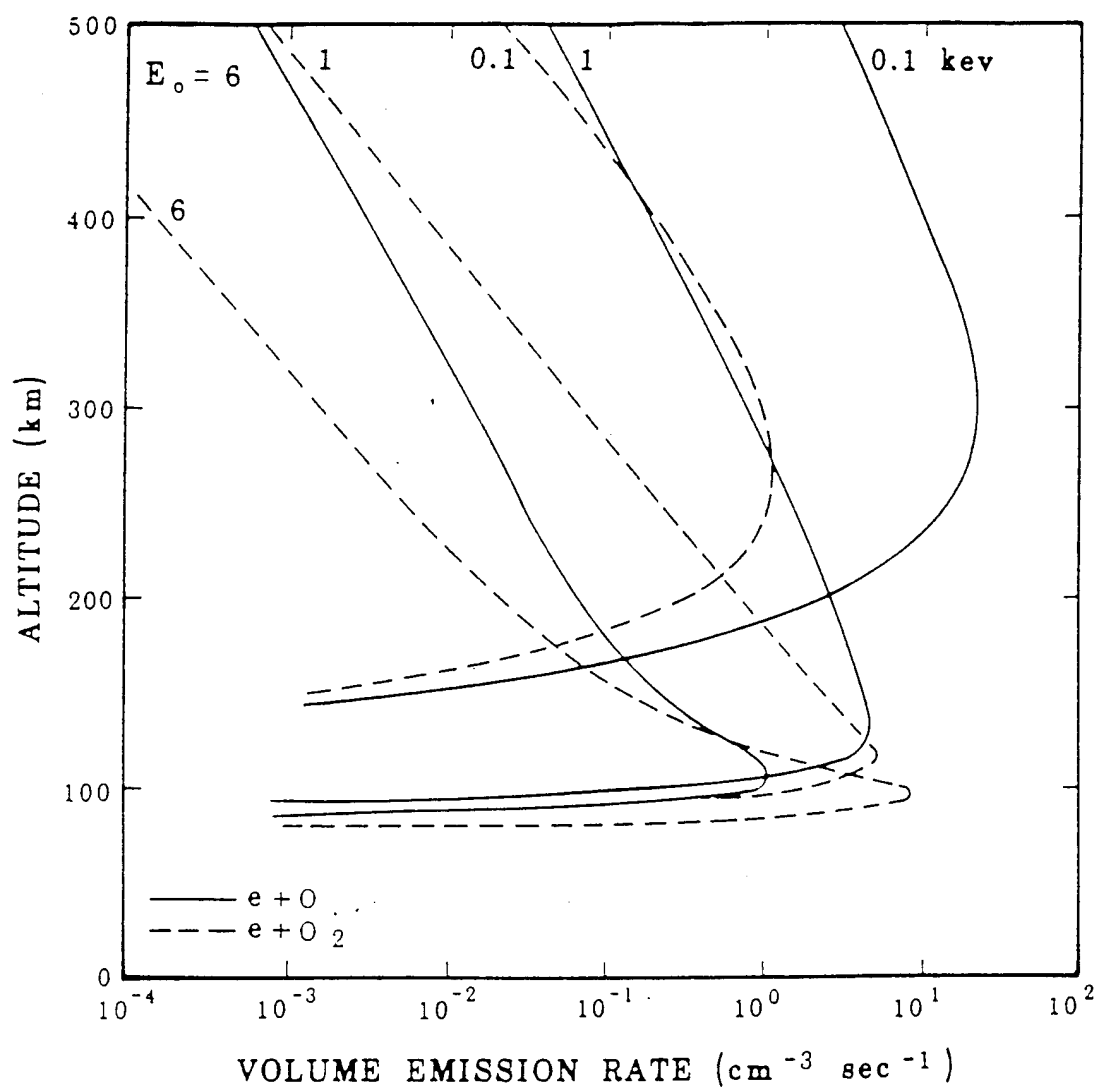
Figure 1.3   Volume emission rate of the OI(130.4 nm) triplet produced by electron impact excitation of atomic oxygen and dissociative excitation of molecular oxygen. Altitude profiles are shown for three isotropic Maxwellian electron spectra with characteristic energies of 0.1, 1, and 6 keV. [Lummerzheim et al., 1991]
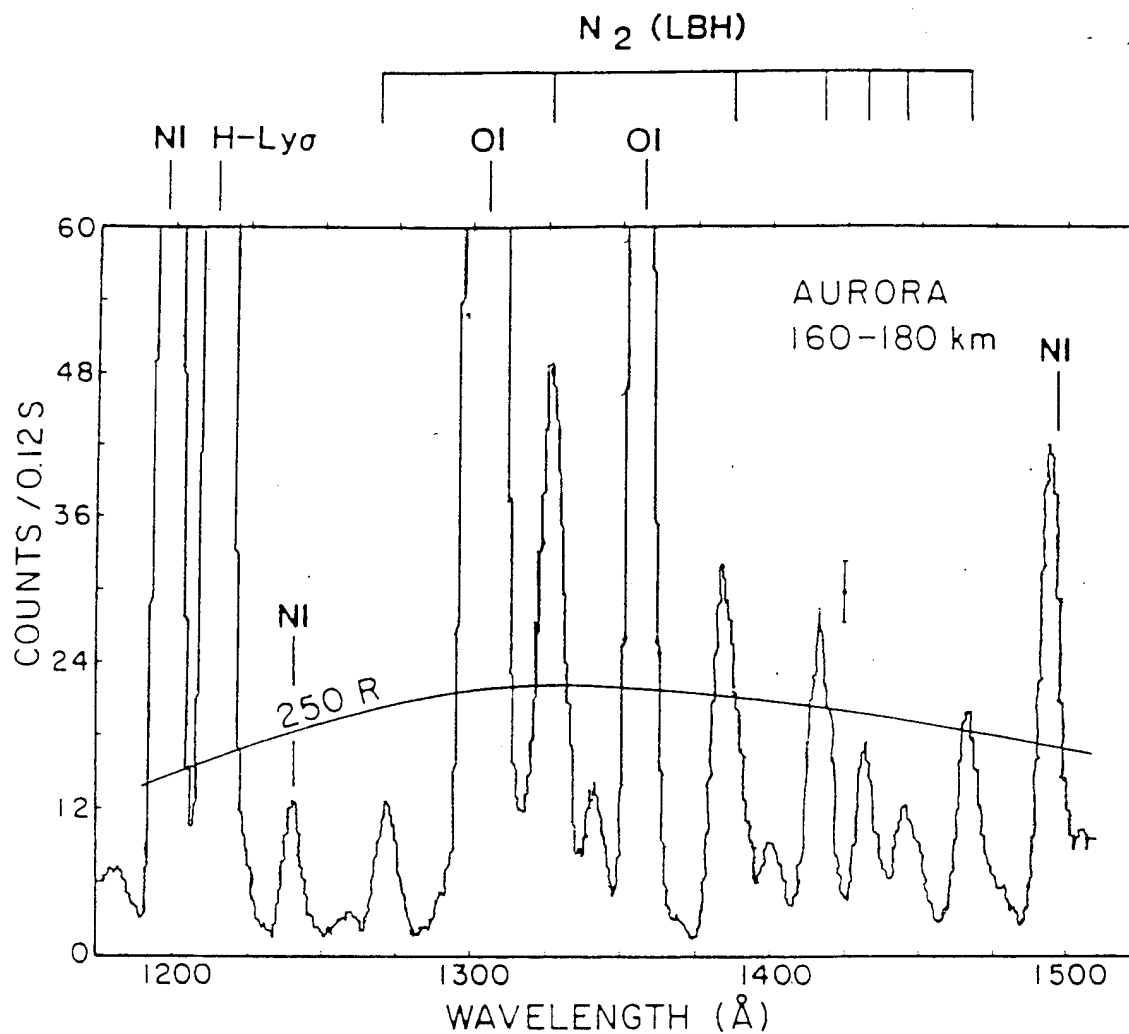
Figure 1.4 Typical auroral spectrum in the wavelength interval 117.5 to 152.5 nm aquired with a rocket-borne spectrometer in the altitude range from 160 to 180 km [Feldman and Gentieu, 1982]. The principal emission features are identified. A contour of a constant emission rate (250 R) is shown.

types of detectors with numerous filters and will generally sample the spectrum over a region that is of particular interest to the researcher.

This research will concentrate on the observations of auroral emissions at FUV wavelengths ranging from 123-160 nm, as shown in Figure 1.4. We can see from this figure that the focus is on emissions from electron interactions with NI, OI, and N_2(LBH). The relative importance of the contributions will be discussed later.

Auroral Emissions

It has been shown that of the precipitating particles reaching the lower thermosphere, electrons contribute the majority of the energy input into the auroral oval [Hardy *et al.*, 1985]. Nearly all emissions of interest to this research are the result of the precipitation of electrons with energies ranging from 0.05 to 10 keV [Lummerzheim, 1991]. In general the type of electron-constituent interactions responsible for the emissions are,

$$e_p + A, AB \rightarrow e_p + A^{+*}, AB^{+*} + e_s \qquad (1)$$

$$e_p + AB \rightarrow e_p + A^{+*} + B^* + e_s \qquad (2)$$

$$e_p + AB \rightarrow e_p + A^* + B^* \qquad (3)$$

$$e_s + A, AB \rightarrow e_s + A^*, AB^* \qquad (4)$$
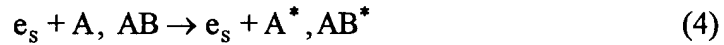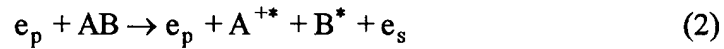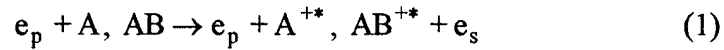
where A denotes atomic species and AB denotes molecular species and e_p and e_s are, respectively, the primary precipitating electrons and resulting secondary electrons created in the interaction [Rees, 1989]. An asterisk denotes the formation of an excited state.

Equation (1) describes ionization excitation, equation (2) dissociative ionization excitation, (3) dissociative excitation, and (4) excitation from secondary electrons [Rees, 1989]. Emission rates for the various electron-constituent interactions are altitude dependent since both the relative density of a given atmospheric constituent and the energy of a precipitating particle are altitude dependent. The precipitating particle spectra and the relative density of atomic oxygen are combined in Figure 1.3 to show that many of the OI emissions at 130.4 nm occur from 85 to 200 km. Emissions of present interest for NI, HI, N_2(LBH) and OI are summarized in Table 1.1. The relative importance of each will be covered in Chapter 2.

Table 1.1. Auroral emissions of interest to this research, wavelength in nm [Meier and Strickland, 1991].

Species		Wavlength (nm)
NI		149.3
HI		121.6
N_2(LBH)		125.9, 127.3, 129.8, 132.5, 135.4, 138.4, 139.8, 141.6, 143.1,
		144.6, 146.5,149.5, 151.1, 153.1, 155.8, 158.6, 160.2
OI		130.4, 135.6

These interactions and their emissions have been extensively studied in the laboratory and the field [Rees, 1989]. The threshold energy a particle needs when colliding with a specific constituent causing it to radiate at a particular wavelength is well

established. Using this foundation one can work in the reverse: By observing ratios of particular emissions in the auroral oval, one can determine principle features of the energy spectrum of the precipitating particles. An example of this is given by Rees and Luckey [1974] for emissions at visible wavelengths.

Previous Research

Much of the previous research on global patterns of energetic particle precipitation has been achieved through the analysis of ground-based or low-altitude spacecraft observations. This is somewhat analogous to someone watching a twenty-inch television screen from the distance of about one inch. While the viewer has an excellent perspective of that part of the screen in his field of vision, he can look at the different parts of the screen sequentially and assume that everything on the TV screen is constant and stationary, or he can take long-term statistical averages of the brightness patterns on the screen and assume that these averages will represent the TV program. In the case of the auroral oval, the screen typically covers the Arctic or Antarctic polar region from about ± 60° latitude to the poles, or an area of about 35×10^6 km^2 [Gorney, 1991]. The field of view of an all-sky camera covers a region about the size of Alaska at best, or 1.5×10^6 km^2. A low-altitude spacecraft can only sample a thin slice of this region in each orbit. Figure 1.5 shows a typical false color image of a Dynamic Explorer far-ultraviolet image of the aurora. The bright yellow region in the upper left of the image is due to the dayglow emissions in the sunlit hemisphere. The Sun is toward the upper left. The remaining principle directions are : midnight to the lower right (the broad region of the oval); 0600 magnetic local time to the upper right; and 1800 MLT towards the lower left. The circle centered at about 1000 MLT outlines the field of view at auroral emission altitudes of a ground based all-sky camera [Craven, personal communication, 1994].
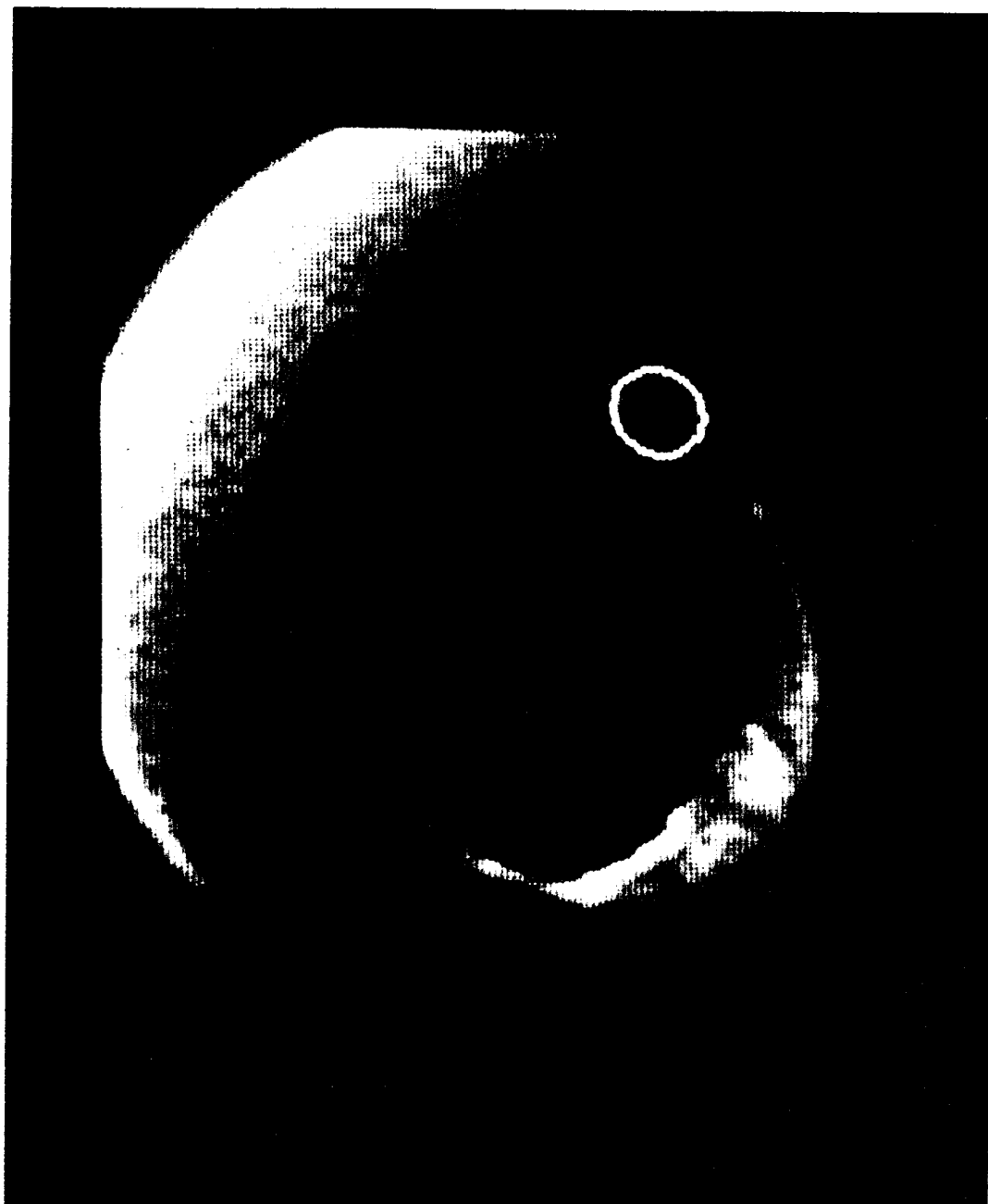
Figure 1.5 False-color image of the auroral oval in the far-ultraviolet region of the spectrum. The sun is to the upper-left of the image. The overlayed circle in the morning sector represents the field of view of a ground-based all-sky camera.

The aurora is very dynamic, with structural changes occurring in the span of seconds, minutes and hours [Akasofu, 1991, 1968, 1964], and with many of these changes occurring in an organized pattern and morphology first identified by S.-I. Akasofu [1964] as an auroral substorm. A typical auroral substorm is first indicated by a sudden brightening of the aurora in the midnight or late evening sector [e.g., Akasofu, 1964, 1968, 1991; Rostoker, 1991]. If a low-altitude spacecraft is not in the proper place at the proper time it may not detect this sudden change in auroral activity.

After substorm onset the auroral brightening spreads rapidly along the auroral oval in what is known as the westward and eastward surges. This occurs in a matter of several minutes to tens of minutes and the entire oval in the nightside becomes bright [Akasofu, 1968]. The oval also expands poleward and equatorward, begins to break up into many bright patches, and then fades and returns to its original state. This entire process from onset to recovery can take as little as 30 minutes or as long as several hours.

One can avoid making too large an inference about the overall auroral distribution by taking many measurements over the entire region of interest. This can be done by linking many observers together as was done with the network of all-sky cameras used for IGY. But this may still leave gaps due to weather or to auroral activity that moves the aurora out of the field of view. It is too expensive to place such all-sky cameras in all regions of interest. Another approach is to make many measurements over a given period of time and create a statistical model of the region of interest.

This last method has been used by many researchers. Of interest to this research is the work done by Hardy *et al.* [1985] and Spiro *et al.* [1982] with particle detectors aboard several low-altitude, polar orbiting spacecraft platforms. Hardy *et al.* made use of DMSP F2 and F4, and STP P78-1, while Spiro *et al.* used observations from Atmospheric Explorers C and D. Their approaches to finding the large-scale pattern of auroral electron

precipitation was to use a large data set of electron energy spectra sampled *in situ*. These data sets were subdivided into groups identified by the magnitude of the Kp or AE magnetic indices at the time of measurement. But according to Holzworth and Meng [1975], spacecraft particle measurements are point measurements in space and time and thus cannot sample the entire auroral oval at any given time.

Although, such research uses large data sets, (e.g., Hardy *et al.* [1985] used 13.6 million spectra, with the measurements taken over a 15-month period), this type of statistical averaging washes out any small- to medium-scale spatial and temporal variations. Knowing the time and spatial scales of auroral activity and comparing them to the periods over which Hardy *et al.* and Spiro *et al.* averaged, the loss of temporal and spatial resolution is easily seen. Typically, a low-altitude spacecraft passes through one auroral region less than once every 90 minutes, so any 'image' or global pattern of the auroral oval needs to be a composite of several orbital passes over several hours, days, or months (as done by Hardy *et al.* and Spiro *et al.*). This knowledge leads an investigator to seek an improved method of evaluating the global pattern of auroral particle precipitation.

Dynamics Explorer 1

The time scale and spatial distribution of a typical auroral substorm are so dissimilar to the sampling capabilities of single low-altitude spacecraft that there is a need for a higher resolution model for the energy deposition associated with auroral activity. The Dynamic Explorer 1 (DE 1) images in the visible and far ultraviolet (FUV) wavelengths provide that increased resolution in both time and space over ground-based and *in situ* representations of the entire auroral oval. With this increased resolution and large database of images over a wide range of magnetospheric activity, one should be able to

establish an improved model of auroral electron energy deposition versus geomagnetic activity.

Much work has been done with global spacecraft images in the visible and ultraviolet regions of the spectrum [Rees *et al.*, 1988]. Rees and Luckey [1974] showed that by using the ratios of specific emissions from the visible spectrum (427.8, 557.7, and 630.0 nm) one can derive a characteristic energy for the precipitating particles. For global images the visible region of the spectrum has a drawback in that the bright sunlit hemisphere overwhelms the auroral signal. Much of the auroral activity near the terminator may also be lost due to this interference. Photometers sampling at FUV wavelengths are less hampered by this constraint because the intensities of FUV dayglow emissions in the high-latitude sunlit hemisphere are not entirely dissimilar to the intensities of auroral emissions.

Dynamic Explorer 1 (DE 1) data consist of photometric images of the entire auroral region with a temporal resolution of approximately 12 minutes and a spatial scale from apogee on the order of 100 km [Frank *et al.*, 1981]. When the geometry is correct, sequences of images of the entire auroral region can be obtained over a period of several hours. An example of such a sequence is shown in Figure 1.6 for observations on 3 December 1981. The sequence of individual image frames is presented from left to right, top to bottom. The color bar used for this sequence to identify photometer counts per pixel is given in the first panel. The remaining panels show eight consecutive images sampled during this particular orbit. The time of start of imaging (in Universal Time) is given above each panel. Note the changes in the brightness and structure of the auroral oval from image to image, especially on the dayside and near midnight. Such sequences allow the researcher to follow the evolution of auroral activity over the entire region, often for several hours or longer.

Year/Day: 81/337

> 4.5
4.1
3.7
3.3
2.9
2.5
2.1
1.7
1.3
0.9
< 0.5

0343:40 UT

0355:49 UT

0407:58 UT

0420:06 UT

0432:15 UT

0444:24 UT

0456:33 UT

0508:42 UT
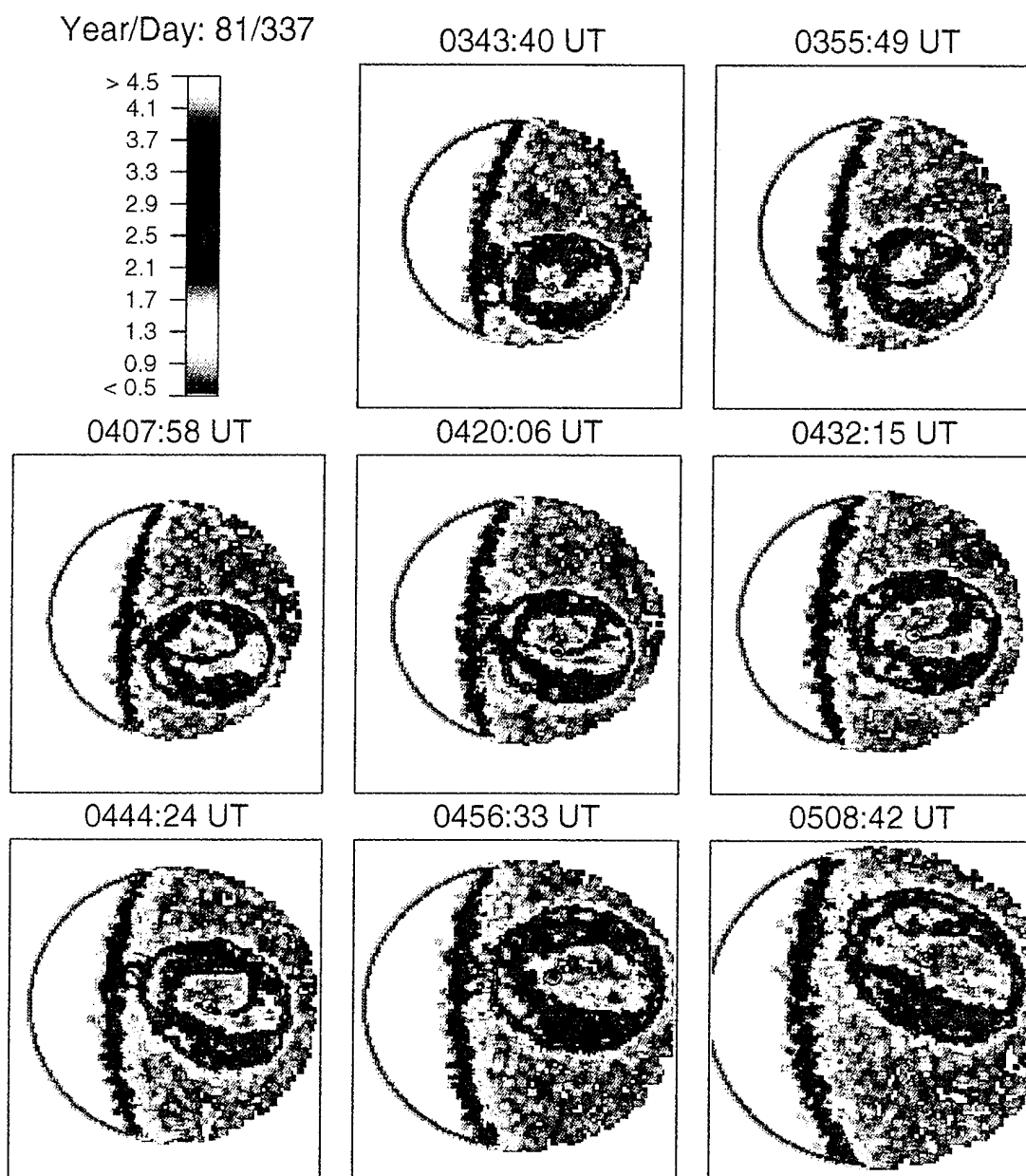
Figure 1.6 This sequence of images from the DE 1 data set shows more than an hour of sampling from an orbit on 3 December 1981. The images are of the northern auroral oval. The sequence is read from left to right, top to bottom, with the imaging start time in Universal Time given at the top of each panel. The color bar is given in counts per pixel in the first panel.

Objective

The objective of this research is to establish an estimate of the nearly instantaneous global pattern for auroral electron precipitation. This research lays the foundation for subsequent investigators by determining the feasibility of FUV broad-band photometric observations at 120-160 nm as a means of estimating the precipitation patterns and subsequently the electron energy deposition. By concentrating on the magnetically quiet periods of auroral activity this research is intended to investigate the use of an auroral-oval centered coordinate system as a baseline for other research to build on.

Chapter 2 describes the instrumentation pertinent to this research, and the basic physics involved in the use of remote sensing and, in particular, photometric measurements. In Chapter 3 the methodology used in data selection, evaluation and model building are discussed. Chapter 4 compares the models created by this research to other model currently available. A discussion of the results is given in Chapter 5.

CHAPTER 2

INSTRUMENTATION AND PHYSICAL PRINCIPLES

Dynamics Explorer Mission

The Dynamic Explorer 1 (DE 1) spacecraft was launched on August 3, 1981, into a highly elliptical polar orbit, with initial perigee and apogee altitudes of 570 and 23,300 km, respectively. The latitude of the line of apsides rotated in the plane of the orbit by about 0.3° each day. This allowed for viewing of both the northern and southern polar regions during the lifetime of the mission. The period of interest for this research is early in the mission when spacecraft apogee was over the northern polar region.

Dynamics Explorer 1 was spin stabilized with its spin axis perpendicular to the orbit plane. The spacecraft was equipped with several instrumentation packages including a magnetometer, plasma wave instrument, retarding ion mass spectrometer, plasma instrument, energetic ion mass spectrometer, and the spin scan auroral imager [Hoffman and Schmerling, 1981]. The scope of this research deals with only one of the spacecraft's packages, the auroral imaging instrumentation. A detailed description of the imager can be found in the paper by Frank *et al.* [1981], and as significant results are presented, for example, by Frank and Craven [1988], Craven and Frank [1991], Lummerzheim *et al.* [1991], Rees *et al.* [1988], and Sojka *et al.* [1992]. Only a brief review of the essentials will be covered here.

19

Imaging Instrumentation

A photometer is an instrument used to measure the intensity of light. Generally a photometer consists of a collimator, focusing elements, and a detector. The collimator defines the maximum field of view by allowing passage to only those photons coming from a limited range of directions and blocks strong sources of light at greater angles that can interfere with the imaging. From the collimator the photons pass through a focusing lens and into a detector. In this case, the detector is a photomultiplier, which, for weakly emitting sources, is used to increase the signal to a measurable quantity. For example, one photon entering the photomultiplier may produce $>10^5$ electrons at the photomultiplier's anode. Figure 2.1 shows a cut-away view of one of the auroral imaging photometers used on DE 1. Note the addition of a stepping mirror, parabolic mirror, and filter wheel to the basic photometer. The parabolic mirror acts as the focusing element.

The DE 1 Spin-Scan Auroral Imager (SAI) was equipped with three such photometers, designated A, B, and C. The photometers were mounted in the spin plane of the spacecraft looking radially outward, which allowed the photometers to sample over a full circle of 360° with each rotation of the spacecraft. Each rotation of the spacecraft took six seconds. In each image the path of the photometer's line-of-sight is referred to as a scan line. Each photometer was mounted with its line-of-sight centered in the spin plane of the spacecraft and with an angular separation of ~120° between photometers. Although each photometer operated during a full 360° scan, telemetry limitations allowed for the collection of data in only a 120° Earth-centered scan when all three photometers were operating simultaneously.

Each photometer also scanned a 30° field of view centered on and perpendicular to the plane of rotation by means of the stepping mirror. The mirror was rotated 0.125° once each revolution of the spacecraft to change the direction of the field of view by 0.25°.

D-G78-177

PARABOLIC
MIRROR

RAY PATHS

MIRROR
MOTOR

PINHOLE

LENS

FILTER
WHEEL

FILTER WHEEL
MOTOR

STEPPING
MIRROR

PHOTOMULTIPLIER

COLLIMATOR

SPIN-SCAN IMAGING PHOTOMETER
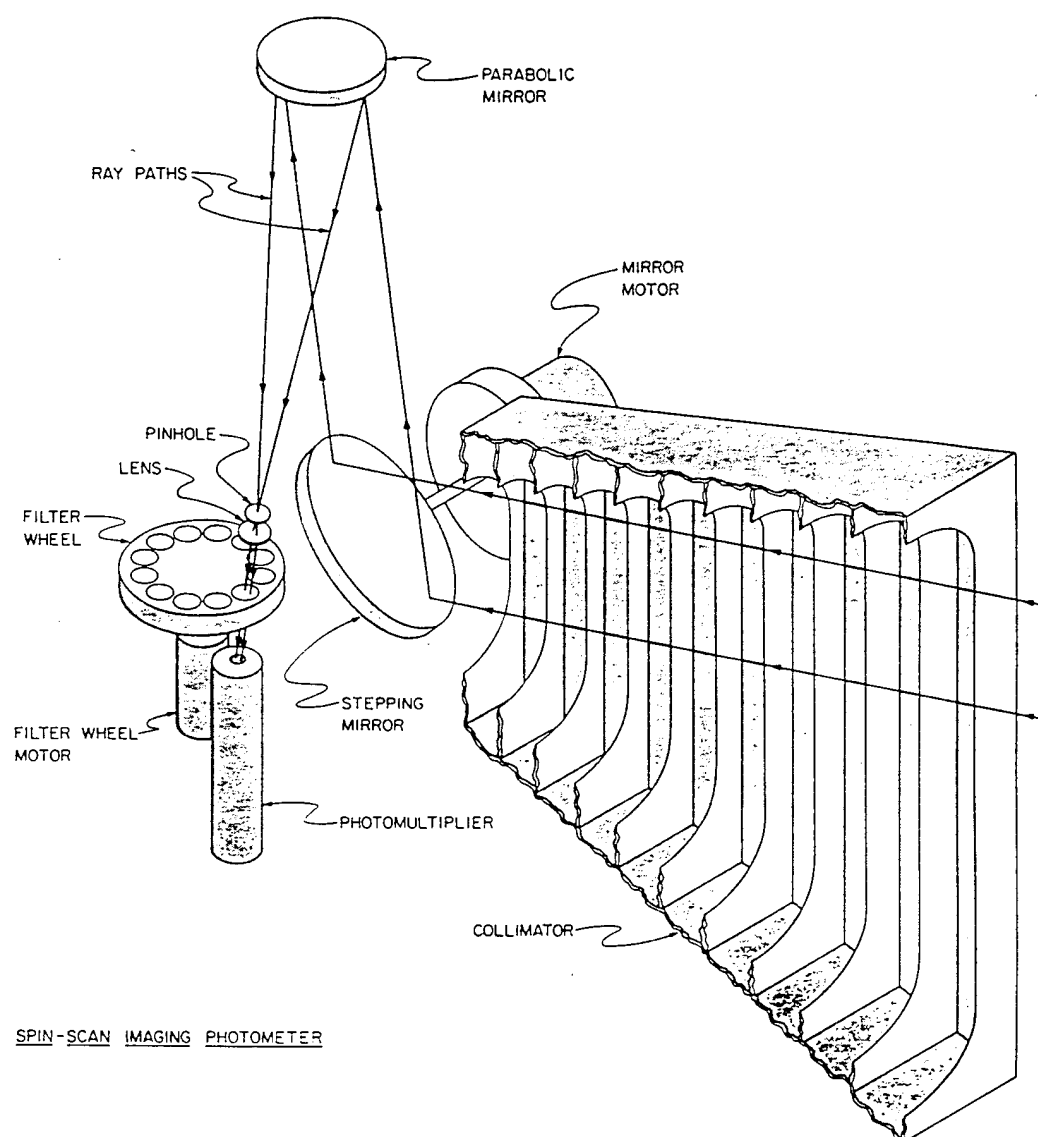
Figure 2.1 A pictorial diagram displaying the principal optical elements of an auroral imaging photometer. The stepping mirror selects the region being sampled for each scan line. The parabolic mirror focuses the incoming rays through the pinhole, lens, and filter into the photomultiplier [Frank et al., 1981].

There are 120 scans per 30°. A full 120 scan image was completed in 720 seconds (12 minutes). The sampling time of the photometer was 3.4 ms per pixel which corresponds to 0.20° of spacecraft rotation. This arrangement created a two-dimensional array of pixels for each image, each pixel having the angular dimensions of 0.20° x 0.29°. Figure 2.2 depicts this graphically. The left-hand side of the figure shows the spinning spacecraft and the ground track of a sampled scan line of the auroral oval (not to scale). The ground tracks crossing the auroral oval correspond to the centers of two consecutive scan lines, separated by 0.25°. The 0.32° instantaneous field of view along a scan line is depicted on the dayside region of the auroral oval.

The right side of Figure 2.2 shows the detailed structure of a single scan line and two consecutive scan lines. The sequence is from top to bottom. Although the instantaneous field of view is 0.32°, the actual sample field of view weighted for sampling time is only 0.29°, as seen in the third panel. This sampled field of view defines one pixel. The center-to-center separation between consecutive pixels in a scan line is 0.23°, resulting in some overlap in consecutive pixels. In the next scan line the pixels can be offset slightly along the scan line (bottom panel) and slightly overlap the region covered by the previous scan line. This overlap limits the amount of area not sampled by the imager. Each image is made up of these pixels over angular dimensions of 30° x 120°.

Photometers A and B responded to photons in the visible spectrum, while photometer C sampled in the far ultraviolet (FUV). Each photometer was equipped with 12 selectable filters. This research is concerned with data obtained using the photometer C and a single filter. The filter used was designed for peak transmission at a wavelength of 131 nm and a bandpass from 120 nm to 160 nm [Frank *et al.*, 1981]. Its principle function was to monitor OI emissions. Figure 2.3 shows the passbands and sensitivities for six of the filters for photometer C. The dash-dot-dash line corresponds to the filter 2
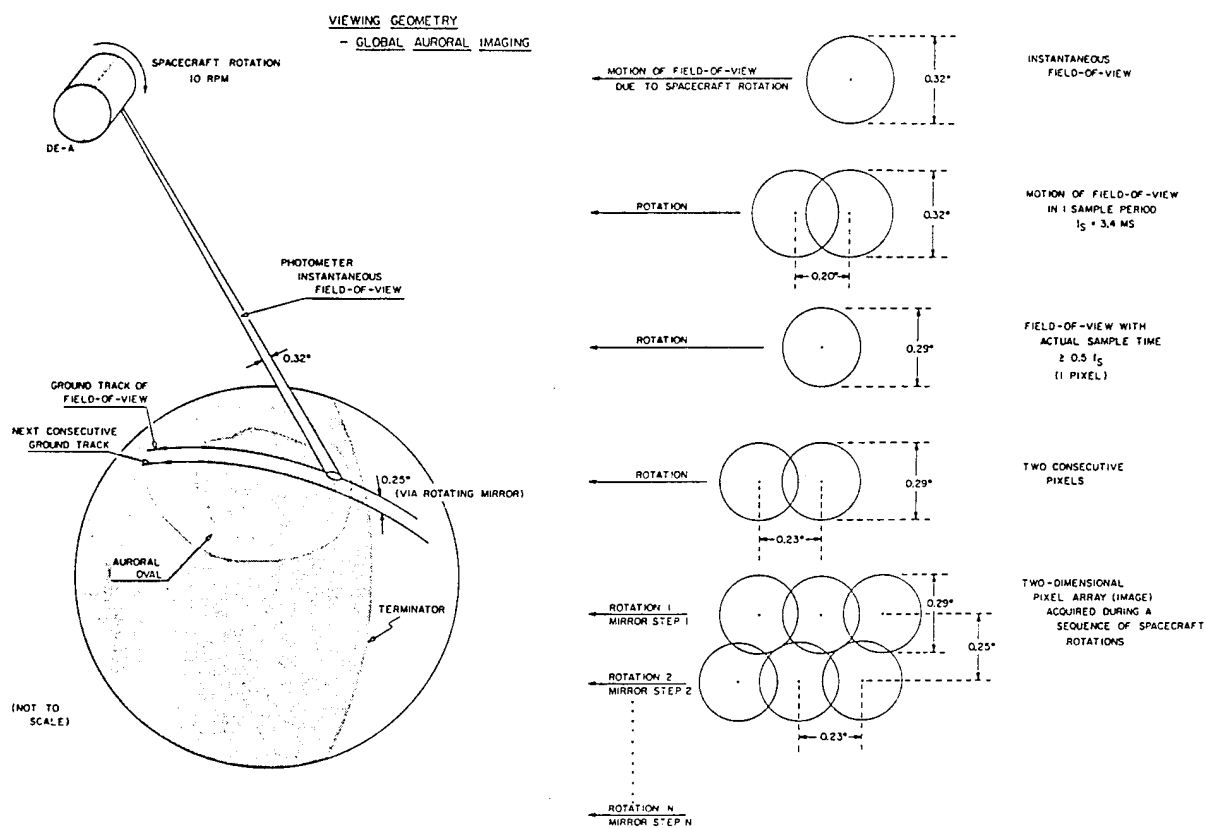
Figure 2.2 Diagram depicting the viewing geometry a Spin Scan Auroral Imaging photometer relative to the auroral oval. An enlarged view of the angular dimensions of a pixel, a successive pixels, and a neighboring scan line are shown in the right side of this figure [Frank et al., 1981].
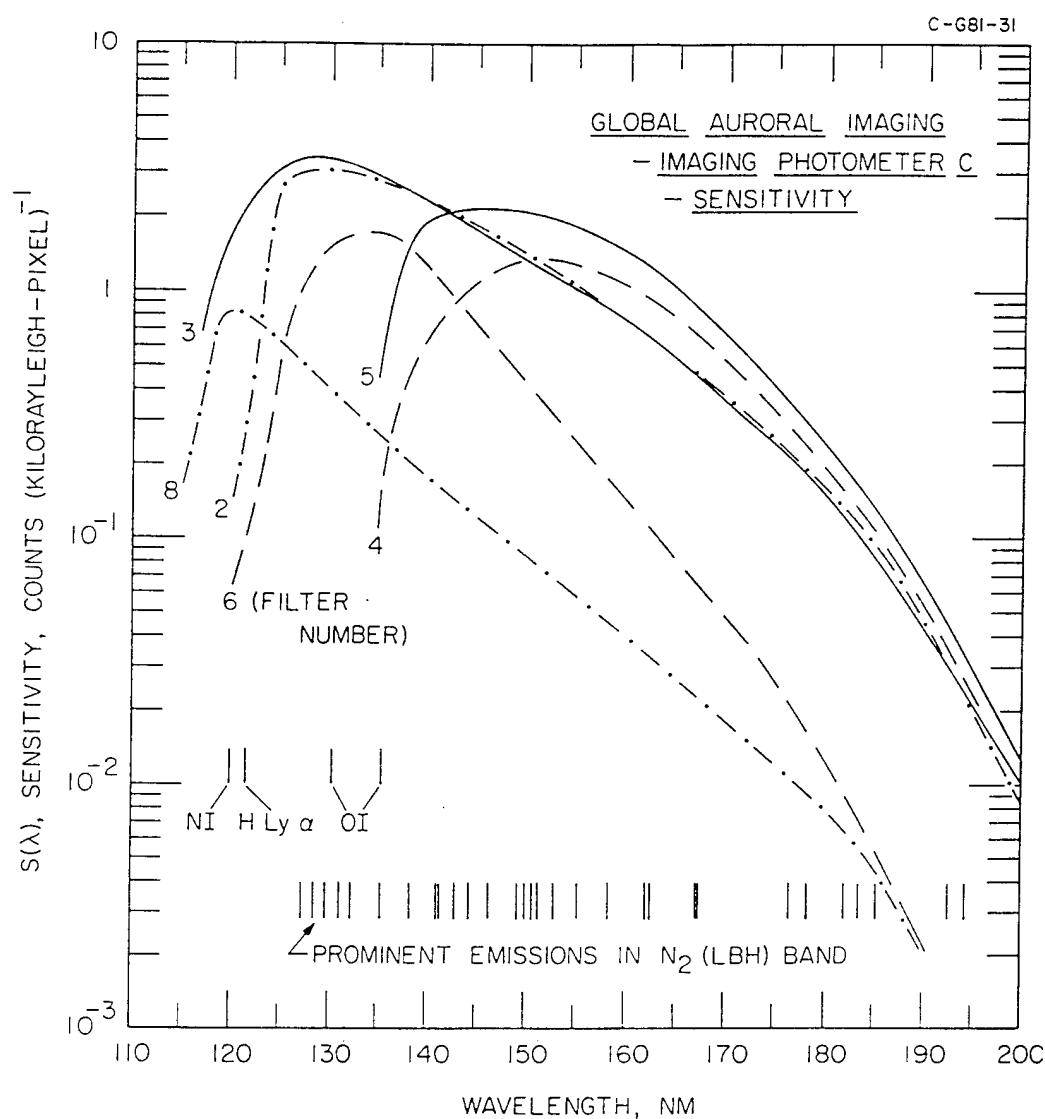
Figure 2.3 The absolute sensitivities of vacuum-ultraviolet imaging photometer C as functions of wavelength for six of the twelve filters in its filter wheel [Frank et. al., 1981]. Filter 2 corresponds to the 123W filter used for this research.

used in this research (#2, later designated 123W). Prominent auroral emission features are identified as vertical lines near the bottom of the graph. Note that the peak of the passband for the 123W filter is at the emission lines for OI. Based on the filter sensitivities given in Figure 2.3, the emission bands from Table 1.1, and the column emission rates given by Meier and Strickland [1991] for a 1-keV characteristic electron energy distribution and an energy flux of 1 $erg \cdot cm^{-2} \cdot s^{-1}$, I calculate that the OI(130.4) emissions account for approximately 74% of the total emissions detected by the 123W filter. This was done by dividing the scaled column emission rate for OI(130.4) by the sum of all the column emission rates scaled by the filter sensitivity for each wavelength within the filter's bandpass. For the other emissions the percentages are about OI(135.6) 15%, N_2 (LBH) 6%, and NI 5%. The emissions for HI are negligible in the absence of strong proton precipitation. These estimates are based on preflight sensitivity data, but are accurate to within 5% for the imaging data used for this research since it was obtained during the first several months of the mission. Studies using later imaging data should take into account changes in photometer sensitivities. Other researchers get different results. For example, Robinson et al. [1989] found that the OI(130.4) emission contributed only 65% of the total emissions as seen by the 123W filter. Some of the discrepancy in percent contribution of OI(130.4) may arise from a different assumption about the characteristic energies. Also Robinson et al. did not calculate the OI contributions through a direct method, relying instead on the output of model calculations for the Hall and Pedersen conductivities. Even with such a discrepancy there is still evidence that OI(130.4) is the primary contributor to the emissions detected by the photometer.

Image Processing

The telemetered data were processed at the University of Iowa. All images were processed via software systems and transferred into Mission Analysis Files (MAF). The processing created Earth-centered images of 120 pixels x 150 pixels, corresponding to a 30° x 30° field of view. The header file of each image included the photometer and filter codes used to calculate the photometer response and spacecraft attitude information, which are necessary to reconstruct the image.

Using a customized software image display package, XSAI, designed by Rae Dvorsky at the University of Iowa, selected images can be displayed on a VMS-based VAX station. XSAI allows the user to interactively display images and do some basic evaluation of phenomena. Graphics routines allow the use of false color enhancement of images. Geometric interpretation routines calculate various user selectable geographic and geomagnetic coordinates for each pixel of the image from the spacecraft attitude data.

The XSAI software package was used to extract the photometer counts and the geomagnetic coordinates for each pixel. Once the desired data were extracted from each MAF it was converted for further processing into a format usable by Research Systems Incorporated's Interactive Data Language (IDL).

Physical Principles and Assumptions

The object of this research is to create a mean quiet-time image of the aurora from the spacecraft photometer data. This mean image will be used as a baseline in the development of a spatial and temporal model of the electron energy deposition. To do this one must first convert the photometric counts to photons per second for a given region of interest. Each photometer and filter combination had a specific wavelength-dependent sensitivity, and a conversion from counts per pixel to an equivalent surface brightness in

kilorayleighs was established. The combination of the 123W filter and photometer C gives a specific sensitivity S=3.08 counts per kilorayleigh-pixel [Frank *et al.*, 1981]. Again, refer to Figure 2.3 for the exact sensitivity curve for the filter.

One of the variables of this calculation is the surface area of the emitting surface sampled in each pixel. This area is dependent on the solid angle of the pixel, and the spacecraft altitude. If Ω is the solid angle of the photometer then the area, A, of a pixel in the nadir direction is given by $A = \Omega r^2$ where r is the spacecraft altitude above the emitting surface. But for each image there may be only one pixel, if any, that is normal to the line of sight from the spacecraft to the emitting surface. So we must incorporate into this area calculation a method of finding the physical area of each pixel as seen by the photometer. This is done by including the spacecraft zenith angle (DZA) as measured from the line of sight from the center of the pixel to the spacecraft. The physical area, A_p, is then given by

$$A_p = \frac{A}{\cos(DZA)}.$$

As a first calculation, the observed counts per pixel, C, are converted to photons per unit solid angle per second, P_s, by first dividing by the photometer sensitivity, S (C/S in kR), then assuming isotropic emission over 4π steradians and applying the definition of the kilorayleigh (10^9 photons$(cm^2 \cdot sec)^{-1}_{column}$ radiated isotropically), and finally multiplying by the area A_p viewed by the photometer, to yield

$$P_s = \frac{10\ CA_p}{4\pi S} \text{ photon} / \sec \cdot sr.$$

The total photon emission rate from A_p is then

$$\frac{10\ CA_p}{S}\ \text{photons}/\text{sec},$$

for isotropic emission and no scattering or absorption in the line of sight from the emitting surface to the spacecraft. An estimate of the actual number of photons being emitted at A_p is found by calculating the absorption above the emitting source and incorporating it into a correction factor.

To further complicate these calculations, the emissions do not come from a simple emitting surface, but from a layer in the atmosphere. Thus the observed emissions from that layer are given by the integral of the volume emission along a column through the layer weighted by absorption within the column. Some emissions occurring lower in the atmosphere may not contribute to the emissions seen at the spacecraft due to absorption. For example, OI(130.4) emissions occurring at ~120 km altitude will be reduced in intensity due to absorption by the Schumann-Runge band of molecular oxygen, and more importantly by resonance absorption by IO. The column is said to be optically thick to such emissions. The optical thickness varies for each wavelength of photon emitted and the constituents of the gas they must travel through to get to a detector. Other emissions may be absorbed and then radiated in a random direction, or scattered. This scattering of the photons emitted broadens the region from which emissions are sampled. Some form of correction for this broadening needs to be built into the model calculations. This will give the true spatial dimensions of the precipitation patterns. These absorption and scattering processes in the lower atmosphere are beyond the scope of this research, and how they are dealt with depends on the thermospheric model and the assumptions used to

make that model. Here we will discuss only the emissions as seen by the satellite and will let other researchers interpret the processes that lead up to such emission patterns.

One model for the absorption and scattering processes has been developed by Rees and Lummerzheim [1988] and will be used later in this research to compare results found here with other precipitation pattern models. Lummerzheim [personal communication, 1994] has calculated a relationship between the characteristic energies of precipitating auroral electrons described by a Maxwellian velocity distribution and the corresponding count rates of the DE-1 FUV photometer. Figure 2.4 shows the calculated curves for the 123W filter. These curves are based on multiple runs of the MSIS 90 model, which is an analytic empirical model of the upper atmosphere based on satellite mass spectrometer and ground-based incoherent scatter data [Hedin, 1991]. Lummerzheim varied the differential cross section of the atmospheric constituents, the generation of secondary electrons, and the degradation of the primary non-ionizing electrons [personal communication, 1994; Lummerzheim and Lilensten, 1994]. He also ran these conditions for different levels of solar activity by varying the $F_{10.7}$ cm flux, which is an indirect indicator of the solar extreme ultraviolet flux at Earth. This graph depicts the characteristic electron energy along the abscissa, in keV, and the count rate of the photometer along the ordinate in counts per pixel. These curves are normalized to an incident energy flux of 1 erg cm^{-2} s^{-1}. Each line represents a separate different run of Lummerzheim's model. The variations show the possible changes one might encounter in the real world. A fit to the mean of these curves is used later in this research.

From the physical principles described in this chapter and by using the Dynamics Explorer data set, one should be able to establish a nearly instantaneous model for the global precipitation pattern and be able to make inferences about the global electron precipitation pattern. The methods used to obtain such global patterns for the quiet
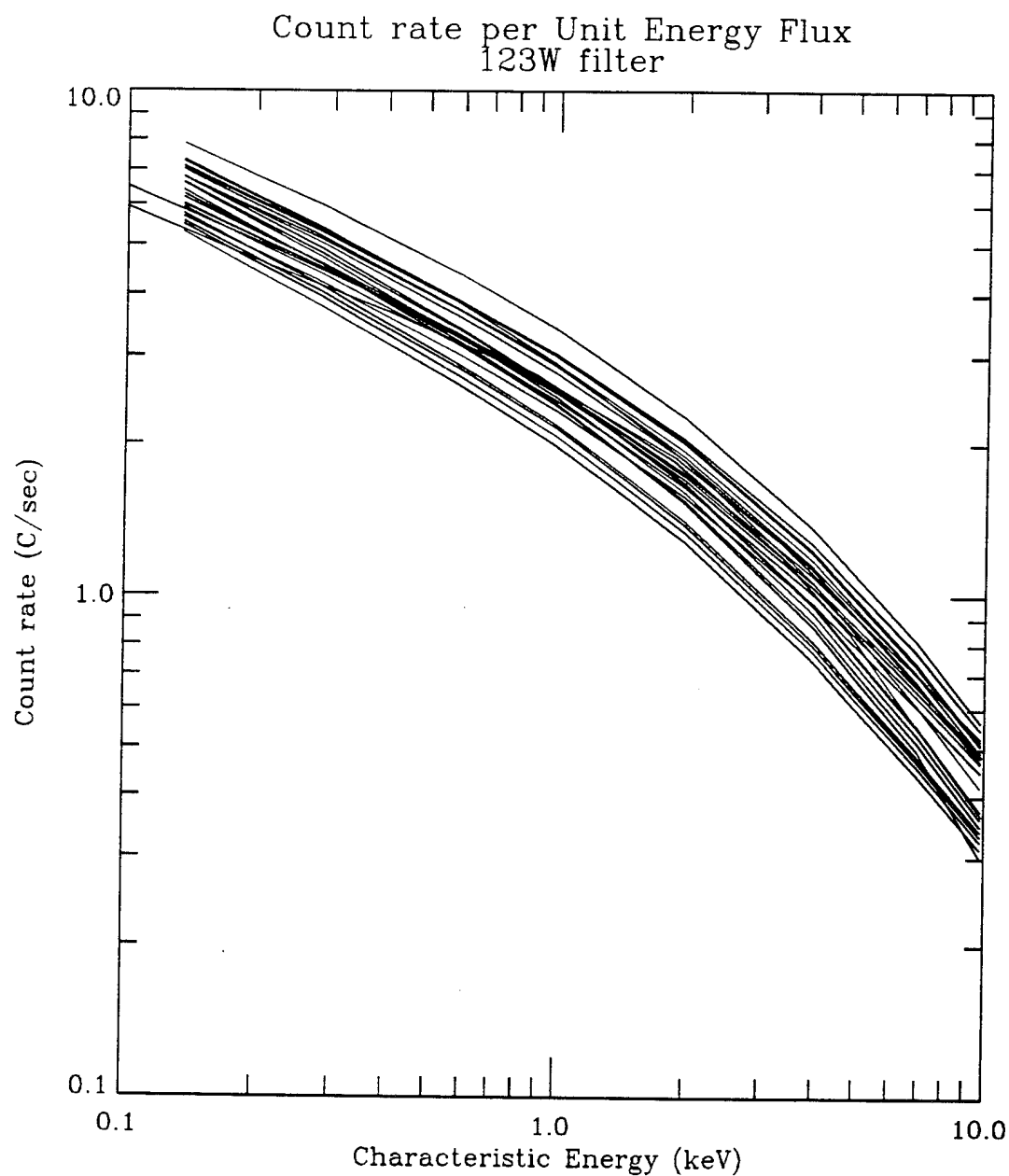
Figure 2.4   Predicted count rates for an electron energy flux of 1 erg/cm/s as a function of the characteristic energy of an assumed Maxwellian spectrum. Calculations used the MSIS 90 atmospheric model [Lummerzheim, personal communication, 1994].

aurora are discussed in Chapter 3. A comparison of the results to other precipitation pattern models is discussed in Chapter 4.

CHAPTER 3

DATA SELECTION AND ANALYSIS

Selection Criteria

Images of the aurora for magnetically quiet times were chosen to establish a baseline pattern of auroral energy deposition by precipitating electrons. This baseline can then to be used as the starting point for analyzing energy deposition for the more active aurora. The definition used for magnetically quiet periods was simply that the AE index be below 100 nT during each imaging period and decreasing. This threshold was chosen to compare my findings with those of other researchers (e.g., Hardy *et al.* [1985]; Spiro *et al.* [1982]) who have already used a 100-nT criterion to designate periods of low magnetic activity. Also, because only a finite number of images were available, an even lower threshold would have made the data set too small for reasonable analysis.

AE records for the period from the start of the DE-1 mission in 1981 through January of 1982 were scanned for periods of prolonged low magnetic activity. These magnetically quiet periods were then cross referenced to records of DE-1 observations using photometer C and the 123W filter. The 123W filter was chosen for its high transmission in the center of its passband, which favored detection of the 130.4 and 135.6-nm emissions of OI, and for the large attenuation of the H Lyα (121.6 nm) emissions [Frank *et al.*, 1982; Robinson *et al.*, 1989; and as shown in Chapter 2]. Since AE has a latitudinal dependence and some levels of increased auroral activity may not be evident in

the AE traces for a contracted oval, imaging sequences that met the 100-nT criterion were then viewed on microfilm to identify any auroral activity not evident in the AE records. The images were viewed in sequence on the microfilm to determine if there was any systematic brightening or expansion of the auroral oval that might indicate the onset of substorm activity not evident in the AE-index records. The viewing geometry was also checked at this stage to ensure that the entire oval was visible in the image. These criteria identified 176 possible images from 24 orbits.

These 176 images were then viewed using the image display software package XSAI. At this time a more detailed visual inspection was conducted to ensure minimum interference from dayglow, that the oval was sufficiently far from the limb (10° at ~110 km altitude above the Earth's surface) to eliminate limb brightening effects, and to avoid large uncertainties in surface area and position of each pixel at large spacecraft zenith angles. These selection criteria further reduced the size of the available data set to 134 images in 17 sequences.

These images were then converted to IDL format files using programs written by A. J. Nicholas [1993] and modified slightly for this research. These programs subtracted from the original image the limb region as defined by Nicholas and used an empirical quiet-time model for dayglow to subtract many of the dayside emissions. An example of a sequence of images in which the quiet-time dayglow is subtracted is shown in Figure 3.1, which is the same as seen in Figure 1.6. Comparison of Figure 3.1 and Figure 1.6 shows how the dayside emissions were minimized through this application of the dayglow model. Although the model did not eliminate all the dayglow emissions, it did allow for more precise measurement of the dayside auroral oval boundaries and emission patterns.

An interesting feature in these images is the extensive region of weak emissions at low latitudes in the nightside hemisphere, outside the auroral oval. Such emissions were
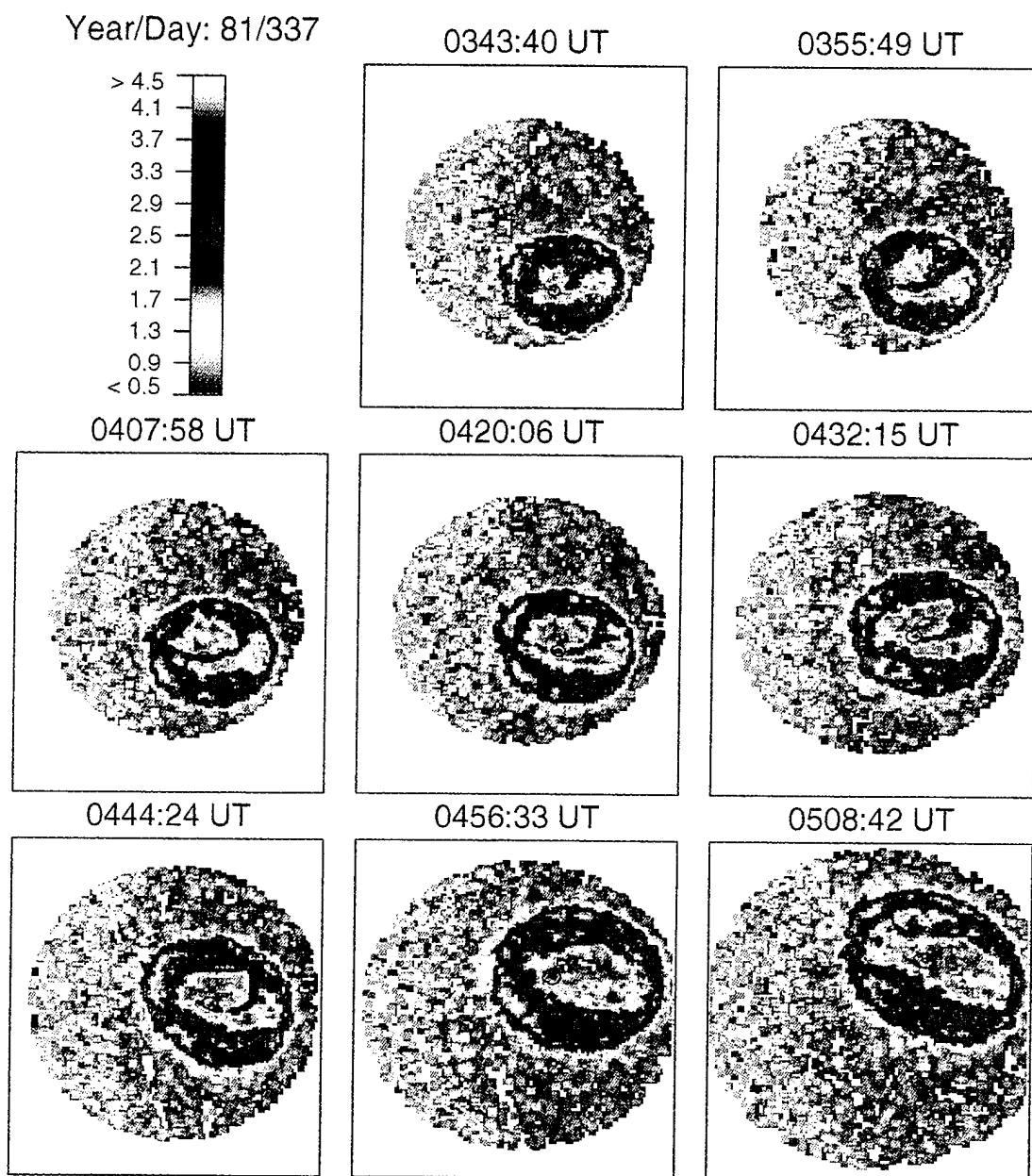
Figure 3.1   A sequence of eight consecutive images from the DE-1 data set for 3 December 1981. Similar in format to Figure 1.6, but with the dayglow background subtracted. The sequence is read from left to right, top to bottom, with the imaging start time, in Universal Time, given at the top of each panel. The color bar, in counts per pixel, is placed in the first panel. The circled dot represents the location of the geomagnetic pole.

not evident in all DE-1 images. A comparison of images in Figure 3.1 with the image shown in Figure 1.5 emphasizes the difference in the nightside emissions. Although some of the apparent difference is due to differences in the color bars used, the emissions seen in the nightside of the images in Figure 3.1 are real and not just noise. These nightside emissions were created by photoelectrons from the sunlit conjugate hemisphere that traveled along the closed field lines and precipitated into the nightside upper atmosphere in this hemisphere. Average photometer responses were generally < 1 count/pixel.

Finally, once the computer programs for limb and dayglow subtraction were applied to the images they were again viewed to ensure that portions of the auroral oval were not lost due to the limb subtraction, where the limb subtraction as defined by Nicholas [1993] was a more stringent condition than what was provided by the earlier visual inspection with XSAI. The additional inspection of the images ensured that the entire oval was visible in each image. This last test further reduced the data set used by this research to 85 images in 13 sequences. A list of the images used is provided in Appendix A.

Low-Latitude Boundary -- Initial Investigation

To establish the mean quiet-time geometry of the auroral oval (size, shape, location relative to a chosen coordinate system, etc.), an initial investigation of the low-latitude boundary, or edge, of the auroral emissions in the FUV was done. The size and location of this boundary was measured and correlated with the AE-index, the interplanetary magnetic field (IMF), and other geomagnetic and solar parameters in an attempt to establish a link between oval size and location due to known, and easily measured parameters. Determination of this quiet-time geometry and the physically relevant parameters that organize the observations is necessary to establish a baseline model of the auroral oval. The low-latitude boundary was then used to determine the size of the

auroral oval during quiet periods, in an attempt to find a lower limit to the area of the auroral oval.

The contours of the low-latitude boundary were first determined manually by visually inspecting a false-color image displayed on a twenty-inch monitor with XSAI and by placing points on the image (using the cursor and mouse) at the edge of the oval. The color bar used in XSAI was set with a threshold of about ½ count average ($\approx$150 rayleighs) for this display. The low-latitude boundary (LLB) was estimated by a series of points placed along this ½-count threshold. The contouring routine then computed a spline fit to these points and created an array of 100 data points along the contour in both geographic and geomagnetic coordinates. The contour routine also calculated the area encompassed by the contour. Finally, the contour was overlaid on the image and visually inspected to ensure that the low-latitude boundary encompassed all the emissions associated with the auroral oval.

To determine if there were any rapidly occurring spatial changes to the quiet-time oval, the size of the auroral oval and polar cap, as measured by the area encompassed by the contour, was then plotted against the time interval since the AE index last decreased below 100 and 50 nT. Figure 3.2a shows the area enclosed for the first and last image of each imaging sequence (dots connected by a solid line) and the time since the AE dropped below the 100-nT threshold. Figure 3.2b is a similar plot for those sequences where the AE index was less than 50 nT during the entire imaging time. Generally, the total area of the auroral oval defined by this low-latitude boundary decreases slowly with time, for each imaging sequence, as the AE index decreases below 100 nT and then remains below this value. This trend of decreasing oval size for a given sequence of images is also apparent for the plot of AE less than 50 nT. Because the areas generally varied slowly and systematically, only the areas of the first and last image of a given sequence are plotted to
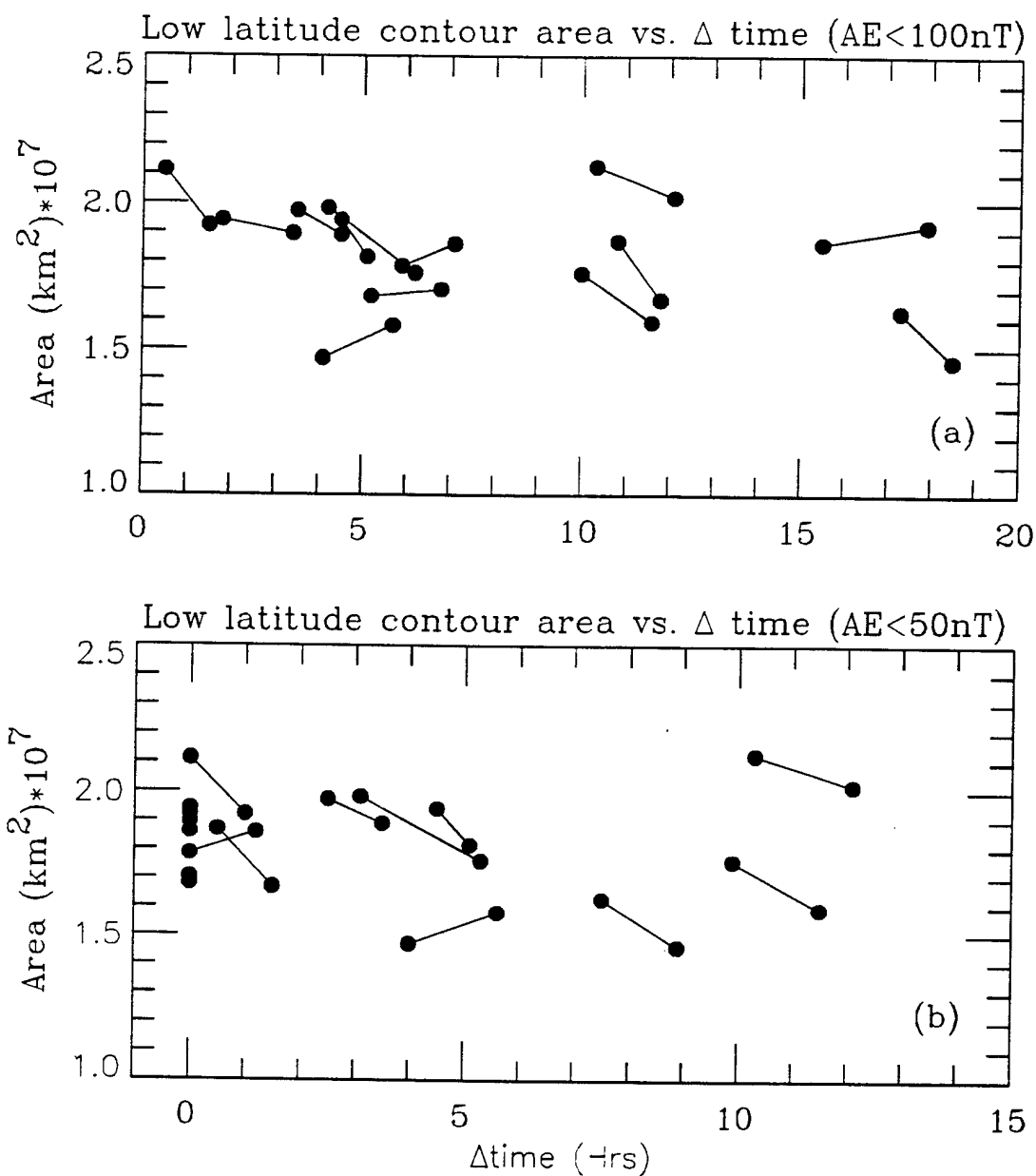
Figure 3.2 Plots of the area enclosed by the low-latitude boundary for the first and last image of (a) all sequences for AE ≤ 100 nT plotted against the time since the AE index passed below the 100-nT threshold, and (b) those sequences where AE ≤ 50 nT for the entire imaging time verses the time since the AE index passed the threshold of 50 nT.

show the total change during one imaging sequence. For a given sequence, the area may increase and/or decrease during the imaging time, but the general trend is indicated by the slope of each line connecting the two points.

From the areas given in Figure 3.2 a more convenient parameter was calculated, the angular radius, or geographic co-latitude, of a circle on a sphere that encloses the same surface area. The co-latitudes were calculated using the formula for the surface area of a sphere, and are measured in degrees of geographic co-latitude from the "pole" towards the "equator". This was done to see if the aurora oval came to some minimum size after a period of low or no activity. Figure 3.3a shows the geographic latitudes (90° - co-latitude) for all data plotted against the time since AE was first less than 100 nT. In the next two panels the latitudes are plotted for only those cases when AE was less than 50 nT, and plotted versus the time since AE first decreased below 100 nT (Figure 3.3b) and below 50 nT (Figure 3.3c). In each of the panels a linear and quadratic fit are depicted, with a solid line representing the linear fit, and a dashed line the quadratic fit. A quadratic fit to the data was first attempted since the decrease in area enclosed by the ovals was nearly linear and the area is a function of the square of the co-latitude for small angles. The linear fits were then investigated as a comparison.

The quadratic fit in Figure 3.3a varies little from the linear fit, and appears to have a minimum oval size of ~71° after 11 hours of being below 100 nT. The quadratic fit in this figure shows what one might expect, although it is only weakly quadratic. In Figure 3.3b, where the threshold of 100 nT is the same but using only those orbits where the AE index fell below 50 nT for the entire sequence, the quadratic fit is not as one would predict. Instead of a minimum value for the latitude, as in (a), the quadratic fit indicates a very weak increase in the rate of the oval shrinking as time passes. In Figure 3.3c the quadratic fit to the data shows a minimum in the auroral oval size of ~72° after the AE index has
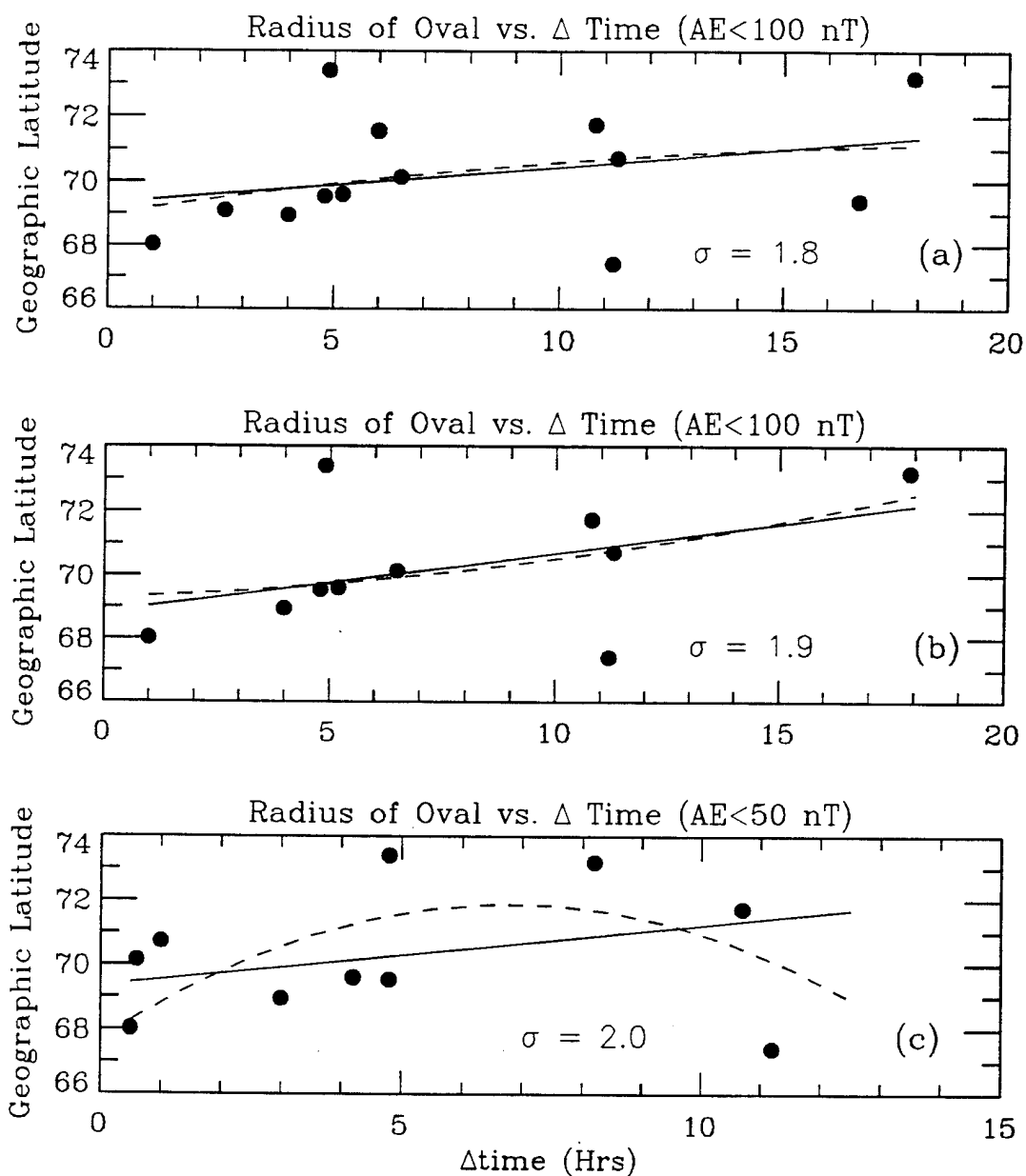
Figure 3.3 Plots of the radii of circles of equivalent areas of the mean areas for each sequence depicted in Figure 3.2 for (a) all sequences where AE ≤ 100 nT, and (b) those sequences where AE ≤ 50 nT during the entire imaging time verses the time since the AE index passed below the 100-nT threshold. Panel (c) depicts those sequences where AE ≤ 50 nT during the entire imaging time plotted against the time since AE passed below the 50-nT threshold. The sigma values given are for the linear fits.

been below 50 nT for 5-7 hours, and then begins to expand. This quadratic fit is counter to what one would expect for long magnetically quiet periods. Note that the slope of the linear fit in Figure 3.3a is 0.11°/hour and 0.19°/hour for panels (b) and (c). The error of the slopes for all three fits is ±0.07°/hour. The t=0 intercept for all three panels is 69° ± σ, where σ is 1.8, 1.9, and 2.0°/hour for panels (a), (b), and (c), respectively. This shows a tendency for there to be an increase in the rate at which the auroral oval shrinks when the AE index remains below 50 nT. The data point at ~11.2 hours (latitude of 67.4°) in all three panels does not fit well with the other data, and is largely responsible for the poor quadratic fit in Figure 3.3c. All parameters for this imaging sequence were reviewed and none were found suspect. This data point meets the criteria set for all the other data used.

The low-latitude boundary contours for all images were summed and averaged, with each contour weighted equally, to create an average auroral oval size for the magnetically quiet periods. This average oval size compares favorably with the results of Holzworth and Meng [1975] for similar magnetic activity, as can be seen in Figure 3.4, and provides a first comparison of this work with previous, independent measurements. Holzworth and Meng [1975] used the Q-index (discussed below) to quantify magnetic activity, and an estimated position for the boundary was obtained using DMSP auroral images with which they were able to view a major portion of the oval in the visible spectrum. The Q index is closely related to the AE index. The top panel shows the mean LLB for those imaging sequences with AE < 50 nT (solid line) and the calculated oval size given by Holzworth and Meng [1975] (dash-dot line) for Q=2. The lower panel is a similar plot for all DE-1 images (AE < 100 nT) and Q=3.

The Q index was proposed in 1956 as a measure of geomagnetic activity for use during the International Geophysical Year (IGY). The index was calculated every fifteen minutes from the H component of the ground magnetometers in conjunction with the

12 mlt

50°

70°

18 mlt — 06 mlt

(a)

AE < 50 nT
Q = 2

00 mlt

12 mlt

50°

70°

18 mlt — 06 mlt

(b)

AE < 100 nT
Q = 3

00 mlt
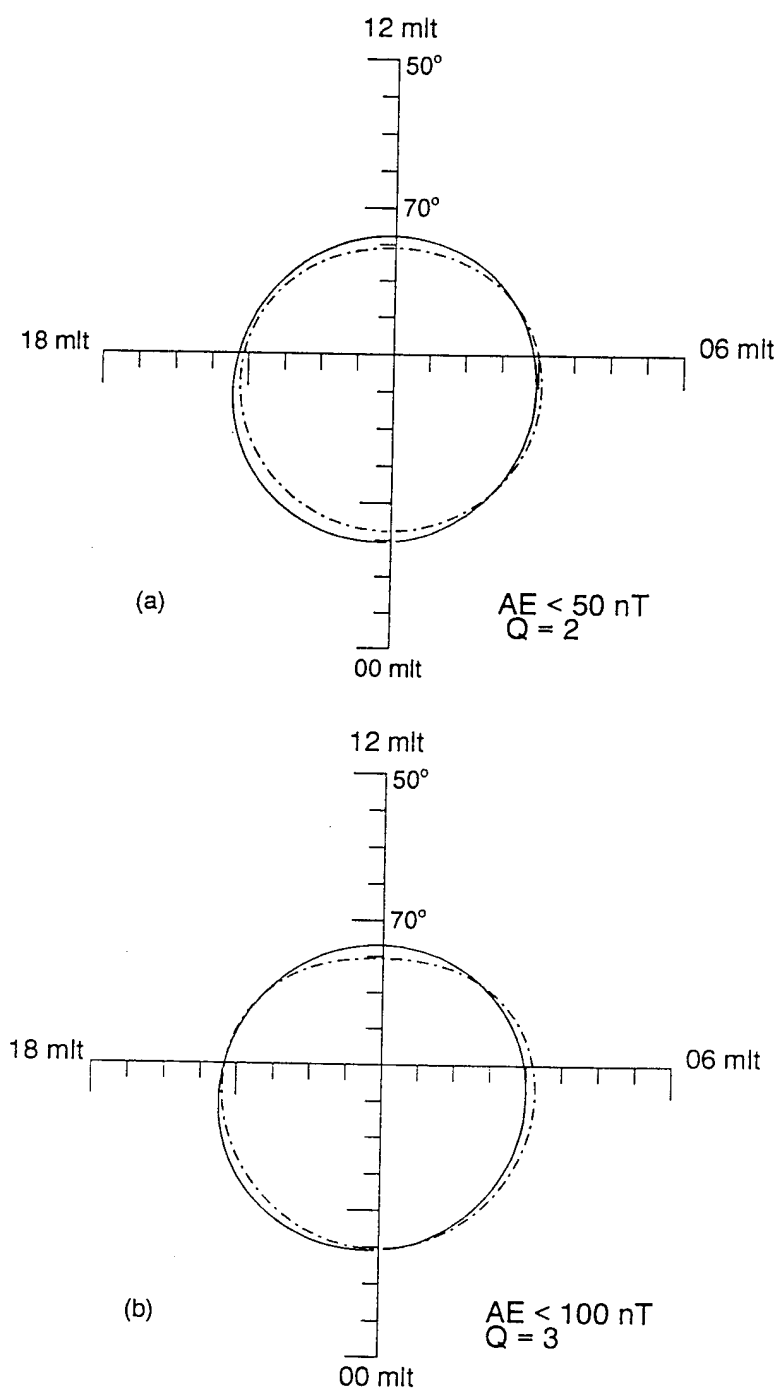
Figure 3.4 Low-latitude boundary for (a) AE $\leq$ 50 nT and Q $=$ 2, and (b) AE $\leq$ 100 nT and Q $=$ 3. The solid line denotes the boundary for the DE-1 results presented here, at an average auroral brightness of 150 R. The dash-dot line is the boundary as determined by Holzworth and Meng [1975] with DMSP auroral images.

quarter hourly ionosondes and other auroral observations taken during IGY. It used the magnitude of the positive or negative deviation of the magnetic field's H component from its quiet value. Only the records from high latitude observing stations were used in the formation of the index, and no averaging was done: only the maximum deflection was used [Mayaud, 1980]. Unlike the AE index, the Q index was divided into twelve levels of activity, similar to the K_p index. For Q = 0 the deflection of the H component was less than or equal to ten nanoteslas. Similarly, a Q value of 1, 2, 3, 4, 5, 6, 7, 6, 9 or 10, is assigned for deflections of less than or equal to 20, 40, 80, 140, 240, 400, 660, 1000, 1500 and 2200 nT, respectively. A Q value of 11 denoted all activity with the deflection greater than 2200 nT [Fukushima and Bartels, 1956]. This is similar to the AE index in that measured of the deflection of the H component of the ground magnetic field at auroral latitudes. The AE index is also measured in nanoteslas, but is not quantized into a limited number of values: the actual value of the maximum perturbation is used. The closest value of Q for AE $\leq$ 50 nT is Q = 2, for which $\Delta H \leq$ 40 nT. Similarly, for AE $\leq$ 100 nT the closest Q value is Q = 3 ($\Delta H \leq$ 80 nT).

This study of the low-latitude extent of the auroral oval shows that the magnetically quiet oval is roughly a circle with its center offset from the geomagnetic pole towards midnight by 4° and 1° towards the evening sector. It also confirms that the equations for the low-latitude boundary published by Holzworth and Meng [1975] remain valid for the quiet-time data. Figure 3.5 shows the mean center of the low-latitude boundaries determined here for each sequence plotted relative to the geomagnetic pole. The origin is the geomagnetic pole with local noon towards the top of the page and 0600 MLT to the right. The triangle on the plot located at (-0.3°,-4.4° ±1°) shows the mean center of the quiet-time auroral oval low-latitude boundary as visually estimated during this initial investigation. The asterisk is the mean center for Holzworth and Meng's oval. Note the

Low-latitude Boundary
mean centers
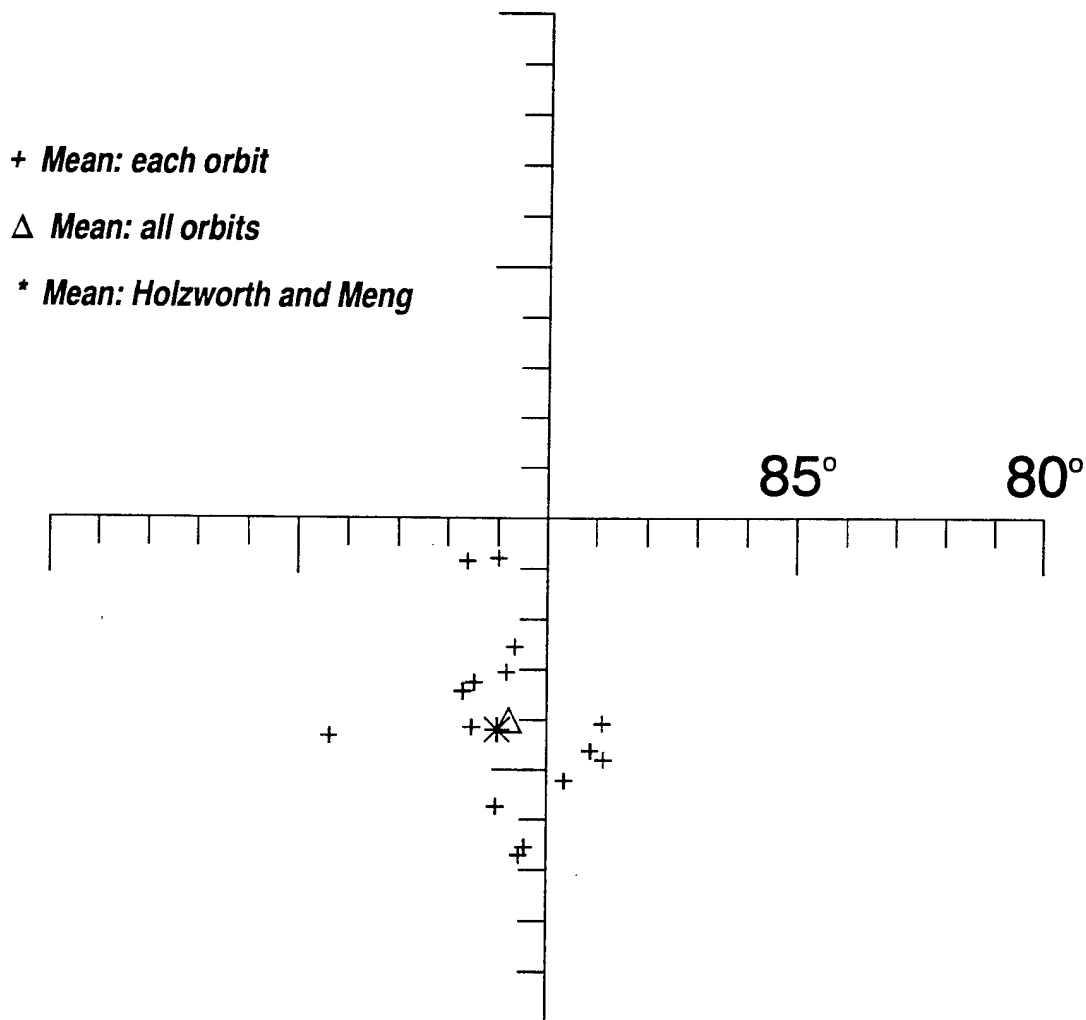
Figure 3.5 Center of the mean low-latitude boundary for each image sequence (plus), the mean for all sequences (triangle), and the mean center for the Holzworth and Meng [1975] boundary.

near coincidence of the two means. A brief investigation of the location of the center of the oval and its relationship to geomagnetic parameters was done for each sequence for the IMF components B_x and B_y, and D_{st}. The investigation of quiet-time auroral conditions requires $B_z > 0$. There were insufficient data to draw any conclusions about the influences of these parameters on the location of the center of the oval.

Figure 3.6 shows two examples of the visually estimated contour from XSAI plotted on a Mercator projection of the corresponding images. The dark solid line denotes the low-latitude contour as visually estimated by using the XSAI computer program described earlier. The contours for the two images in this figure do not necessarily overlay directly with the low-latitude edge of the color display. An investigation of these overlays shows that the difference between the contoured boundary and the more exacting boundary of a given number of counts/pixel, as will be discussed in Chapter 4, is not systematic. These two images are good examples of how difficult it can be to visually estimate the position of the low-latitude boundary.

In conclusion, contours were visually estimated using the computer program XSAI for each image to get a first-order approximation of the quiet-time auroral oval dimensions. This investigation showed the oval to be circular with a center offset from the geomagnetic pole. The changes in the dimensions of the oval after AE went below a given threshold were used to investigate whether the oval would reach some minimum size. Although no minimum dimensions were shown conclusively, some systematic behavior of oval 'shrinking' is seen in the data. A mean contour was calculated for the quiet-time aurora and compared with similar work done by Holzworth and Meng [1975]. This comparison confirmed their results and showed that a visual estimate of the low-latitude auroral oval boundary is a good starting point for further investigations.

0408:41 UT

0421:26 UT
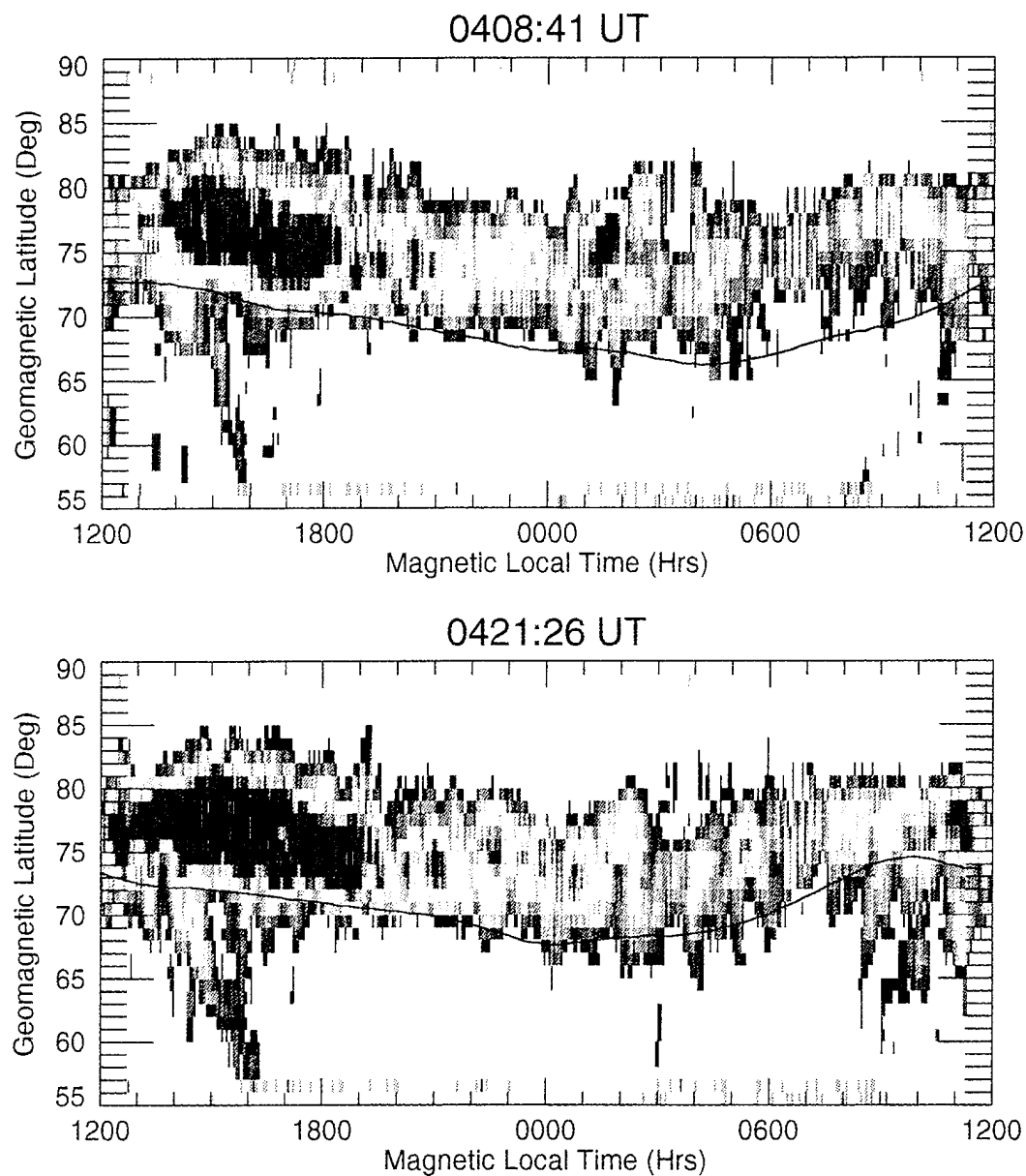
Figure 3.6 Two examples of visually estimated contours from XSAI plotted onto the corresponding images in a Mercator projection. The two images are from December 17, 1981. The solid black line denotes the visually estimated contour.

Figure 3.7 shows the color bar used for these and all images in this and subsequent chapters. The range of the color bar for this work is very narrow, with the range for the average photometer response varying from ~0.6 to 2.4 counts/pixel (left of the color bar, unless otherwise noted). Although in the actual raw data the counts are integers and generally range from 0 to 6 counts for the quiet time auroral emissions, because we do large scale averaging the color bar used here is scaled to the fraction of counts. Note that all the images depicted have been smoothed with a 3 x 3 boxcar (nearest neighbor) routine for better presentation.

Image Analysis

Viewing individual images in different sequences shows that there is a need for some sort of averaging of the magnetically quiet-time data. First, we can do an average because as shown before the auroral oval varies slowly over time for these quiet periods. A method of averaging needs to be investigated that will limit the washing out of spatial features. The averaging processes and their results are discussed in this section.

After the size of the auroral oval was established for magnetically quiet times, the 85 images in the final data set were analyzed for their FUV emission patterns, or structures. Each mission analysis file (MAF) was converted to a format that could be analyzed in the IDL environment, with each file containing the 120 x 150 pixel array comprising the image, the geographic and geomagnetic coordinates for each pixel of that image, and the values of the dayglow background that apply to that image. The background values were computed using algorithms created by A.J. Nicholas [1993] and modified by T. Immel [private communication, 1994].

The auroral observations were extracted from each image to scale them to a common size for comparison and presentation. Returning to Figure 3.1 note that as the

Color Bar
(counts/pixel)

> 2.5

2.3

2.1

1.9

1.7

1.5

1.3

1.1

0.9

0.7

< 0.5

> 4.5

4.1

3.7

3.3

2.9

2.5

2.1

1.7

1.3

0.9

< 0.5
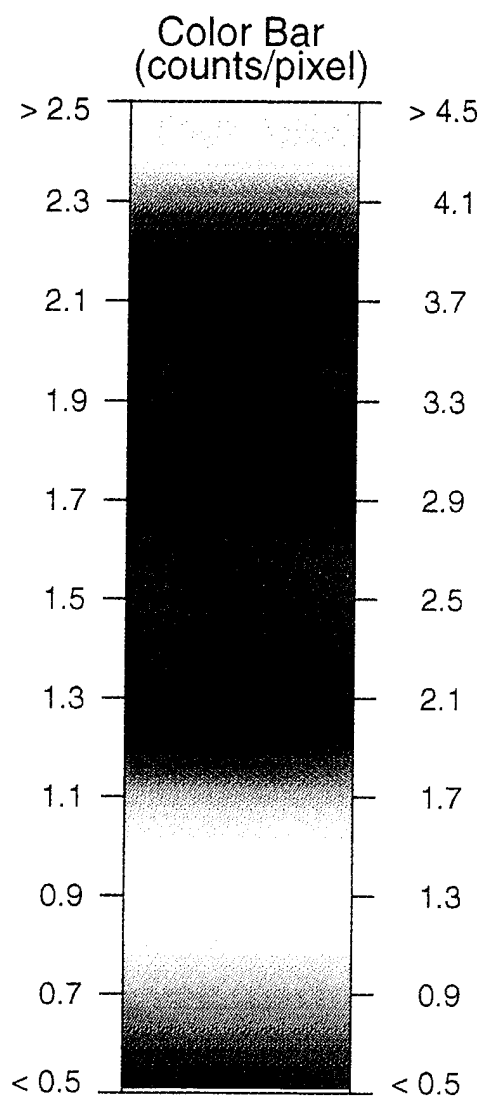
Figure 3.7 The color bar used for the images shown in Chapters 3 and 4. The scale on the left side of the bar (in counts/pixel) is used for most of the images. The scale on the right side of the bar is used only one set of images, as specified in the text.

spacecraft approached the Earth the fraction of the total field-of-view containing the auroral oval increased. From such a series of images it can be difficult to visibly discern slow changes in auroral oval size and shape. Also from Figure 3.1 one can see that there are many features in the image that are equatorward of the oval and, for this research, are not necessary. To eliminate unwanted data and isolate the area of interest for this research in each image, only those pixels located at geomagnetic latitudes >55° North to the pole were extracted from each file. Three 35-by-360 element arrays were created containing counts per pixel, model background, and number of samples per bin. The dimensions of each array correspond to the geomagnetic coordinates of the pixels, 0° to 34° for the geomagnetic colatitudes, and 0°-1° to 359°-360° for the magnetic local time in degrees (15° = 1 hour). The number of samples in each 1° x 1° bin is specified by an integer value. The number of samples is used later in calculating weighted average values for the photometer's response. For spacecraft altitudes of use here, the angular dimension of individual pixels were also ~1° at auroral emission altitudes. Hence, each pixel is treated as an independent sample.

Previously shown in Figure 3.1 is a sample of an orbital sequence for day 337 of 1981 before the binning was done, but with the dayglow background subtracted. Figure 3.8a depicts a sample binned image for 1004:08 UT, December 17, 1981, in a Mercator projection on the left and a polar projection on the right. The Mercator projection depicts geomagnetic latitude along the ordinate and the magnetic local time along the abscissa. The polar plot orients the oval such that up is the direction to the Sun. The intersection of the axes for the polar projections denotes the geomagnetic pole. Each of the axes ranges from 90° at the pole to ~65° latitude at 0600, 1200, and 1800 MLT, and ~64° at 0000 MLT. Figure 3.8b is a simple mean image of all data used in this study, without any weighting or scaling. Figure 3.8c shows a 'translated' average of all the quiet images that

Sample Image

Simple Average

Translated Average

(a)

(b)

(c)

Magnetic Local Time (Hrs)

MLT
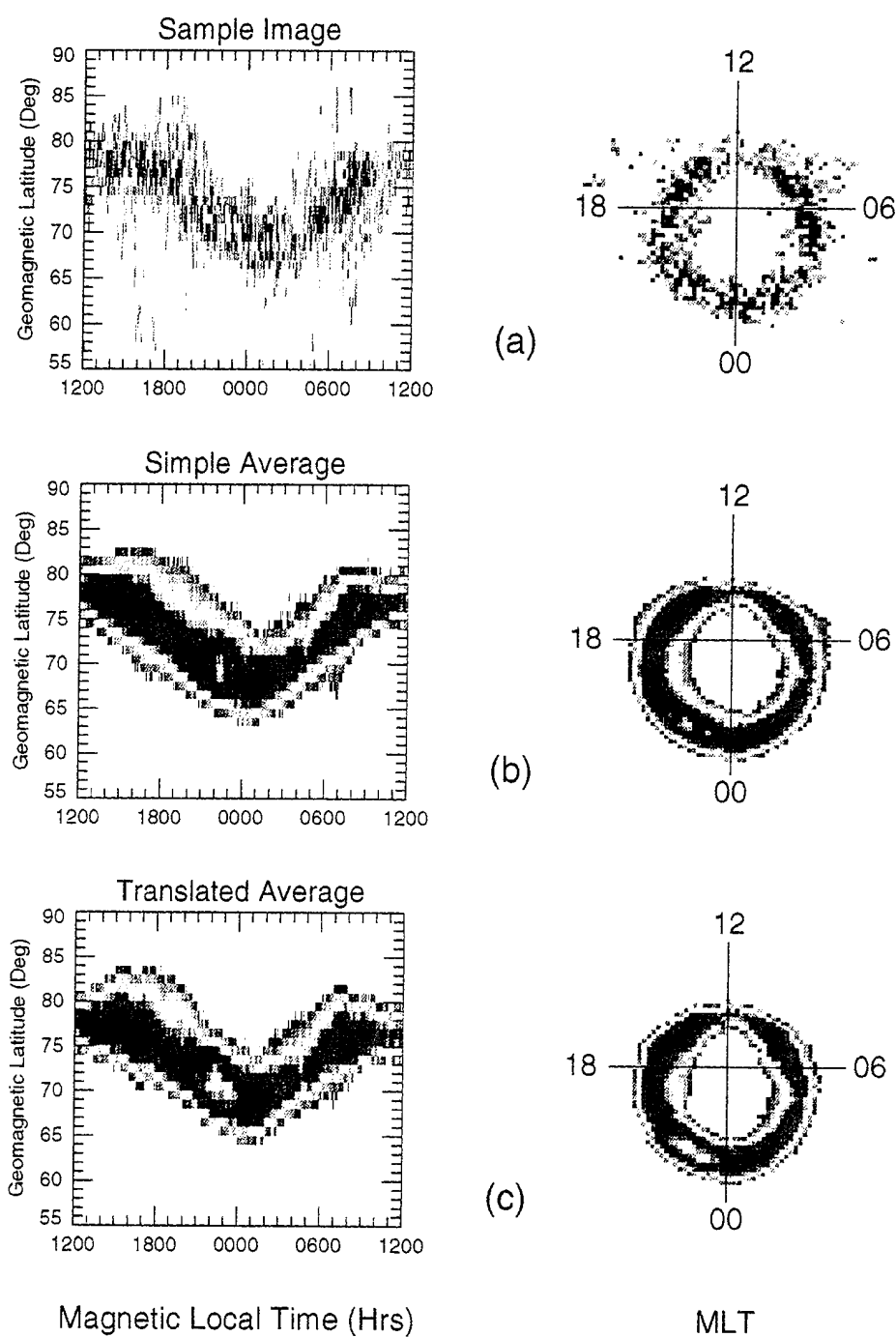
Figure 3.8 Depictions of (a) an single sample image, (b) a simple average of all images, and (c) a translated average of all the images. The left side of the figure shows Mercator projections of the auroral oval. The right side show polar projections of the same ovals.

will be discussed later in this chapter. A comparison of the single binned image to either of the means shows immediately why it is necessary to obtain a mean image. In the single image the viewer has a difficult time discerning the global scale pattern, while in the mean images a global structure is easily seen. Note that the nightside emissions outside the auroral oval are no longer visible in these mean images as opposed to the individual images of Figure 3.1. This is because the emissions caused by the precipitating photoelectrons from the conjugate sunlit hemisphere are generally weak and their spatial pattern is dependent on Universal Time. So on any large scale averaging the mean values of such emissions fall below the level of the color bar used here.

An average for all the quiet-time images was done to increase the number of counts per degree bin to improve the spatial resolution for localized discrete structures in the distribution. Such an averaging is considered acceptable due to the small observed variations in the dimensions of the oval. Two methods of averaging were found to be effective. The first method used for averaging was to simply overlay all the images with no scaling or adjustment of any kind and to sum and average the photometer response in each bin. This 'simple' average (Figure 3.8b) will be used as an initial check against the other averaging method. It is also the method of averaging used by other researchers presenting electron data (i.e., Spiro *et al.* [1982] and Hardy *et al.* [1985]).

The second averaging scheme 'translated' the images to fit the mean low-latitude boundary as defined earlier in this chapter. The LLB for each image was compared to the mean LLB of all images. In each one-hour magnetic local time sector the single image was translated to overlay its LLB with the mean LLB. This was done by defining a translation factor as the difference in geomagnetic latitude between the image LLB and the mean LLB at the same position, and then translating the hour 'pie' wedge of the image towards or away from the geomagnetic pole by the computed amount. In effect this

served to expand or contract the region of activity to the mean oval size. This translated average was done to eliminate some of the washing-out, or blurring of the boundaries seen in a non-translated average for differing instantaneous diameter for the auroral oval.

In both of the averages of Figure 3.8 relative maximums are apparent at about 2200-2400, 0730-0900 and 1400-1600 MLT. Without averaging, maxima in the morning and afternoon sectors are not easily distinguishable in the sample image shown in Figure 3.8a, but the maximum at ~2300 MLT can be seen. These maxima in the emission pattern are apparent in some of the single images and not in others. In some sequences an observer can see these maxima 'winking' on and off. Such variations in the individual images leads one to ask about the possible parameters that may influence such activity. Iijima and Potemra [1982, 1978] suggest that the parameter of interest is the IMF B_y component. This will be discussed later in this chapter. Comparison of Figures 3.8b and 3.8c shows an increase in the spatial size of the maximum at ~2300 MLT, and a slight narrowing of the over all oval width: In panel (b) the peak in the brightness of the maximum near 2300 MLT extends from ~2200 to 0000 MLT, while in panel (c) it extends from ~2100 to 0000 MLT. The maxima in the morning and afternoon sectors show little change between these averages.

Figure 3.9 shows cross-sectional views of the three images shown in Figure 3.8. The cross sections are of the unsmoothed images and therefore any comparison of the thresholds and features to those seen in Figure 3.8 will be approximate. The values in Figure 3.9 are more exact than the boxcar smoothed data displayed in the images of Figure 3.8. Each cross section is a slice along a given hour of magnetic local time (MLT) specified at the top of each panel. The sample representative image cross section is depicted by the solid line, the dotted line depicts the simple average cross section, and the dashed line is the cross section of the photometer response for the translated average
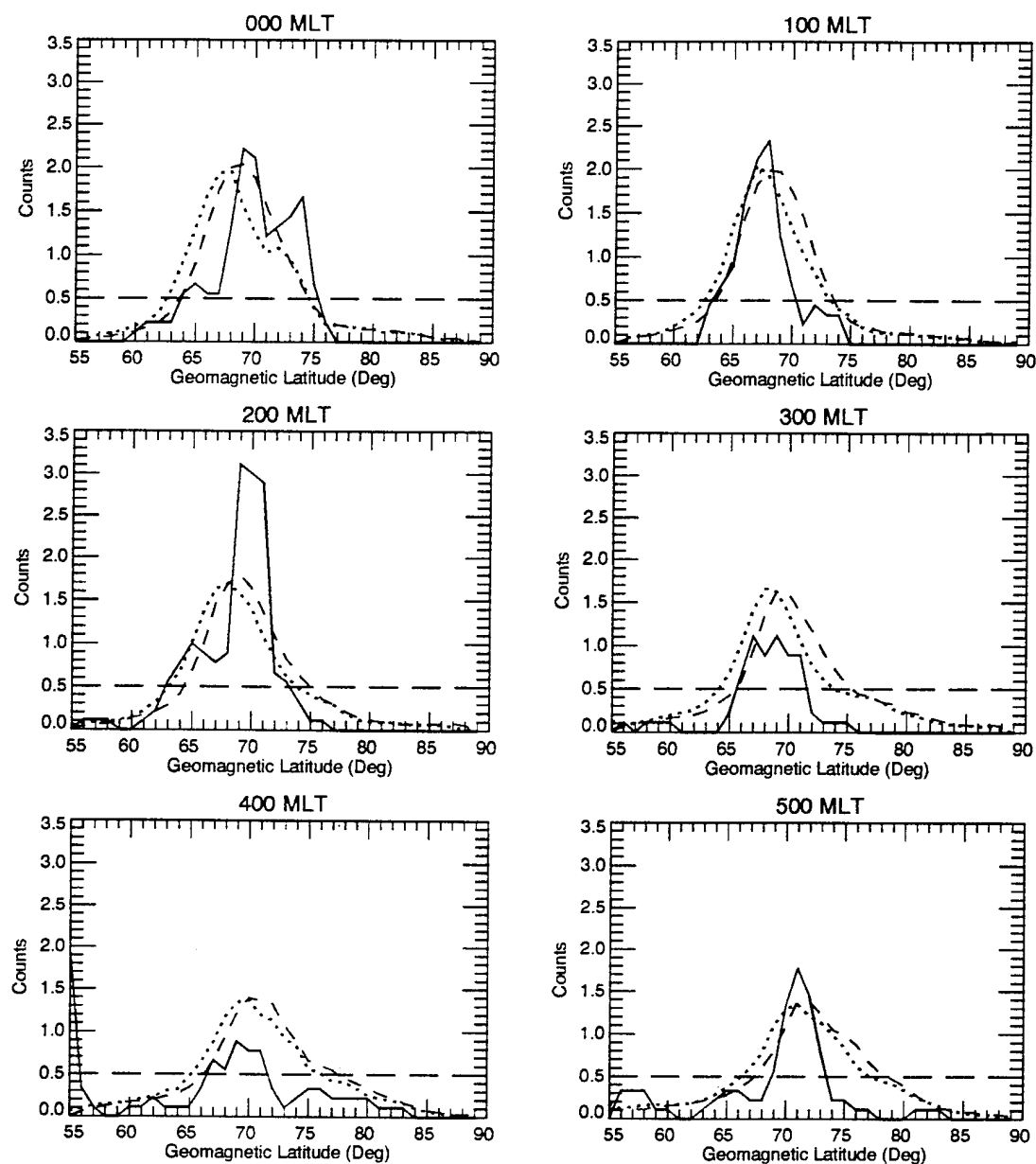
Figure 3.9   Latitudinal profiles of the images shown in Figure 3.6 for the magnetic local time given at the top of each panel. The solid line denotes the instantaneous image, the dotted line the simple average, and the dashed line the translated average.

54
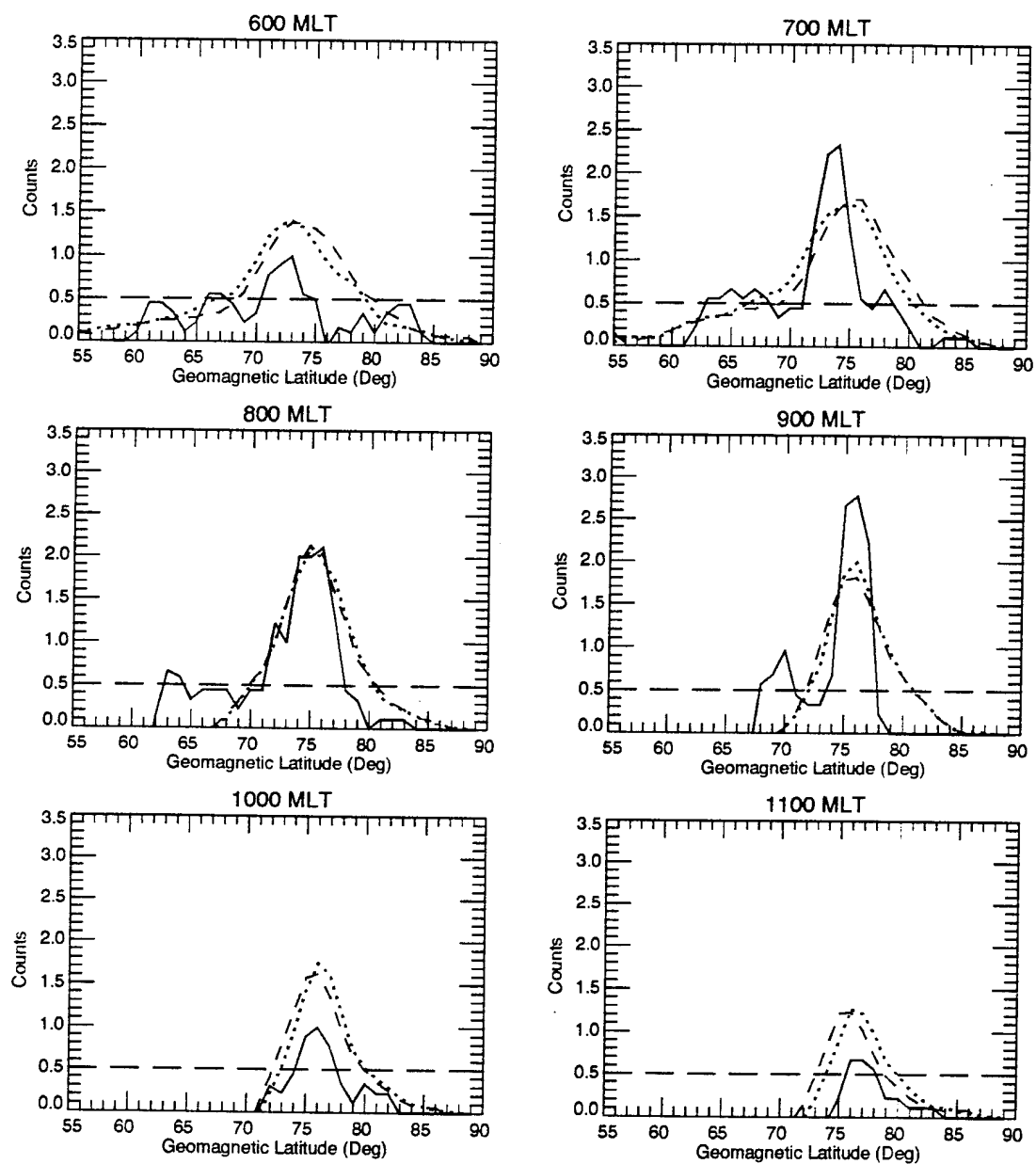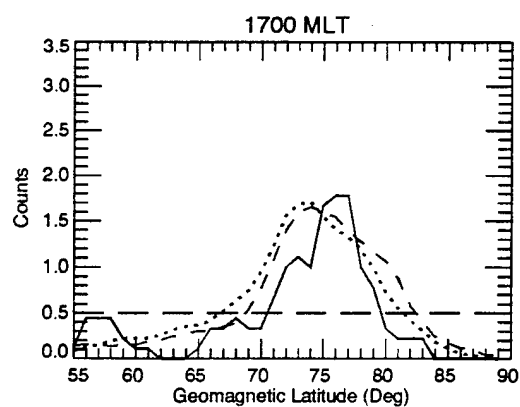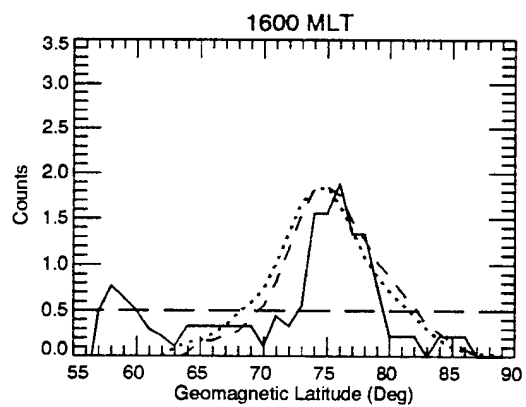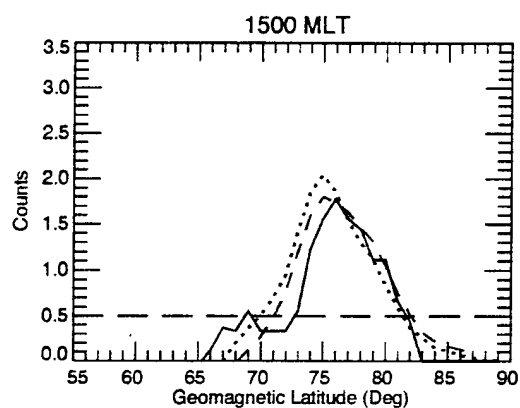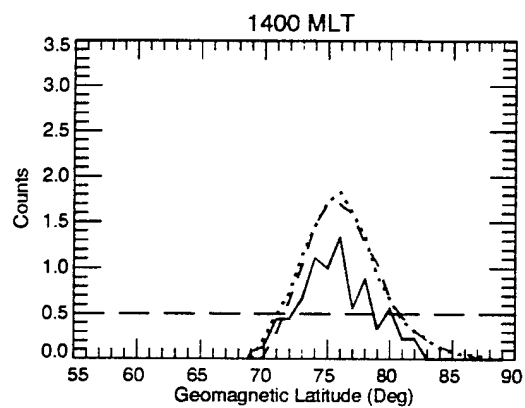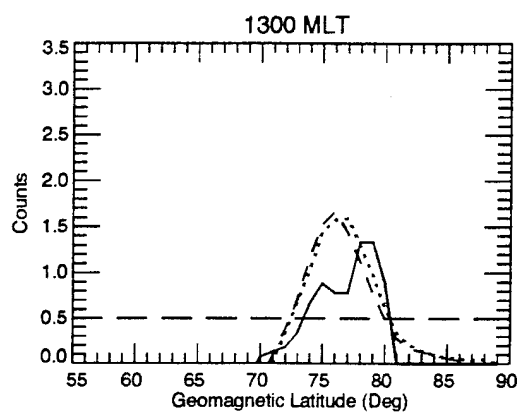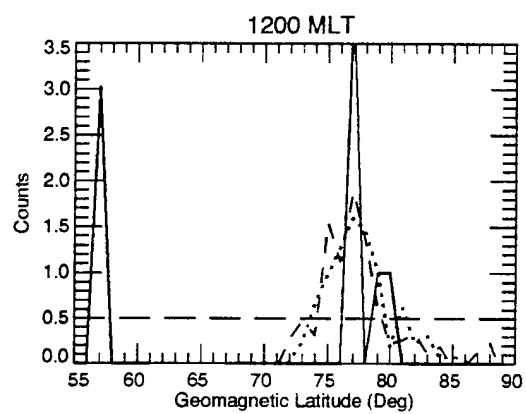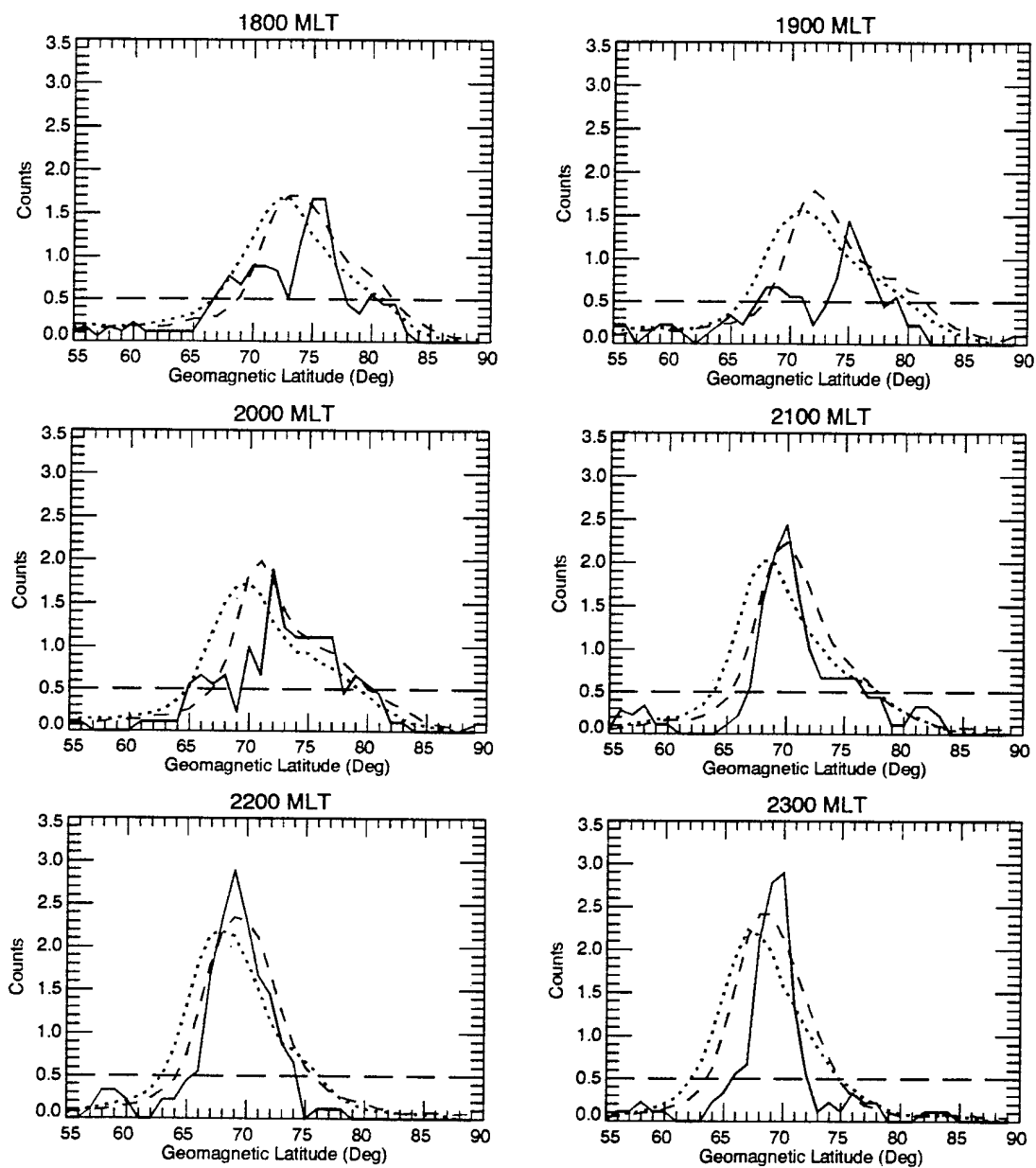
image. The horizontal dashed line marks the ½- count level, which is the threshold level in the color image displays and for the original contouring of the low-latitude boundary. Although the instantaneous image displays some short-lived features (on the time-scale of a single image) not found in the averages, it still compares favorably with them. A ratio of the translated average to the simple average shows that there is a mean difference of ±5% counts/pixel between the two averages, except in the midnight sector where the differences were as much as 25% . This comparison shows that for the most part there is little or no difference in the emission patterns between the simple and translated averages, except in the midnight sector. This may suggest that the translated average is not necessarily an improvement over the simple average for quiet-time auroral activity.

As a comparison for even more quiet conditions, the simple and translated averages for those images where the AE index went below 50 nT and remained so for the entire sequence are shown in Figure 3.10. For the simple averages the maximum at 2300 MLT appears to diminish in brightness, but the translated average shows the 2300 MLT maximum persisting. For AE < 50 nT both averages show the maximum in the morning sector decreasing in brightness, and the maximum in the afternoon sector remaining about the same. The overall dimensions of the oval don't change significantly between the AE < 100 nT averages and the AE <50 nT averages. A ratio of the AE < 50 nT to the AE < 100 nT averages shows the mean differences between either of the averages is on the order of ±10% counts/pixel. This is not a significant difference in the emissions since it is generally on the order of only two tenths of a count, and there is no systematic pattern to the differences. The AE < 50 nT average emissions were not uniformly less those for the AE < 100 nT averages.

An analysis of the translated averaging scheme is depicted in Figures 3.11 and 3.12. Figure 3.11 shows histograms of the increments in latitude used for the translations for

Simple Average

Translated Average

Magnetic Local Time (Hrs)

MLT
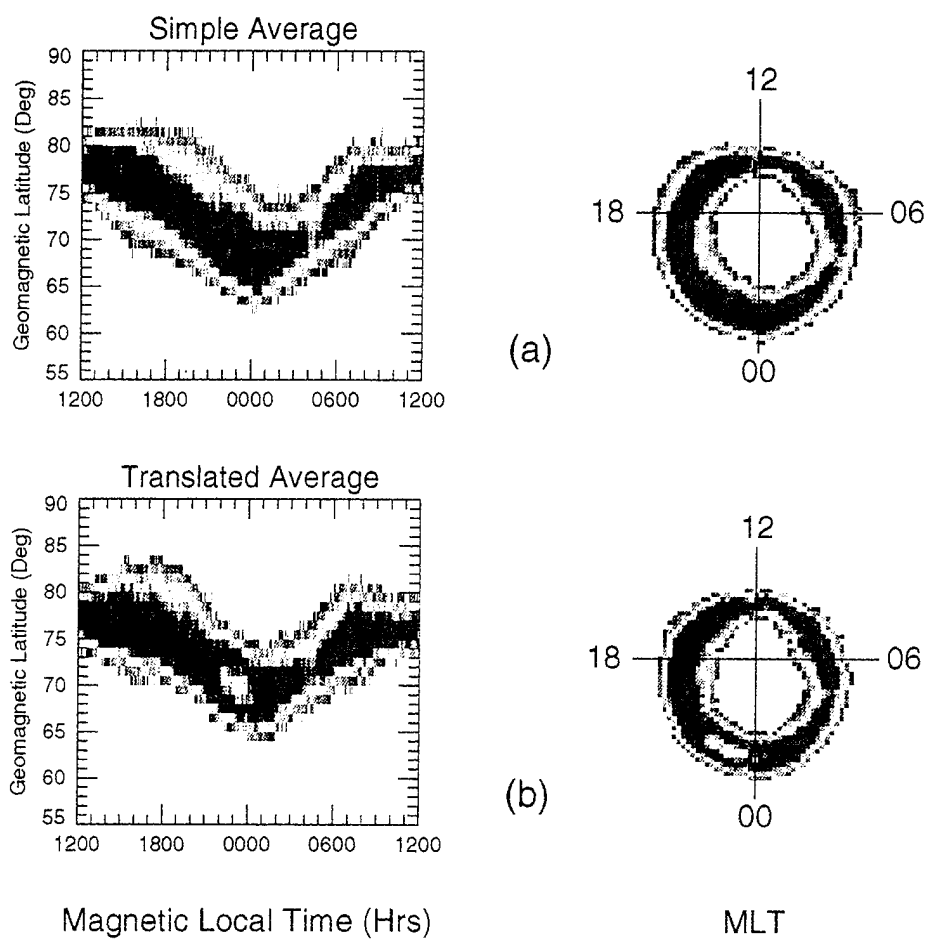
Figure 3.10   Depictions of the (a) simple average and (b) translated average for those images where the AE was below 50 nT for the entire imaging sequence. The left side of the figure shows a Mercator projection of the auroral oval. The right side shows a polar projection of the same ovals.
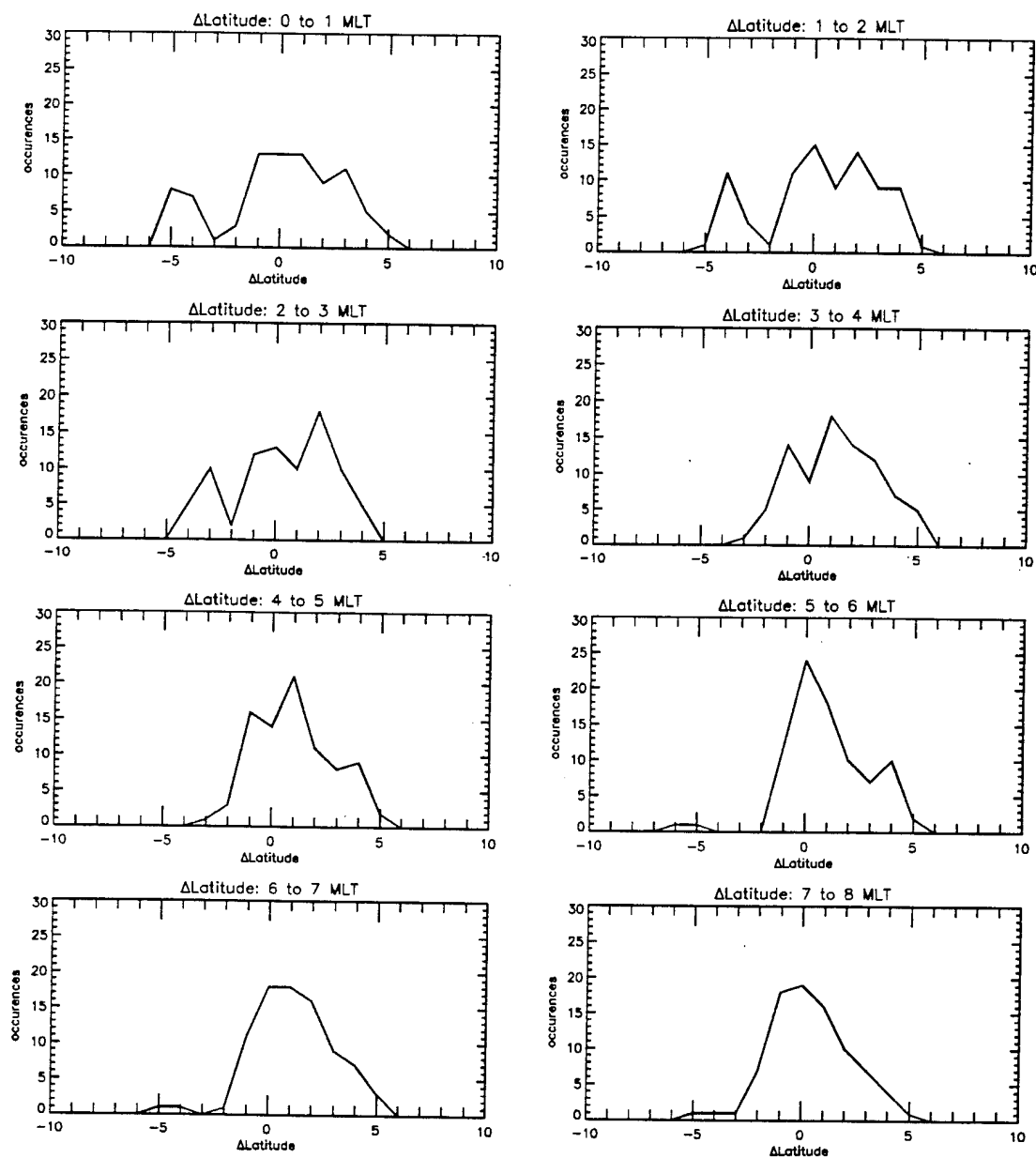
Figure 3.11 Histograms of the change in latitude used for the translated average for each one-hour of magnetic local time (given at the top of each panel).
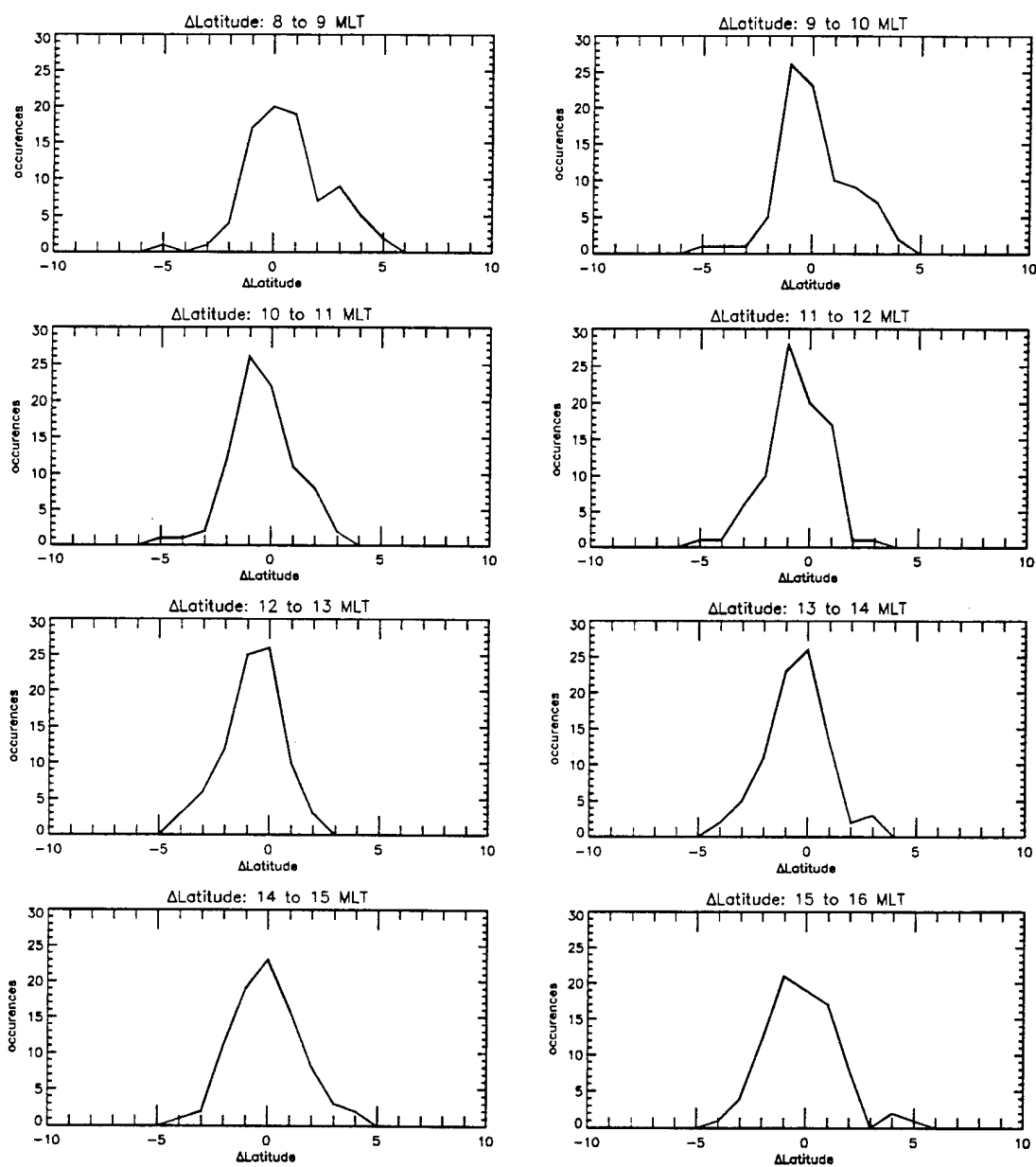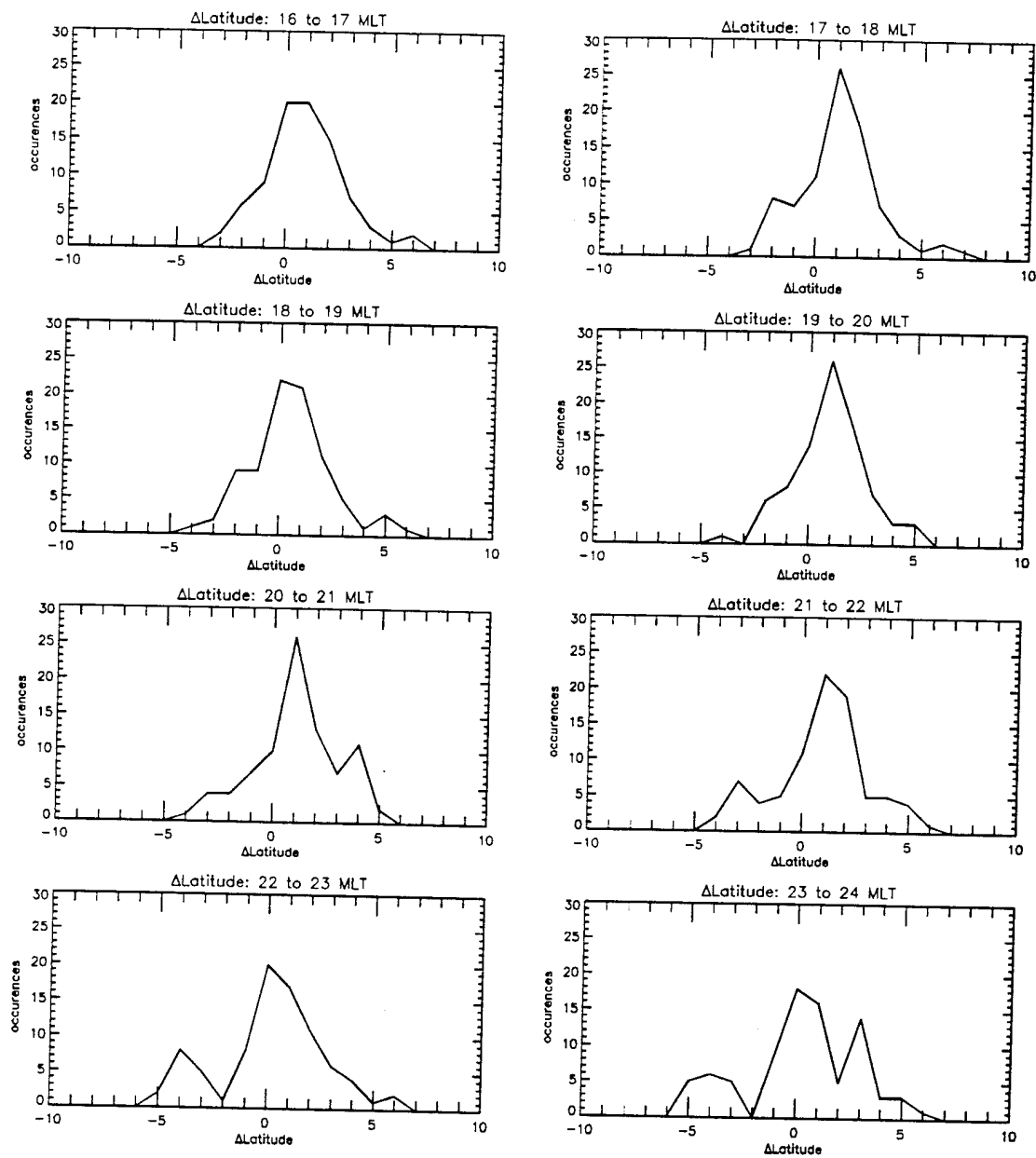
each one-hour magnetic local time sector. While each distribution peaks within 2° of zero translation, the range of translation runs from -6° to +7° of latitude. Figure 3.12 depicts a histogram of the low latitude edge of the mean oval for the simple average (solid line) and the translated average (dotted line). To get above some of the noise, these 'edges' depicted are for the location of the first bin with a count/pixel ≥ 1. This low-latitude edge does not necessarily correspond to the edge seen in the color images of Figure 3.8 due to the smoothing of the color images for display. The plots in Figure 3.12 show that the translation scheme of averaging does eliminate some of the blurring of the low-latitude edge of the auroral oval seen in a simple average.

The sample image displayed in Figure 3.8a makes the need for an average for the quiet-time electron precipitation apparent. A simple average was done as a first approximation of the mean global electron precipitation pattern. An improved method for calculating the average was investigated in an attempt to limit the 'blurring' of the pattern boundaries. The method of translating portions of the oval to a mean low-latitude boundary is shown here to have some impact on the dimensions and brightness of various features of the precipitation pattern, but no systematic improvement over the simple average is seen. By comparing the 100-nT threshold data set averages with a set of 50-nT threshold averages it has been shown that the differences are minimal for the location, size, and brightness of the precipitation pattern features.

Dependence on IMF Orientation

To investigate the suggested dependence of the emission patterns on the IMF orientation, the images in this data set were divided into subsets based on the sign of the IMF B_y and B_x components. The orientation of the IMF was determined using the hourly averages compiled in the Interplanetary Medium Data Book - Supplement 3A,
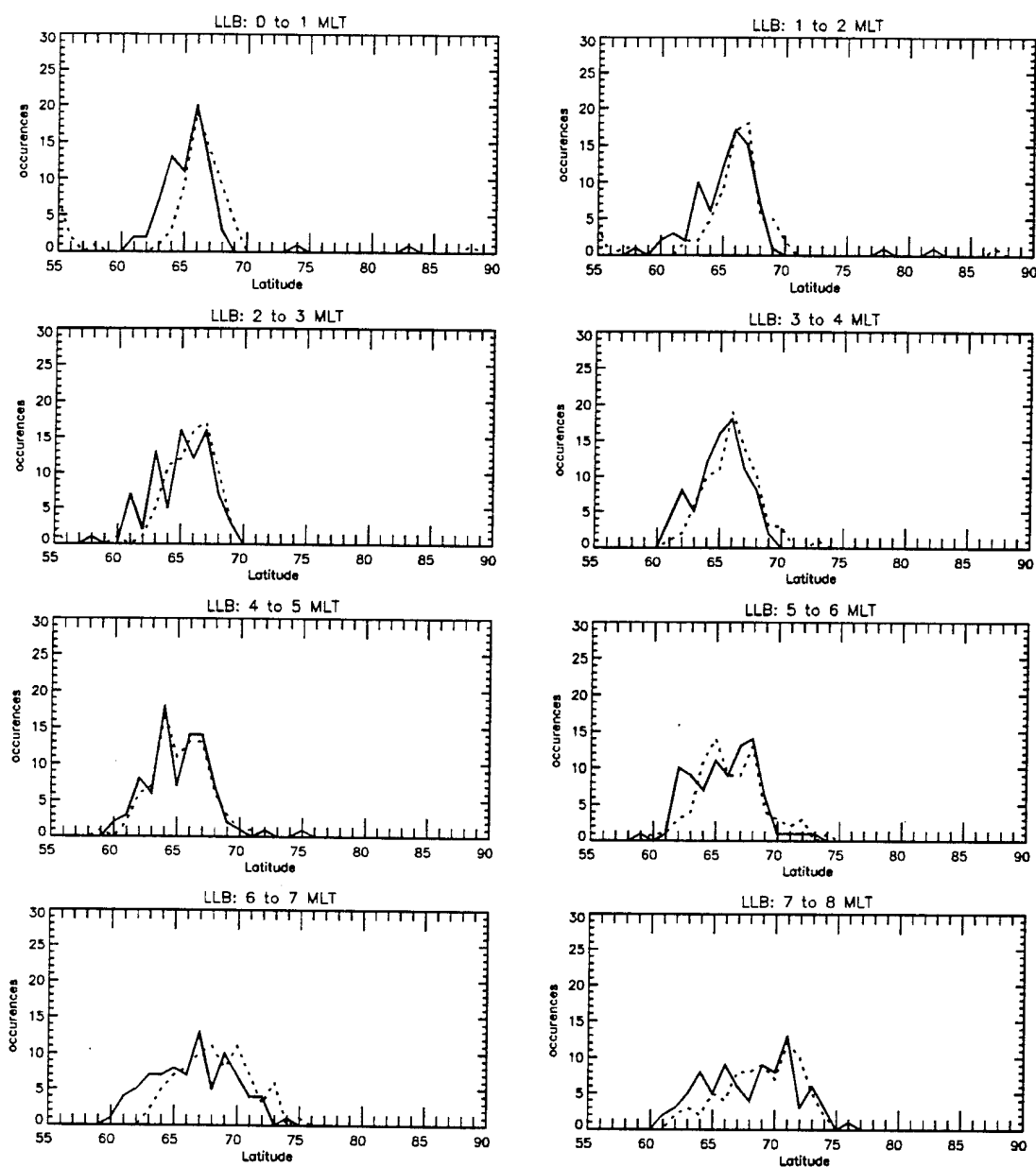
Figure 3.12 Histograms of the hourly average first low-latitude bin where the counts are ≥ 1. The solid line denotes the simple average values and the dotted line depicts the translated average values.

LLB: 8 to 9 MLT

LLB: 9 to 10 MLT

LLB: 10 to 11 MLT

LLB: 11 to 12 MLT

LLB: 12 to 13 MLT

LLB: 13 to 14 MLT

LLB: 14 to 15 MLT

LLB: 15 to 16 MLT
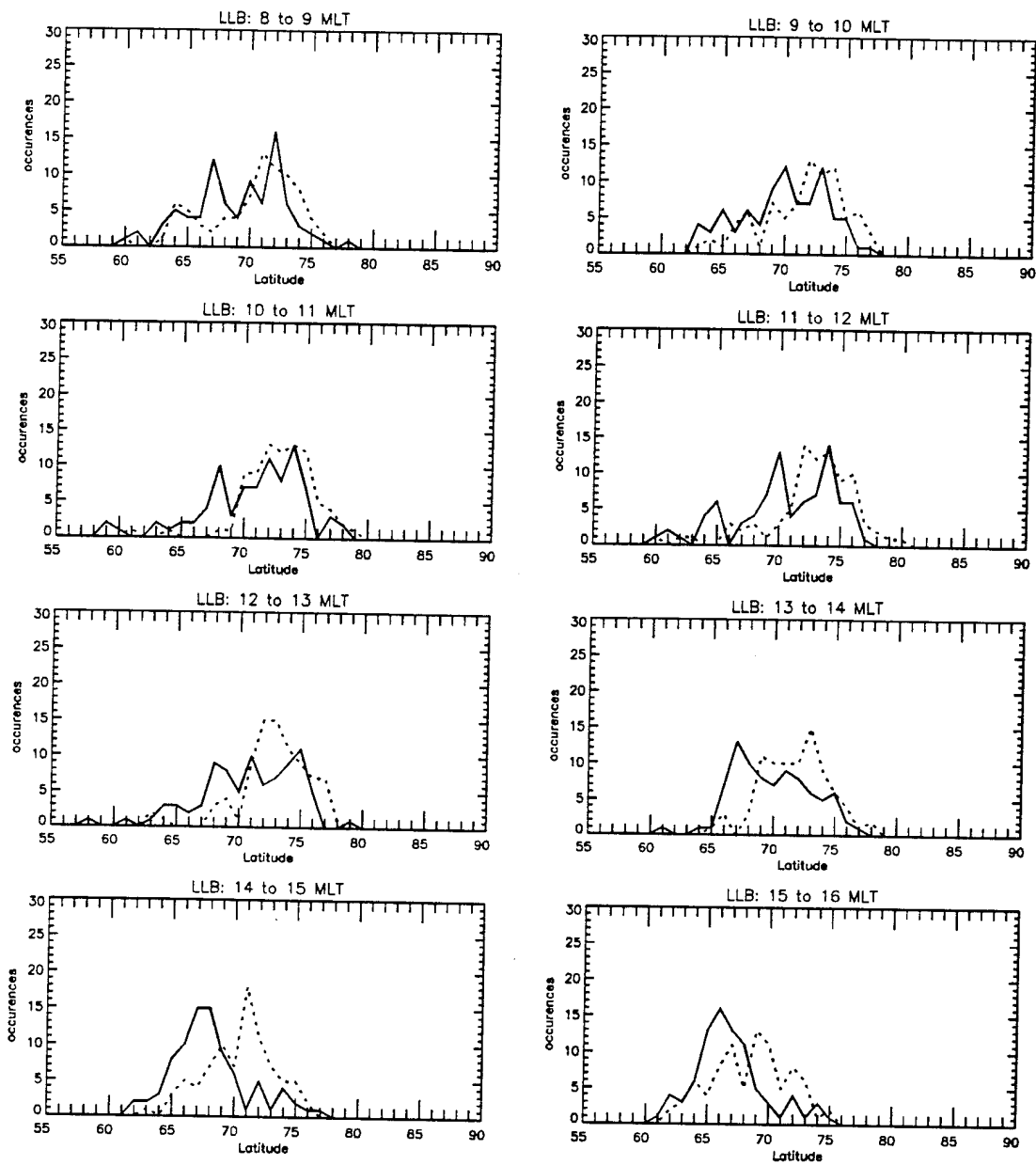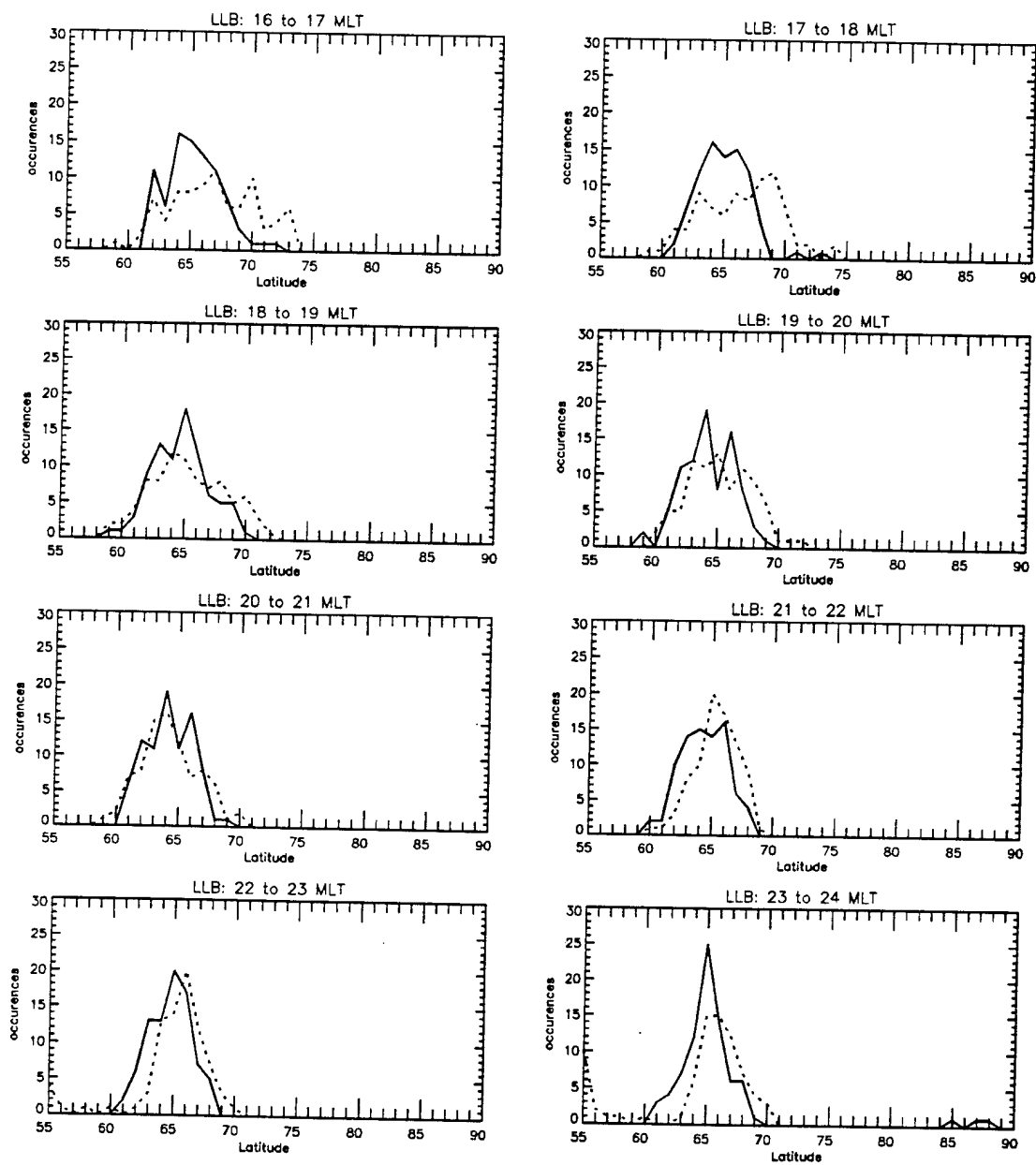
1977-1985 (National Space Science Data Center, World Data Center A for Rockets and Satellites). These subsets were the four quadrants of the B_{xy} plane. The average images for these subsets are seen in Figure 3.13 and 3.14. The B_{xy} plane is oriented in these figures such that positive B_x is sunward and positive B_y is toward 1800 MLT (the left). Figure 3.13 shows the Mercator projections of the average auroral oval for the B_{xy} components. There are 19 images used in the Quadrant-I average, 14 images for the Quadrant-III average, and 39 for the Quadrant-IV average. Only one image is available in Quadrant-II, and it is extracted from a series where the IMF changes direction several times during imaging. In the data set used for this research there are no entire sequences where the B_{xy} component is in quadrant II for the entire orbit. Figure 3.14 show the same averages depicted as polar projections. The color bar used for these images ranges from <0.5 counts to >4.5 counts as depicted in Figure 3.7 (values to the right of the color bar).

The dependence on the orientation of the IMF is evident in the maxima that were mentioned earlier. In Quadrant I (B_x and B_y positive) the maximum at ~2300 MLT extends from 2100 to 0200 MLT. In Quadrant III (B_x and B_y negative) the entire evening sector is brighter than in Quadrant I. There are also significant increases in the brightness of the maxima in the morning and evening sectors, with the maximum at ~0800 MLT doubling from Quadrant I to Quadrant III. Quadrant IV ($B_x >0$ and $B_y < 0$) shows significant bulging in the pre-midnight-sector of the oval. There is also a ~1 hour shift in the midnight maxima from ~2300 MLT to ~2200 MLT as well as a poleward expansion. Although Quadrant II contains only one image (smoothed with a 5x5 boxcar), if we assume it to be representative of the mean when $B_x < 0$ and $B_y > 0$, then one can discern an increase in the overall oval brightness compared to the other quadrant averages. The two 'tails' at about 1600 and 0800 extending from 55° to 70° latitude are artifacts of the

+Bx

Quadrant I

Quadrant IV

+By

-By

Quadrant II

Quadrant III

-Bx
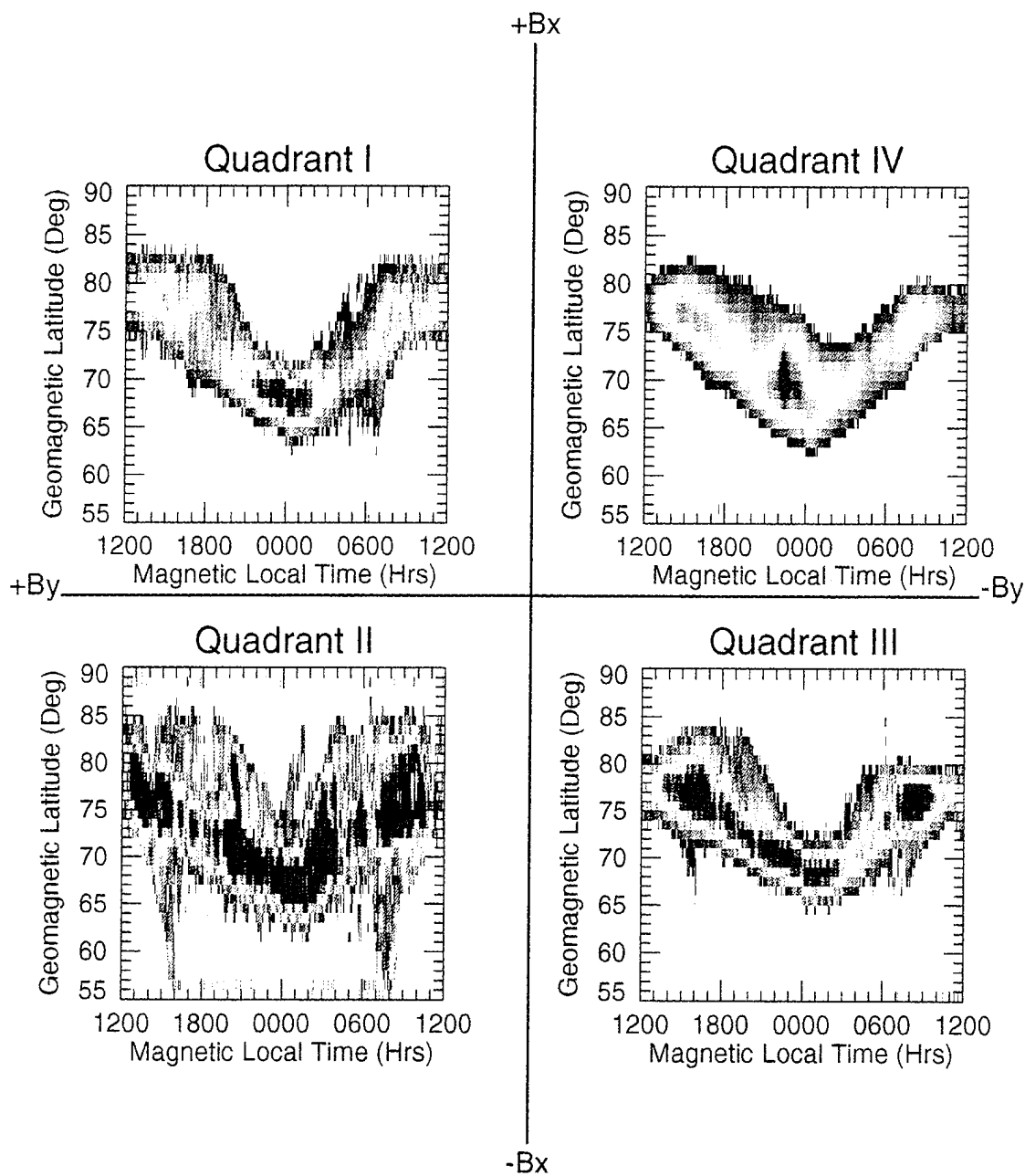
Figure 3.13 Mercator projections of the simple averages for images in the four quadrants of IMF Bx-By plane. Positive Bx is sunward (top of page) and positive By is toward 1800 MLT (left side of page).
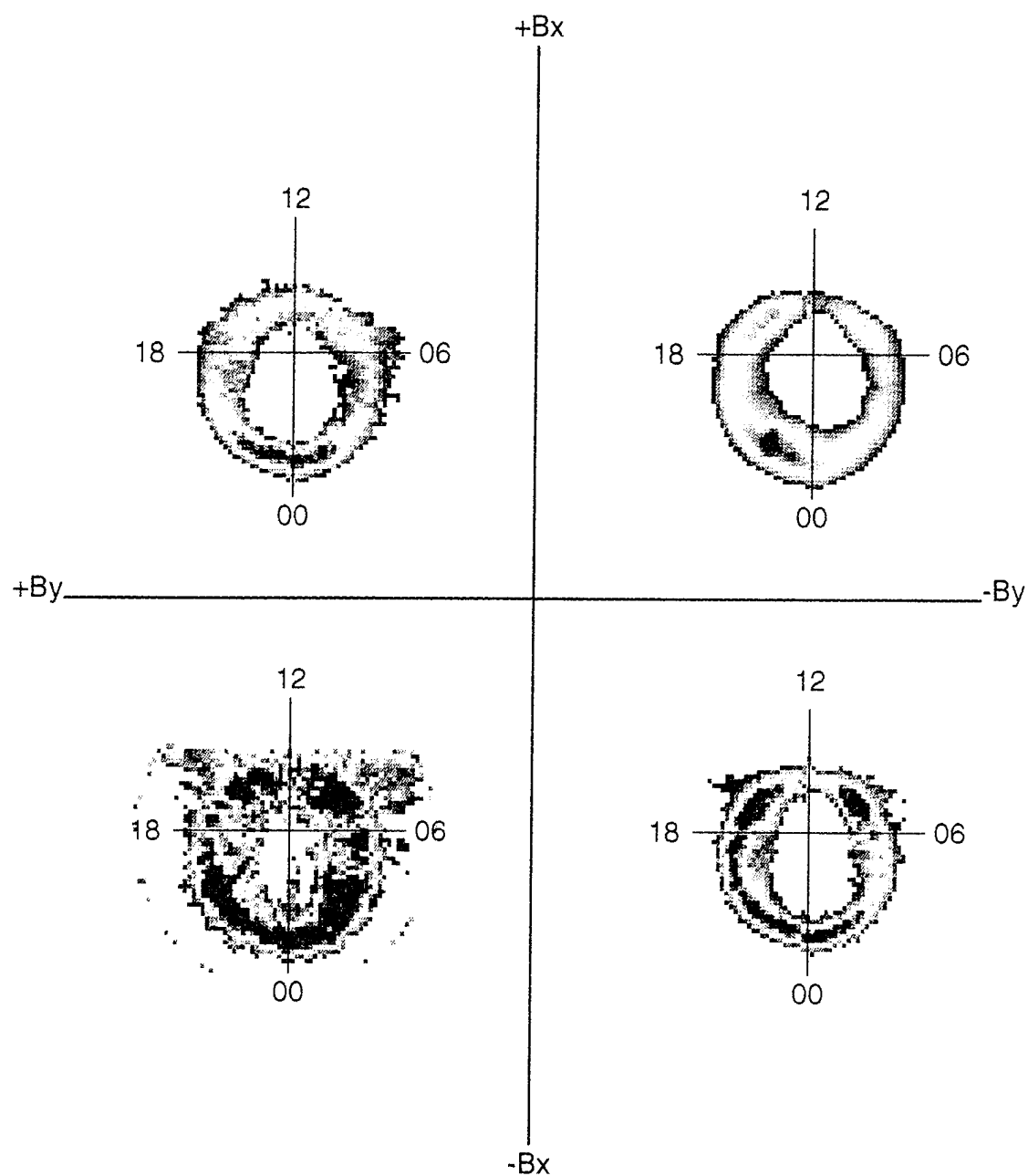
Figure 3.14   Polar projections of the simple averages for images in the four quadrants of IMF Bx-By plane. Positive Bx is sunward (top of page) and positive By is toward 1800 MLT (left side of page).

dayglow model subtraction. This thin sliver of dayglow appears in some of the single images but is minimized when the images are averaged. Also visible in this image are some arcs reaching into the polar cap.

Such changes in the precipitation patterns can be seen clearly in a sequence of individual images where the IMF changes orientation. Figure 3.15 shows one such imaging sequence for December 3, 1981, during which the IMF components change sign. The solid dark line in each image denotes the visually estimated low-latitude boundary for that image. A plot of the IMF components measured in 5-minute averages taken from the ISEE-3 spacecraft for the same period is shown in Figure 3.16. The times have been adjusted by 65 minutes to take into account a mean solar wind speed of 387 km/s during this period and a spacecraft distance of ~1,500,000 km from the Earth. The vertical dashed lines are the start and end imaging times for the sequence in Figure 3.15. The horizontal solid line in each panel depicts the zero line. The B_z component is positive at the start of imaging and becomes negative from ~0420 to 0450 UT, then turns positive and remains through the rest of the imaging time. The B_y component is negative at the start of imaging, becomes positive at ~0400 UT, then alternates from positive to negative between 0445 UT and the end of imaging. The B_x component is positive at the start of imaging and drops below zero from ~0400 to 0435 UT, oscillates about zero until 0450 UT, then remains positive through the rest of the imaging period. The plot of the AE-index for this sequence, shown in Figure 3.17, shows that imaging started five hours after an isolated substorm peak of 400 nT, and that the AE had remained below 100 nT for more than four hours before the start of imaging.

Visible in this sequence of images is an arc developing across the polar cap. In the image for 0456:33 UT there are a few consecutive scan lines missing that show up as white lines through the morning and afternoon sectors of the oval. The breakdown of the

0343:40 UT

0355:49 UT

0407:58 UT

0420:06 UT
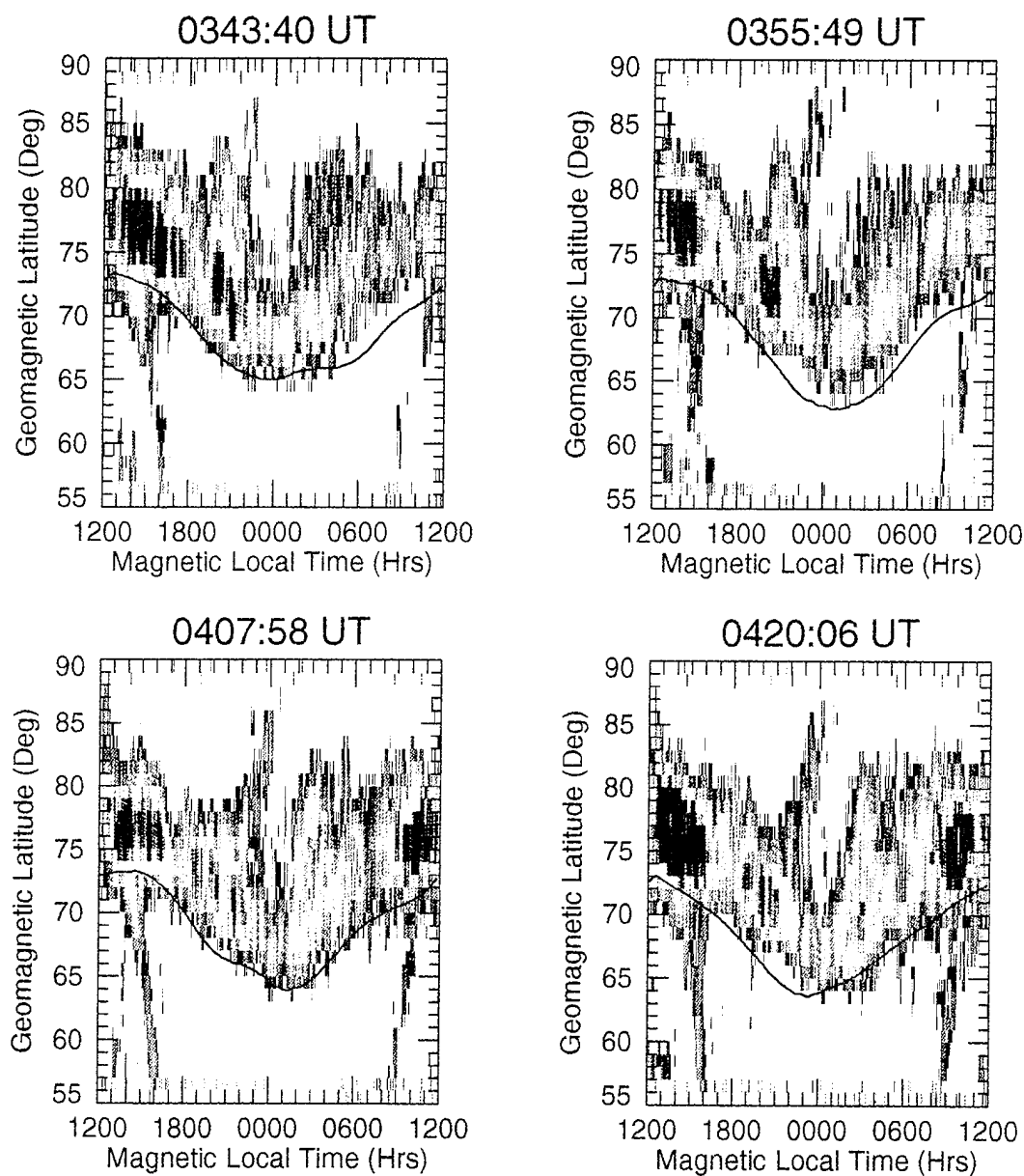
Figure 3.15 Mercator projections of an imaging sequence for 3 December, 1981. The start image time is given at the top of each panel. The IMF components change sign during this sequence, as shown in Figure 3.16.

0432:15 UT
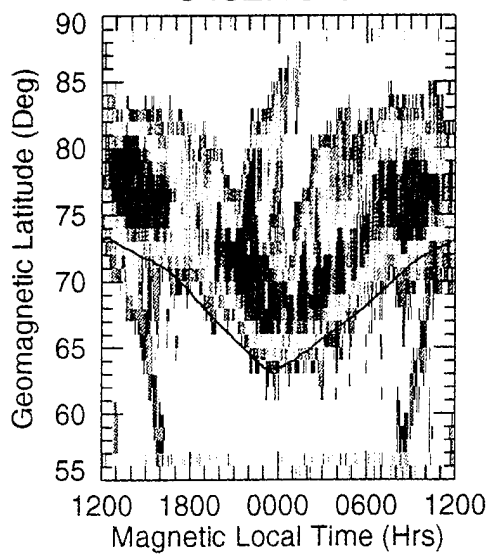
0444:24 UT
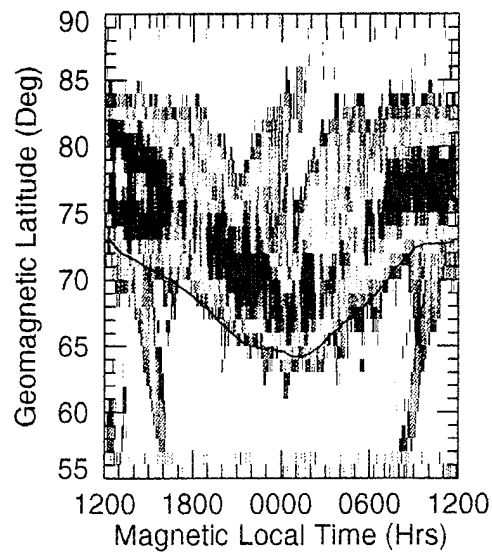
0456:33 UT
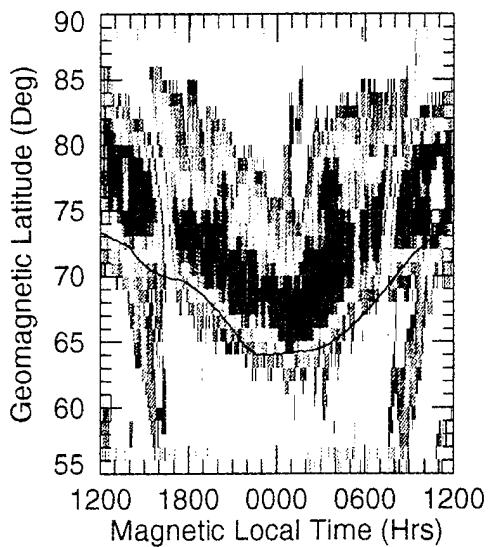
0508:42 UT
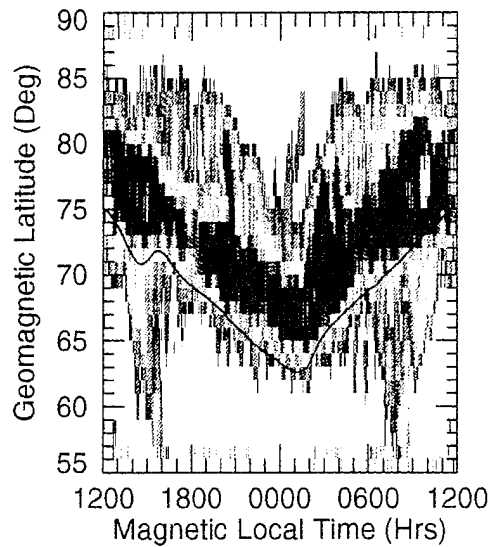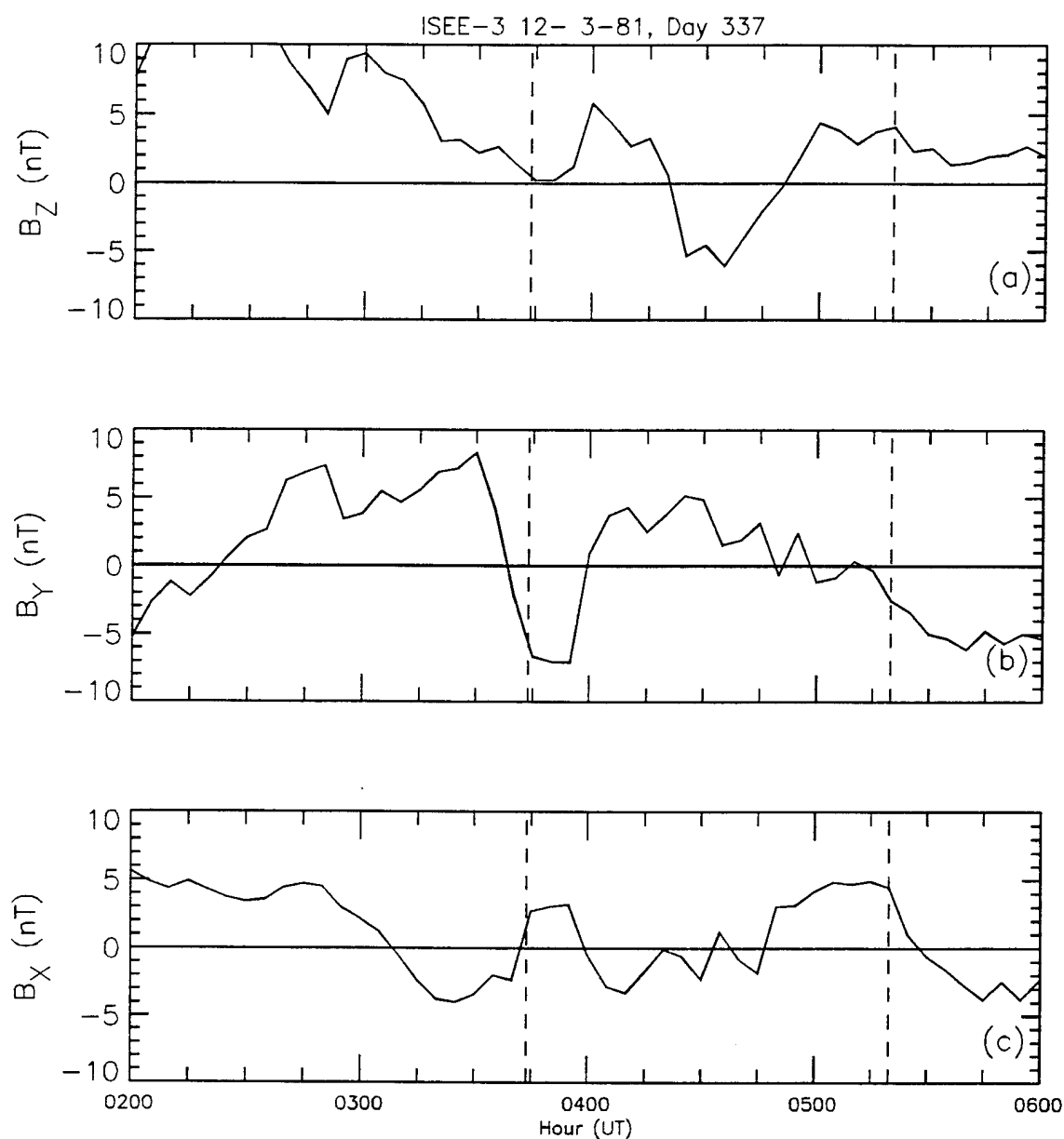
Figure 3.16 Plots of the IMF components measured by the ISEE-3 spacecraft for the period of interest shown in Figure 3.15. The vertical dashed lines represent the start and stop imaging times of the sequence. The horizontal solid line shows the zero level for each plot. The data have been shifted 65 minutes to adjust for ISEE-3 position and solar wind speed at the time of the sampling.

72
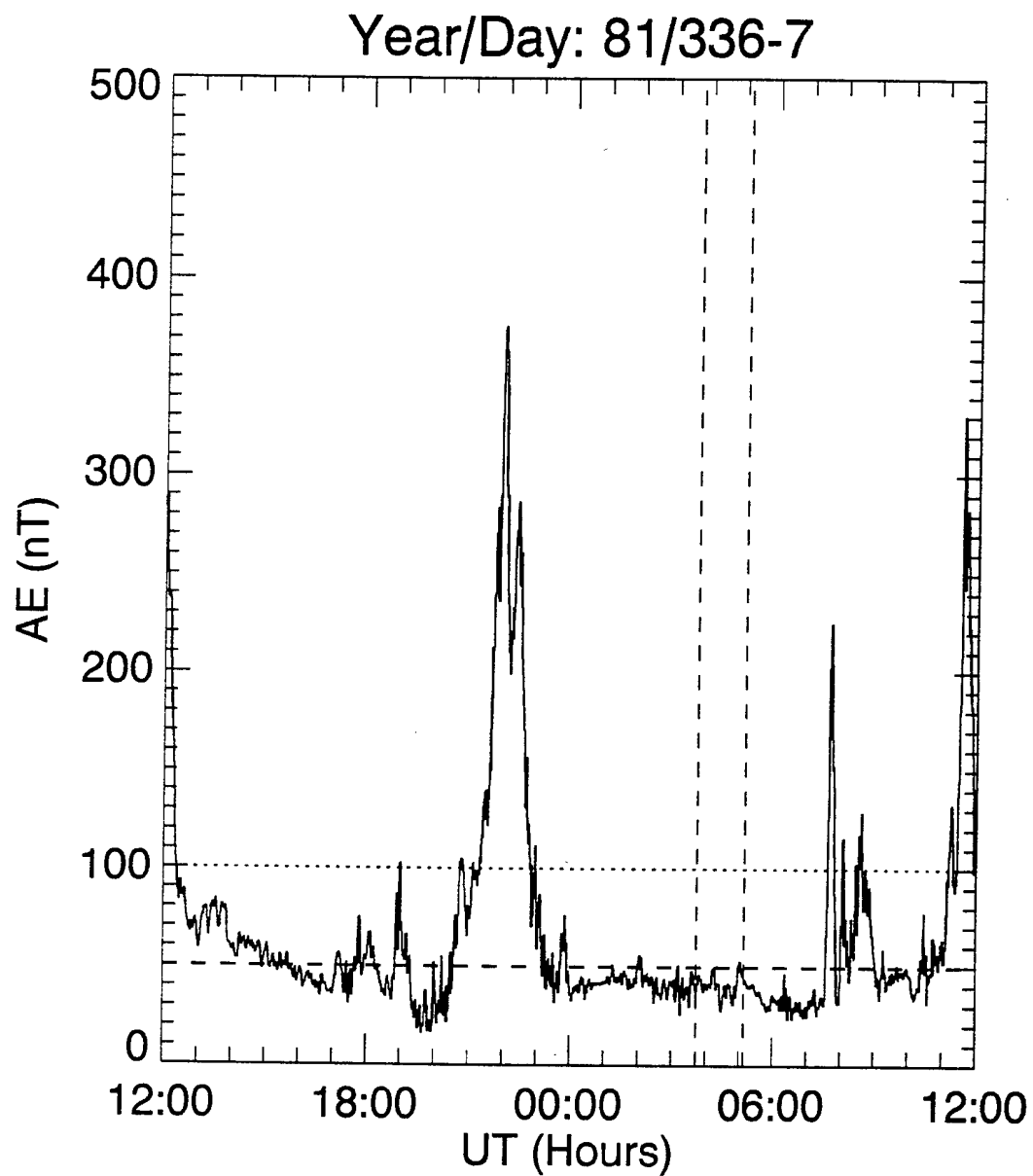
Figure 3.17 A plot of the AE index versus time UT for the period of interest shown in Figure 3.15. The vertical dashed lines are the start and stop imaging times for the sequence. The horizontal dotted line shows the 100-nT threshold used for this research. The horizontal dashed line depicts a 50-nT threshold.

dayglow model along the terminator is apparent in these images from the 'tails' that appear on the dayside.

The first three images of the sequence shown in Figure 3.15 show a trend of decreasing activity as the B_z has been positive for more than seven hours prior to the start of imaging. The maximum seen at ~1500 MLT in the 0343:40 UT image is the only structure of the dayside maxima identified previously that is readily apparent, but begins to diminish in successive images as B_y becomes positive. When B_x becomes negative at about 0400 UT there is an increase in brightness of the maximum at ~1000 MLT. The maxima in the morning and afternoon sectors increase in brightness during these and subsequent images. The maximum near 1500 MLT appears to reach a peak brightness during the 0444:24 UT image, while the maximum in the morning sector continues to increase in brightness. The peak in the afternoon sector maximum may be associated with the turning of the B_y component towards negative values. The maximum in the midnight sector of the oval is closely associated with the B_z becoming negative. This brightening persists even after B_z has become positive again. This may indicate that it takes longer for the oval to recover from a change in the IMF B_z component than it does from the other components. This sequence of images is a good example of how responsive the precipitation patterns of the auroral oval are to variations in IMF orientation.

The dependence of the precipitation patterns on IMF orientation has been shown by other researchers (i.e., Iijima and Potemra [1982, 1978]; Newell and Meng [1992]). The results shown here differ very little from such results, and will be discussed in Chapter 5. The categorizing of the images in quadrants based on the IMF B_{xy} component's orientation does hint that the precipitation pattern is as much a result of the x-component as the y-component, possibly more so. The example images given in Figure 3.15 show how quickly the auroral precipitation pattern responds to changes in the IMF.

The patterns found during this analysis of the quiet time auroral oval are the stepping stone to the investigation of the morphology of the auroral oval patterns during more active periods. While these images were obtained by photometric methods, they compare fairly well with particle measurements used by other researchers. An investigation and comparison with other research was done and is outlined in Chapter 4.

CHAPTER 4

A COMPARISON WITH OTHER RESEARCH

Many studies of the auroral electron precipitation patterns have been done over the years, and many of these studies have used particle detector instruments on low-altitude polar orbiting platforms. One of the advantages of an *in situ* particle detector is that it samples electron energy fluxes directly, and from these measurements one can readily derive two parameters: the characteristic energy and mean energy flux of the electron spectrum. The emission patterns found in this research are also directly related to the characteristic electron energy and electron energy flux patterns in the auroral oval. The results of this research are compared here with the work of Spiro *et al.* [1982] and Hardy *et al.* [1985]. This was done to provide an additional level of confidence in the photometric data.

Comparison with Particle Detectors

To compare these results with those obtained using particle detectors, it is necessary to either relate the imaging data to characteristic energies and energy fluxes, or to relate known characteristic energies and fluxes to the photometer's response. The latter approach was the only one possible at this stage. To go from the Dynamics Explorer images to characteristic energies and energy fluxes would mean that one would have to make an assumption about the distribution of one of these two parameters. To get from

the particle data to the photometer's response, one has two known parameters, the characteristic energy and energy flux, and from these, one calculates the photometer response, in counts/pixel. To do the reverse there is only one known, the photometer's response, while trying to calculate two quantities, the characteristic energy and energy flux. Some uncertainties can be minimized by calculating a ratio of emissions measured simultaneously at two wavelengths and relating the ratio to the energies, as was shown possible for the visible wavelengths by Rees and Luckey [1974]. This research only deals with one filter in the FUV, and DE 1 was equipped with only one FUV photometer. At best one may be able to find a relationship for the characteristic energies and energy fluxes by using a ratio between two filters that alternate during an imaging sequence. Derivation of such a relationship was outside the scope of this research.

The data tables of Spiro $et\ al.$ [1982] give the average characteristic electron energies and energy fluxes (in units of ergs cm^{-2} s^{-1}) for precipitating auroral electrons when AE $\leq$ 100 nT. From Lummerzheim's data [Lummerzheim and Lilensten, 1994] one can get a relationship between the count rate per unit energy flux and the characteristic energy. Figure 4.1 depicts the count rate per unit energy flux as a function of the characteristic energy. This figure is the same as Figure 2.4, but here the quantities plotted are the upper and lower bounds and the mean value. Recall that upper and lower bounds arise from the different model runs where Lummerzheim varied several physical parameters. Using the data set from Spiro $et\ al.$ [1982] and the mean curve from Lummerzheim's calculations, one can generate an average 'image' of the particle data for AE $\leq$ 100 nT. Figure 4.2 shows this 'image' plotted in the same format as those seen in Chapter 3.

Figures 4.2a and 4.2b depict the simple and translated averages from DE 1, respectively. These are the same averages presented in Chapter 3, but have been rebinned
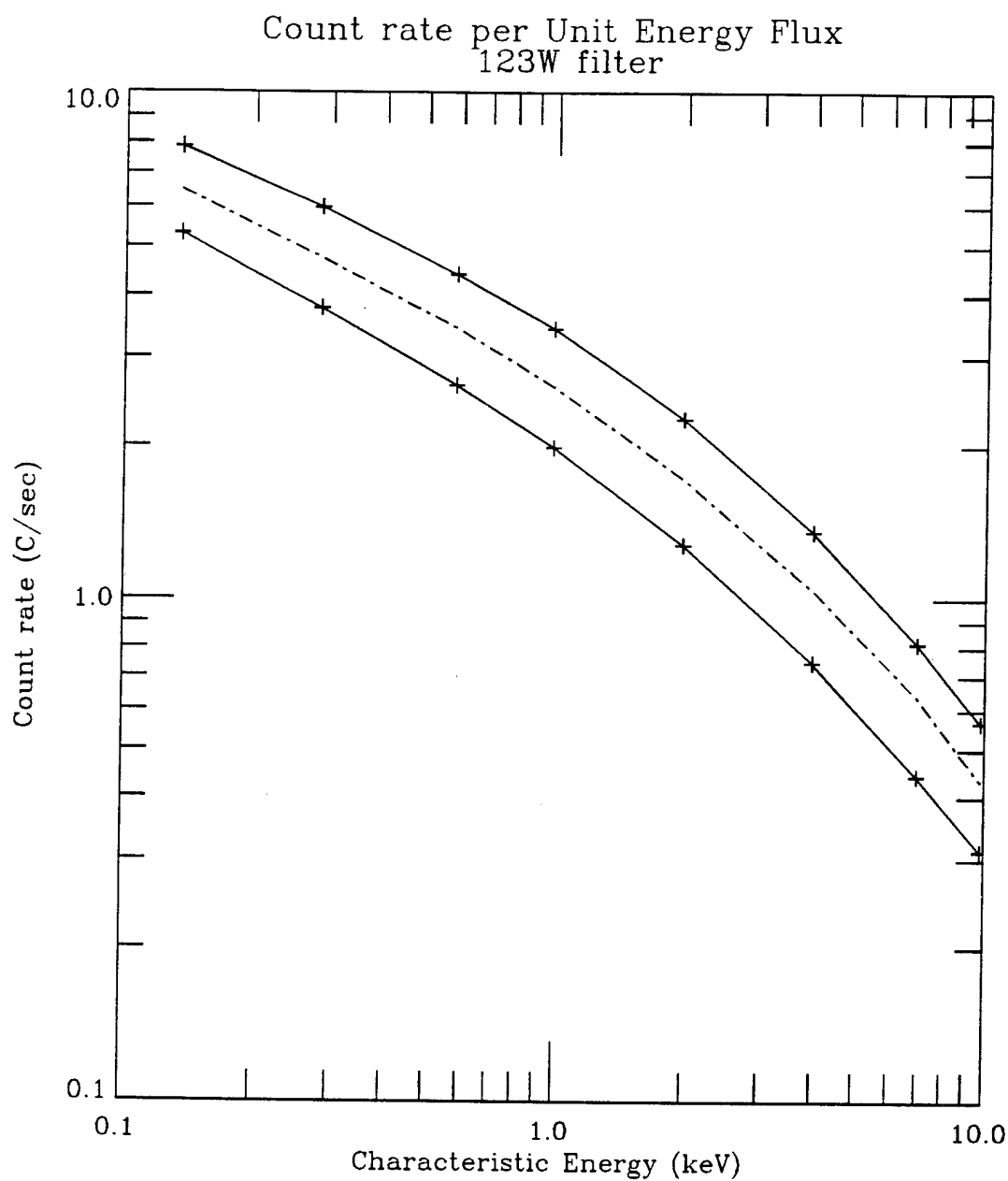
Figure 4.1 Plot of the lower and upper bounds and the mean fit to Lummerzheim's calculations of count rate per unit energy flux of the DE-1 photometer C (123W filter) as a function of characteristic energy.
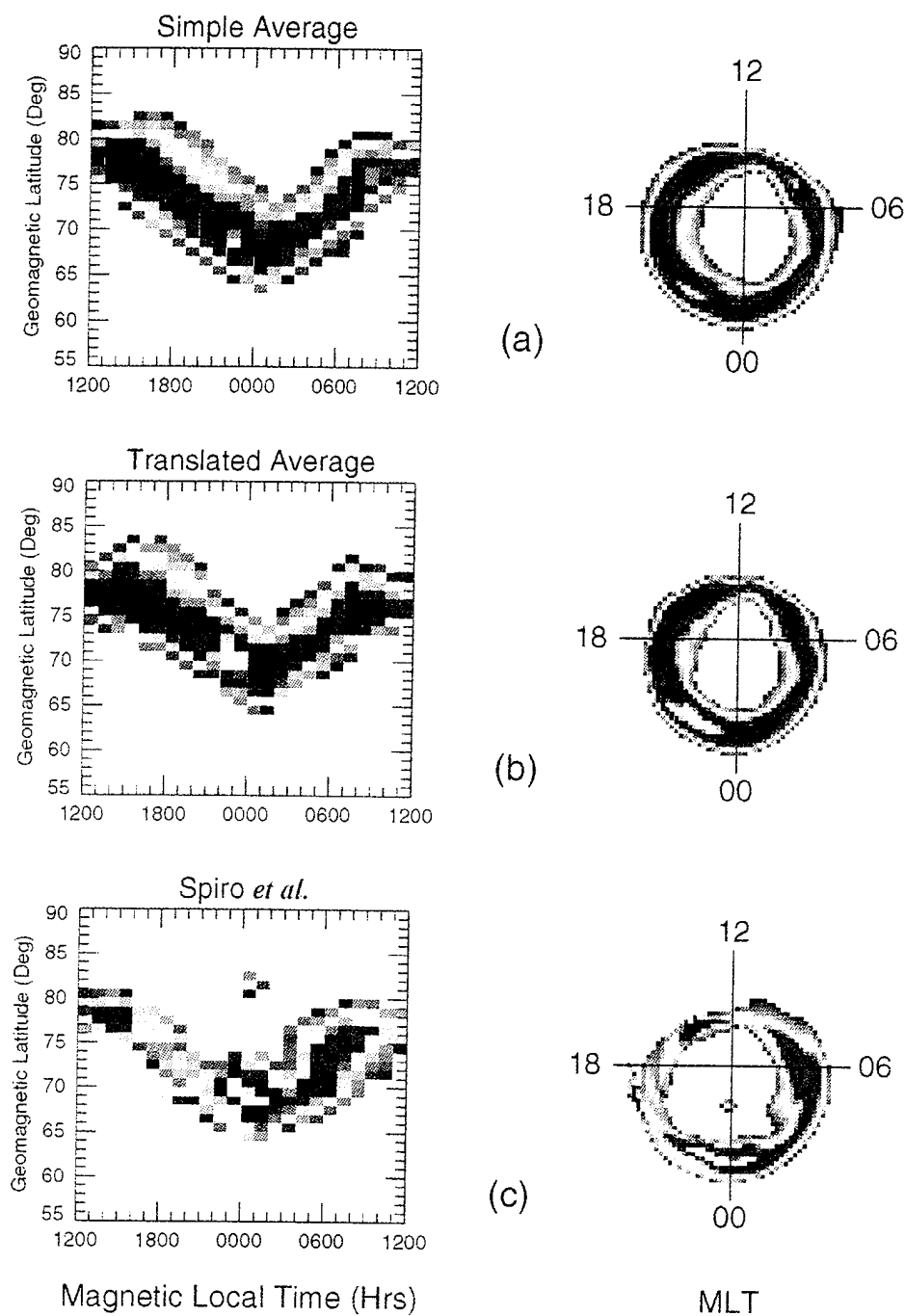
Figure 4.2   Images of the (a) simple average, (b) translated average, and (c) Spiro
et al. data set [1982] for AE ≤ 100 nT. The simple and translated averages are
rebinned into 1 hour MLT by 1° latitude bins for comparison with the particle data.
Mercator projections are on the left and polar projections are on the right.

into 1-hour MLT averages. Figure 4.2c is the calculated photometer response image based on the data set of Spiro *et al.* using the conversion of Figure 4.1. The bin size for the particle data was originally 1 hour in MLT by 2° in geomagnetic latitude, from 50° to 60°, and 80° to 90° GLAT. For the intermediate latitudes from 60° to 80° geomagnetic latitude the bin size was 1 hour in MLT by 1° geomagnetic latitude. To quantitatively compare the particle data with the findings of this research it was necessary to calculate a 1-hour MLT mean of the DE-1 average images. For the high and low latitude regions of the Spiro *et al.* data, where the bin size was 2° latitude, the bin size was reduced to 1° latitude by assigning the odd numbered latitude bins with the mean of the two adjacent even numbered latitude bins.

Comparing the average images and particle data 'image' shown in Figure 4.2 we see that a maximum near midnight is apparent in all three panels. In panel (a) the center of the maximum is located at ~2200 MLT and extends from 2000 to 0200 MLT. In panel (b) it is located at ~2300 MLT, and extends from 1900 to 0200 MLT. In panel (c) the maximum for the particle data 'image' is at ~0000 MLT and extends from 2200 to 0200 MLT.

The maximum in the afternoon sector is not as bright as the maximum near midnight. In the simple average (Figure 4.2a) this maximum is at ~1400 MLT and extends from 1300 to 1700 MLT. The translated average shows this maximum to be at ~1600 MLT and extending from 1300 to 1700 MLT. The particle data shows the maximum at ~1500 MLT and extending from 1400 to 1600 MLT.

In the morning sector the maximum is brightest in the simple average (Figure 4.2a), less bright in the translated average and least bright in the particle data 'image'. The simple average shows the maximum at ~0800 MLT, extending from 0700 to 1100 MLT. The translated average shows it at ~0800 MLT and extending from 0700 to 1000 MLT. The

particle data 'image' shows the maximum at ~0700 MLT and extending from 0500 to 0900 MLT. Note that both dayside maxima are less bright in the Spiro *et al.* image than in either of the two averages. With the exception of the midnight sector, overall the auroral oval is less bright for the Spiro *et al.* data than for the averages.

A different way of summarizing and comparing these images is seen in Figure 4.3, which provides a cross-sectional comparison of the Spiro *et al.* data with the averages found using the DE-1 data set. The dotted line denotes the simple average, and the dashed line the translated average for DE 1 images. While these profiles are similar to the cross sections depicted in Figure 3.9 they are not the same because Figure 3.9 is a cross section at a given hour of MLT while Figure 4.3 is the cross section for the average emission over 1-hour of MLT. The solid line depicts the photometer's expected response (for the 123W filter) as calculated when using Lummerzheim's conversion from characteristic electron energy and electron energy flux to counts per pixel. The horizontal dashed line denotes the ½-count lower limit of the color bar used for the images. The color bar used in this chapter is the same as shown on left hand side of Figure 3.7.

The locations of peak emissions for the three images agree to within a few degrees. The particle data show a much narrower oval and sharper low-latitude boundary in the noon-to-afternoon sectors of the oval. In the morning sector, the low-latitude boundary of the particle data is less sharp than the DE-1 averages. The peaks in the midnight sector are as much as 1.1 counts (~360 R) higher for the particle data than for the imaging averages. This makes the particle-data 'image' about 35% brighter in this sector. These higher peaks can be a result of my more stringent selection criteria in defining quiet magnetic activity. While the particle data yield a greater photometer response near midnight, along most of the oval the responses associated with the particle data are less than those found in the DE-1 averages: In the late evening as much as 1.3 counts (~430
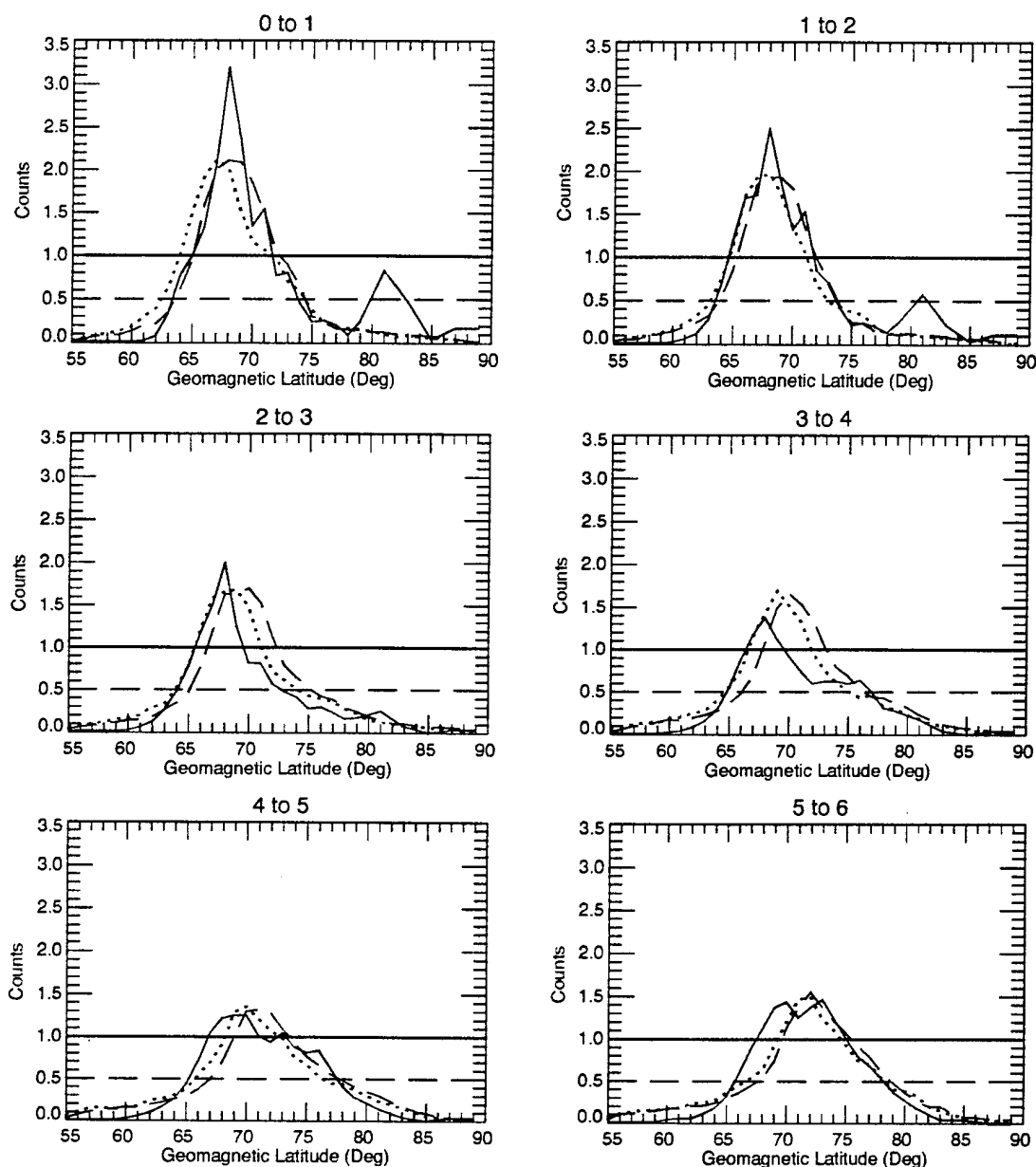
Figure 4.3 Cross sectional representations of the images in Figure 4.2. The dotted line denotes the simple average, the dashed line the translated average, and the solid line Spiro *et al.* data set. The horizontal line depicts the 1/2 count threshold of the color images.

12 to 13

13 to 14

14 to 15

15 to 16

16 to 17

17 to 18

18 to 19

19 to 20

20 to 21

21 to 22

22 to 23

23 to 24
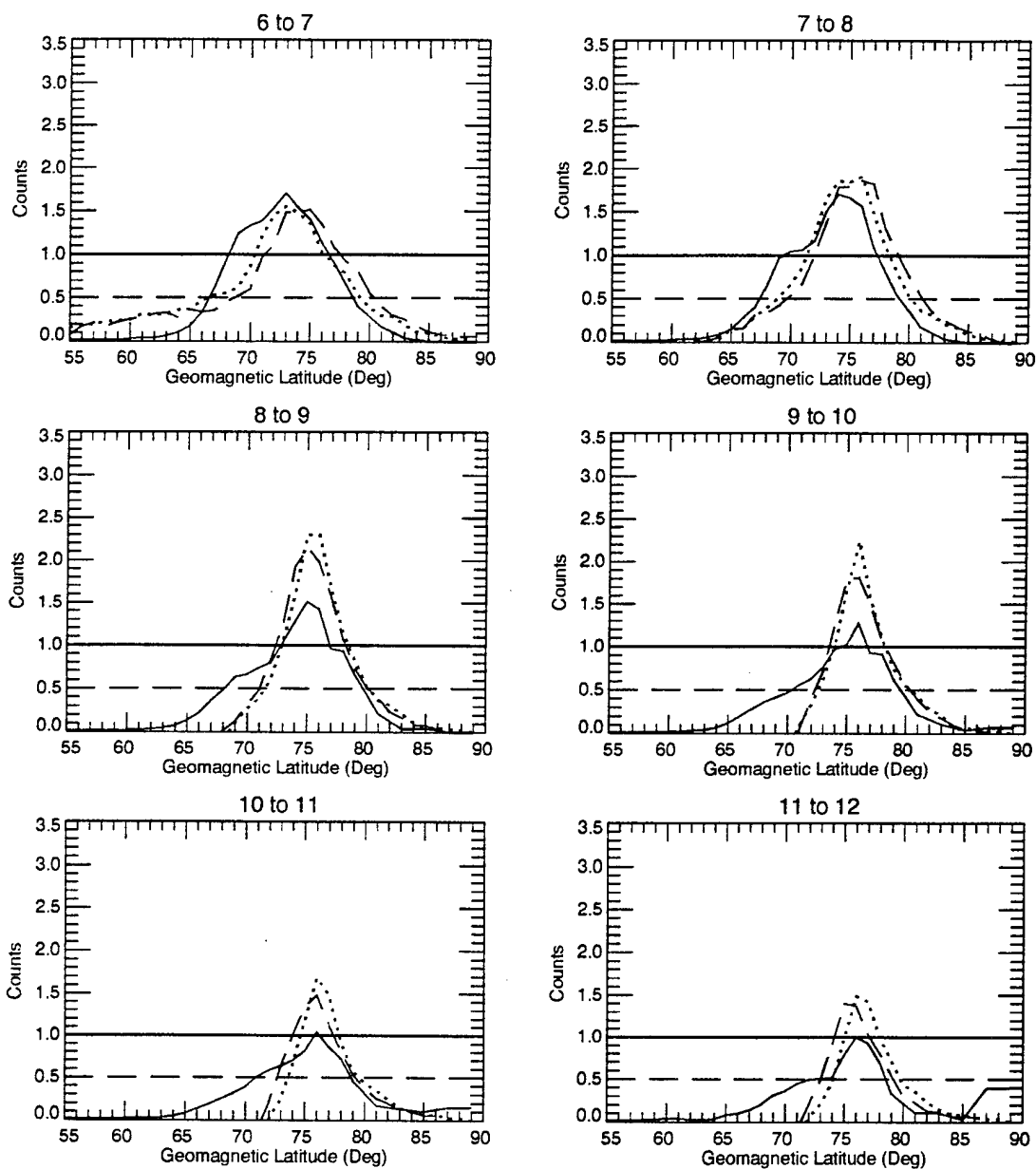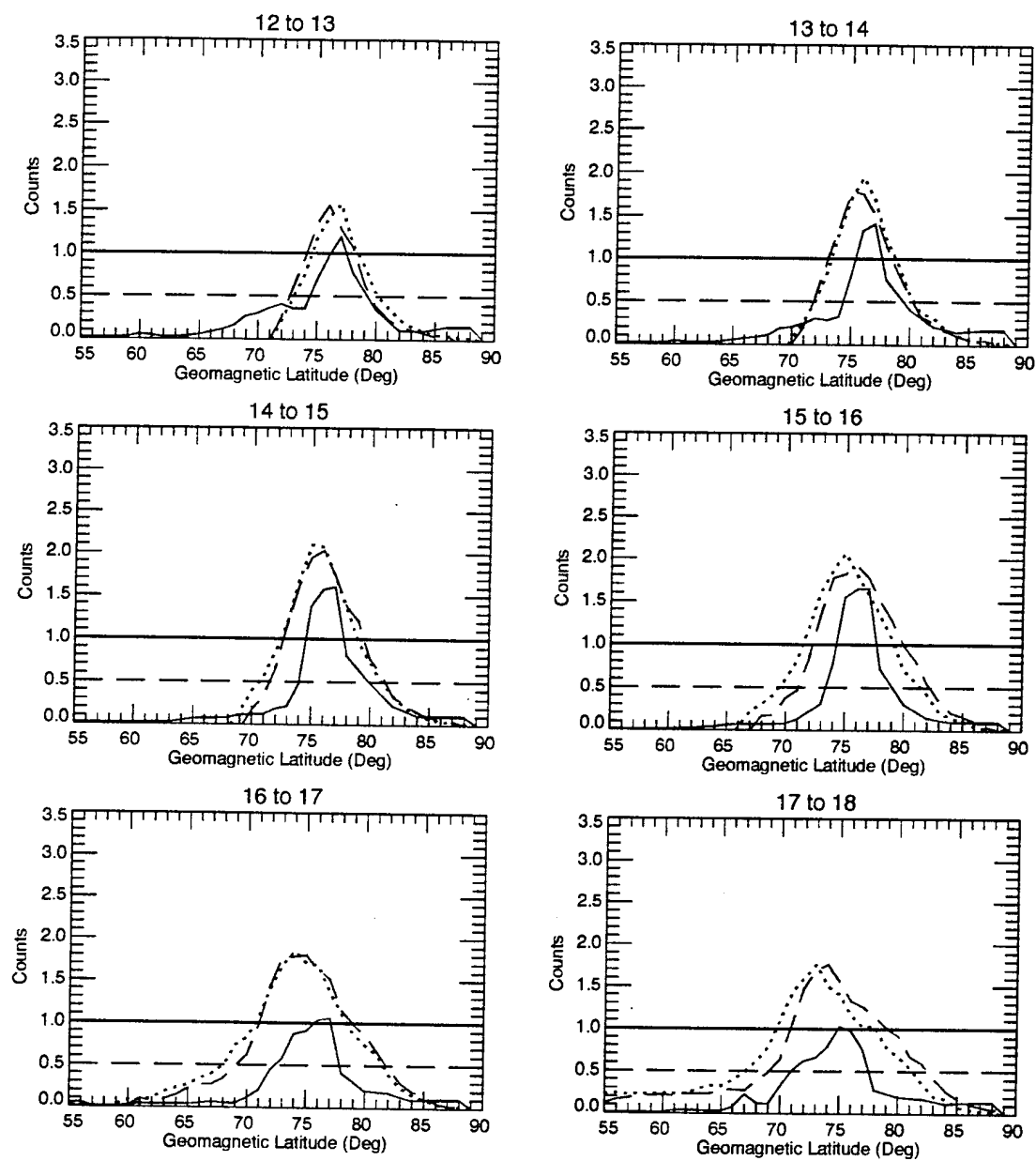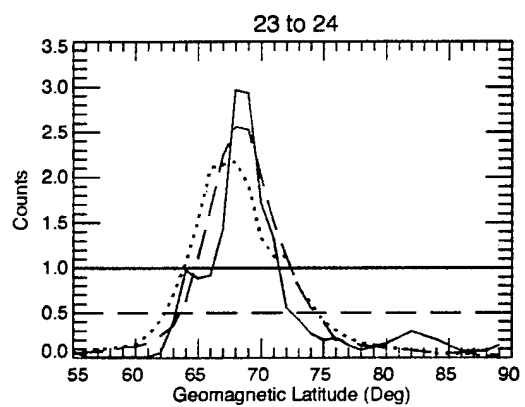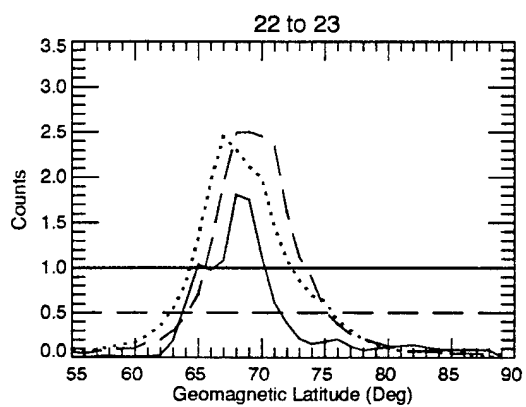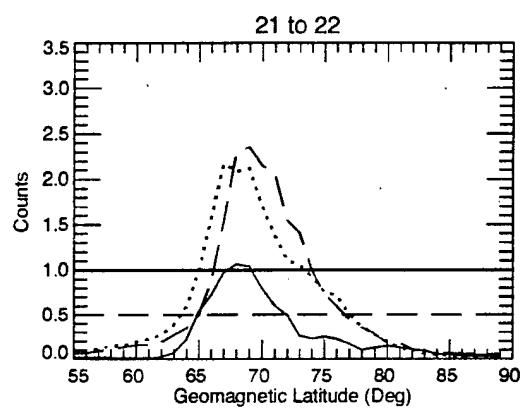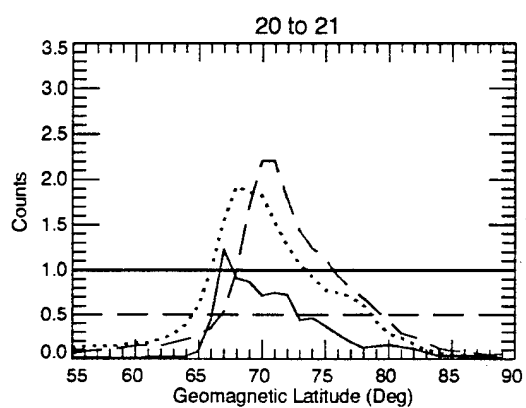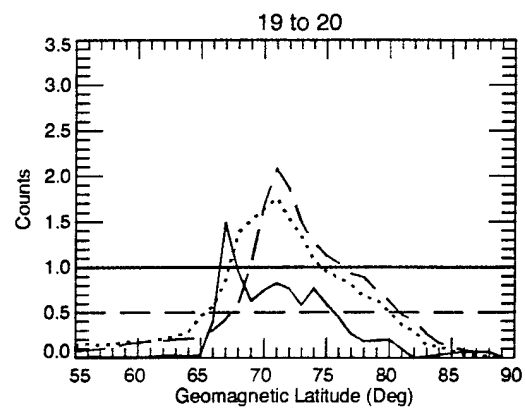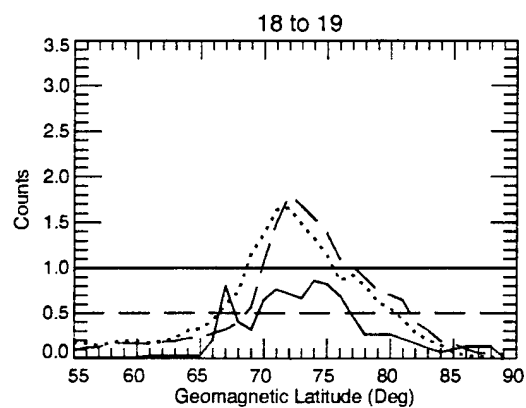
R) alone in finding the Spiro *et al.* data set to have lower values. Hardy *et al.* [1985] showed that their measurements were, on average, within 20% of the Spiro *et al.* [1982] values, but were uniformly higher than those of Spiro *et al.* Hardy *et al.* [1985] pointed out that the two data sets were from two different solar cycles: 1974-76 for Spiro *et al.* [1982] and 1977-79 for Hardy *et al.* [1985]. Even with the extremes described earlier the DE-1 averages emissions are ~15% higher than in the particle-data 'image' inside the auroral oval. Summing over all latitudes and MLT, there are 17% more total counts in the particle-data 'image', 286 counts, than in either of the averages, 235 counts.

From these cross sectional plots of the images depicted in Figure 4.3, the ½-count low-latitude boundary (LLB) and high-latitude boundary (HLB) are extracted for these averages, to the nearest degree. Figure 4.4 shows a polar plot of the LLB depicted in a format similar to those in Figure 3.3. The solid line denotes the Spiro *et al.* boundary as calculated by this research, the dotted line the simple average, and the dashed line the translated average. Also plotted here for comparison is the Q=3 LLB of Holzworth and Meng [1975], denoted by the dash-dot-dot-dot line. Some of the roughness of this plot is due to the large bin sizes used for this comparison. The Holzworth and Meng LLB is generally located at higher latitudes than all the other boundaries, except in the afternoon sector, where the Spiro *et al.* boundary occurs at higher latitudes. The largest differences between any of the boundaries occur in this sector, reaching 4° between the Spiro *et al.* boundary and both the simple and translated averages.

Some of the differences between the averages and the particle data in the afternoon sector may be an artifact of the data selection. As stated in Chapter 3, images were selected to diminish as much as possible the effect of dayglow intrusion into the auroral oval. This restricted the data set available to the northern hemisphere winter. No such

Low Latitude Boundary
(1/2 count)
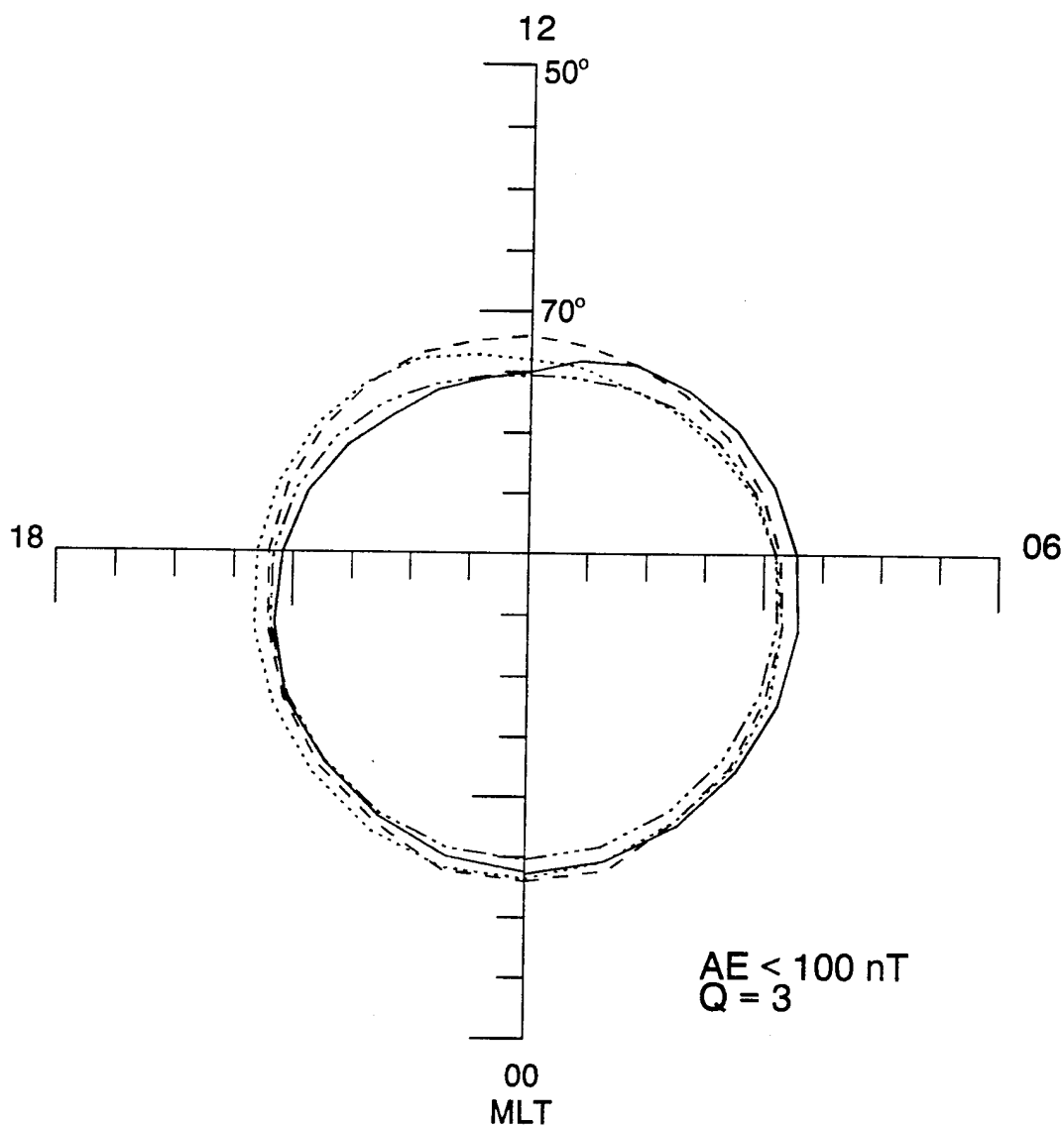
Figure 4.4   Polar projection of the low-latitude boundary for a 1/2-count threshold as seen in Figure 4.3 and the Holzworth and Meng [1975] Q=3 LLB. The solid line denotes the Spiro *et al.* boundary, the dashed line the translated average, the dotted the simple average, and the dash-dot-dot-dot line represents the Q=3 boundary.

distinction was made by Spiro *et al.* [1982], and this may have led to some seasonal variations being washed out.

Figure 4.5 shows a polar plot of the high-latitude boundary at the same ½-count level used in Figure 4.4. This plot uses the same format as Figure 4.4 and includes the HLB of Holzworth and Meng [1975] for Q=3. The solid line depicts the Spiro *et al.* HLB calculated by this research, the dotted line the simple average, the dashed line the translated average, and the dash-dot-dot-dot line the Q=3 high-latitude boundary.

The Q=3 high-latitude boundary is found at much lower latitudes than any of the other boundaries. There is as much as a 7° difference in the afternoon sector between it and the DE-1 averages. The particle data boundary is also generally found at lower latitudes than the averages, the largest difference being 4° in the evening sector.

Figures 4.6 and 4.7 show plots similar to those in Figures 4.4 and 4.5, but the threshold used is 1 count/pixel. Comparison of Figure 4.4 with Figure 4.6 shows little difference in the location of the low-latitude boundary. This is not unexpected, since there is a large gradient in auroral brightness along the low-latitude edge of the oval. The high-latitude boundaries for the ½- and 1-count/pixel thresholds in Figures 4.5 and 4.7, respectively, do show significant differences.

The 1-count/pixel threshold for the high-latitude boundary of the auroral oval more closely matches the Q=3 HLB of Holzworth and Meng [1975]. In the midnight sector the two averages, the particle-data 'image' and the Q=3 boundary, are coincident to within ±1° of latitude. The largest differences for all the high-latitude boundaries are still in the afternoon sector. The particle-data 'image' is nonexistent in the afternoon sector because the particle-data 'image' counts/pixel were less than the threshold of 1 count/pixel.

Spiro *et al.* made no distinction in their study between variations due to hemisphere (north or south), season, longitude, or solar cycle changes. The DE-1 data set used in this

High Latitude Boundary
(1/2 count)
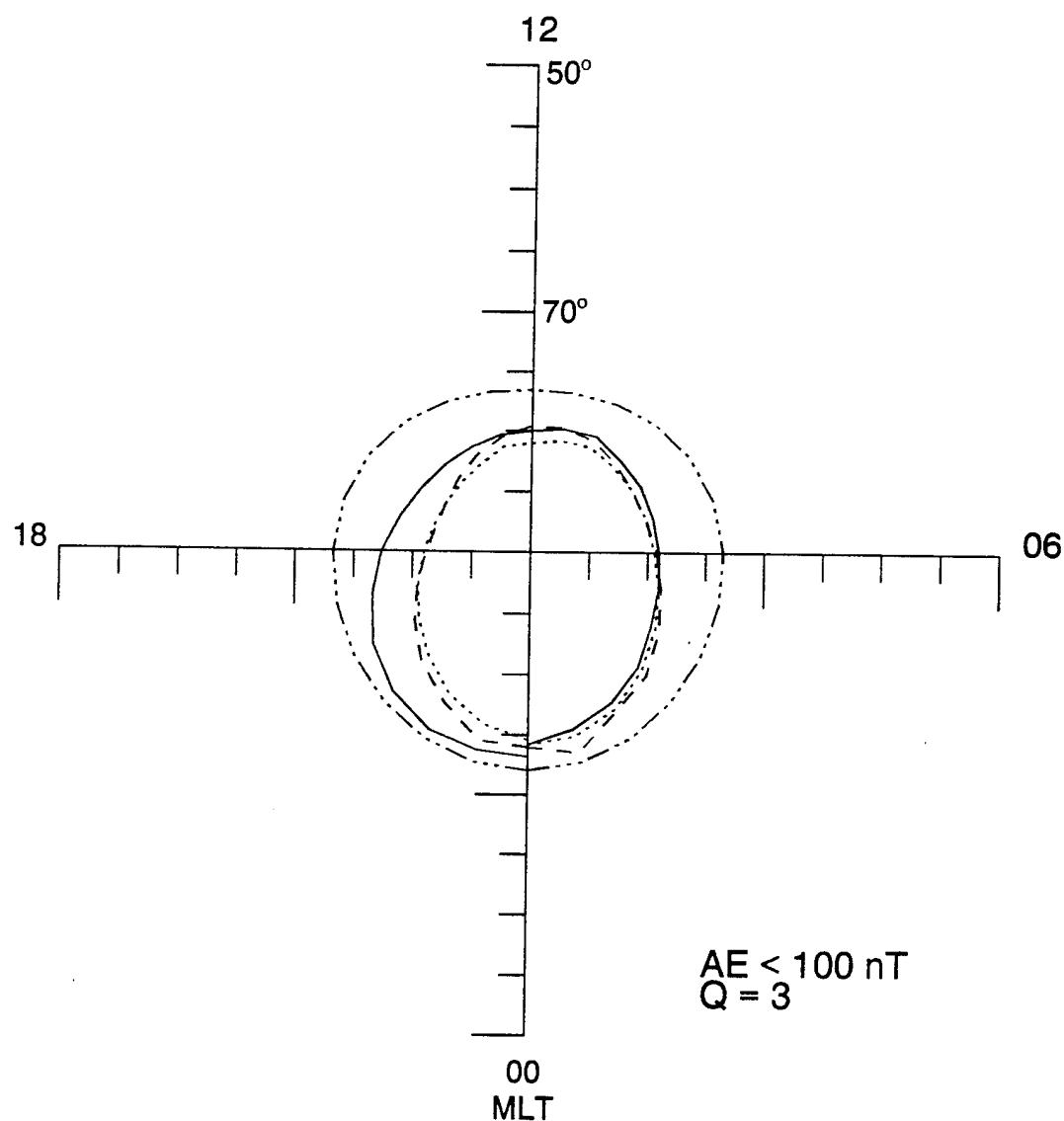
Figure 4.5   Polar projection of the high-latitude boundary for a 1/2-count threshold as seen in Figure 4.3 and the Holzworth and Meng [1975] Q=3 HLB. The solid line denotes the Spiro *et al.* boundary, the dashed line the translated average, the dotted the simple average, and the dash-dot-dot-dot line represents the Q=3 boundary.

Low Latitude Boundary
(1 count)
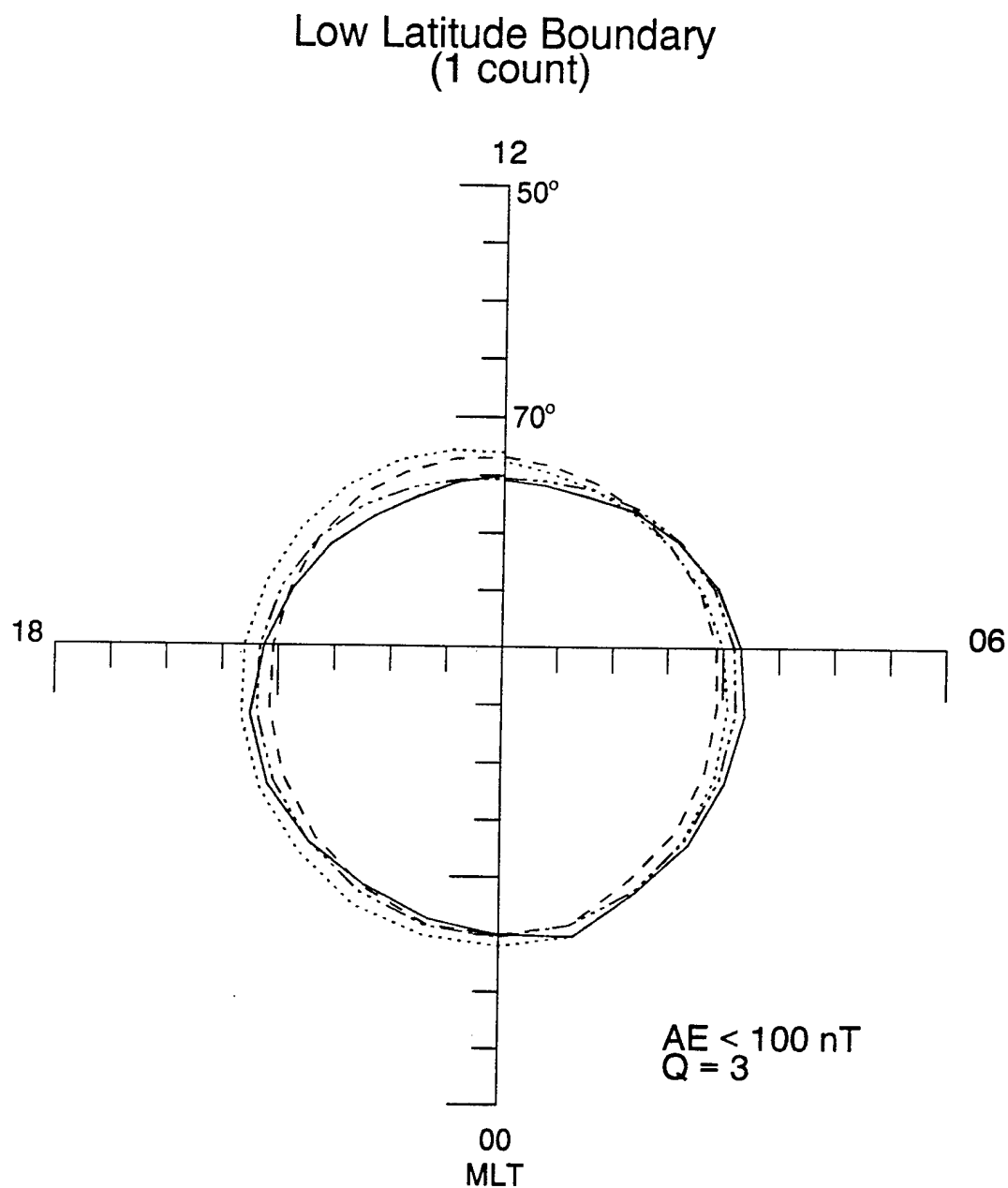
Figure 4.6   Polar projection of the low-latitude boundary for a 1-count threshold as seen in Figure 4.3 and the Holzworth and Meng [1975] Q=3 LLB. The solid line denotes the Spiro *et al.* boundary, the dashed line the translated average, the dotted the simple average, and the dash-dot-dot-dot line represents the Q=3 boundary.

High Latitude Boundary
(1 count)
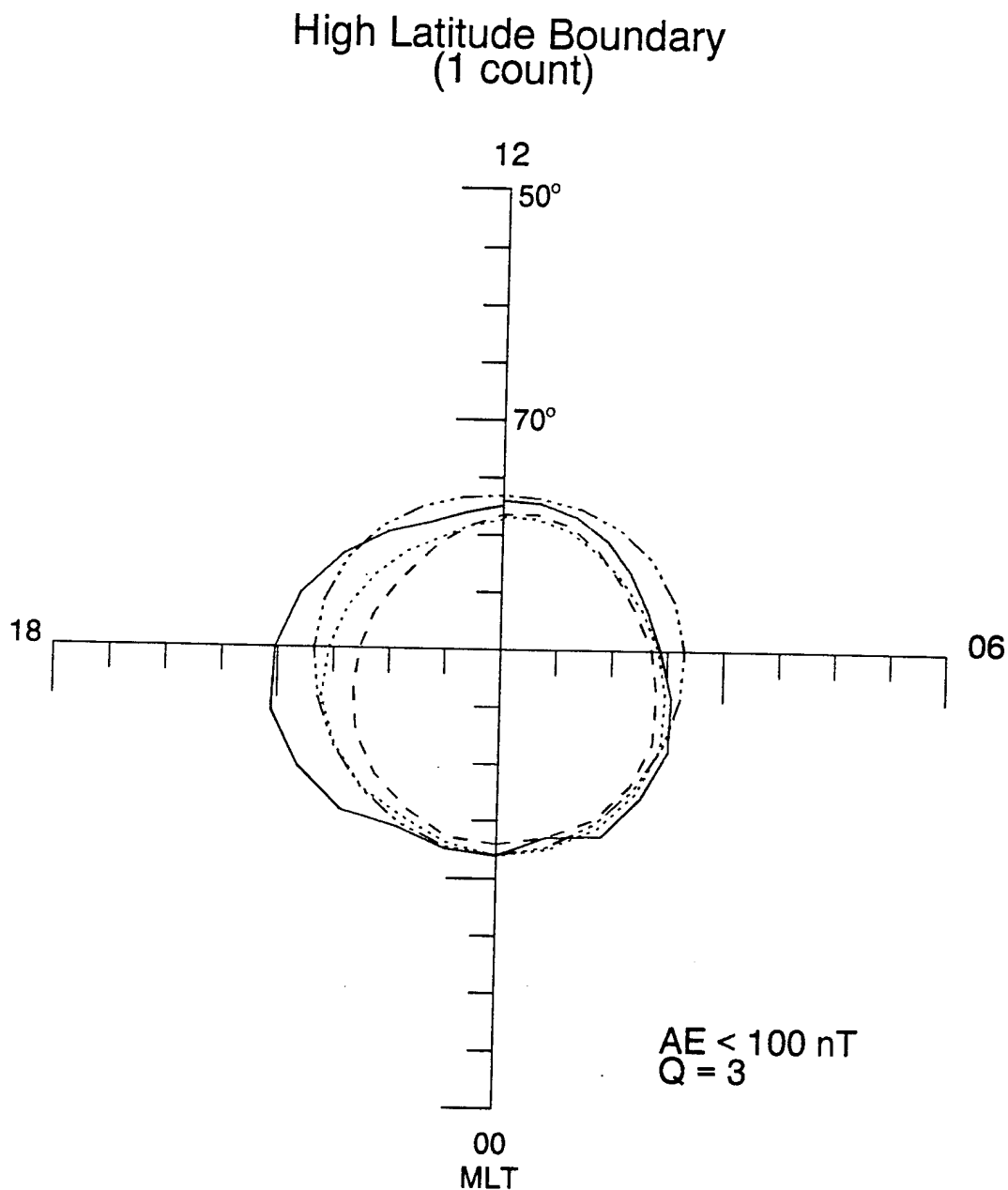
Figure 4.7   Polar projection of the high-latitude boundary for a 1-count threshold as seen in Figure 4.3 and the Holzworth and Meng [1975] Q=3 HLB. The solid line denotes the Spiro *et al.* boundary, the dashed line the translated average, the dotted the simple average, and the dash-dot-dot-dot line represents the Q=3 boundary.

research was restricted to the northern hemisphere winter, and took into account small variations in the oval that may have indicated increased auroral activity. Such differences in the parameters during data selection may explain the differences in the 'images'. More important though is that given these differences in data selection, the global pattern of the electron precipitation is the same. A comparison of the effects of changing IMF component orientation is not possible with the Spiro *et al.* data set.

CHAPTER 5

DISCUSSION AND CONCLUSIONS

Discussion

The nearly instantaneous pattern of auroral electron precipitation for magnetically quiet periods has been investigated by using the emission patterns detected by the Dynamics Explorer 1 Spin-Scan Auroral Imaging photometer in the far-ultraviolet (FUV) region of the spectrum. From the DE-1 data set between September 26, 1981 to February 28, 1982, 85 quiet-time images in 13 separate imaging sequences were selected to create a mean auroral oval for AE < 100 nT. This mean auroral image showed a general precipitation pattern that can be seen in part, or in whole, in each of the individual images.

The initial investigation looked at the changing dimensions of the auroral oval after the AE index decreased and remained below a given threshold during the imaging sequence. The purpose was to establish a reference oval coordinate system to which other auroral distributions may be translated. The low-latitude boundary of the oval was used as a first measure of the auroral angular spatial extent because it is the most constant and distinct feature of an auroral oval. An initial estimate of the low-latitude boundary (LLB) was made visually using the XSAI computer program. From these visually estimated boundaries the total area encompassed by the oval was plotted against the time since AE decreased below threshold values of 50 and 100 nT. Initial inspection of these plots shows the area of the oval to be decreasing approximately linearly with time. On the basis

of this approximately linear relationship, the co-latitudes of equivalent circles were calculated from the areas and quadratic fits were used in an attempt to extrapolate a minimum auroral oval size for long periods of magnetic quiescence. As a comparison to the quadratic fits, linear fits were also obtained for the same data. For the plots of radius versus the time duration after AE passed below 100 nT, there was no important difference between the linear and quadratic fits, within one sigma. In the case of the radius plotted against the time duration after AE went below 50 nT, the linear fit was better than the quadratic fit. For this 50-nT plot the linear fit made more sense physically since the quadratic fit shows the auroral oval reaching a minimum co-latitude of ~18° then expanding again after 7 hours of no magnetic activity. The mean linear relationship for the data is given by,

$$R = 0.16°/hr \cdot \Delta t + 69.1°$$

where R is the latitude of the equatorward boundary and Δt, in hours, is the time since AE passed below 100 nT.

From this initial investigation of the auroral oval low-latitude boundary it was determined that the mean auroral oval was nearly a circle in geomagnetic coordinates, with its center offset from the geomagnetic pole ~4° towards the midnight sector and ~1° towards the evening sector. A comparison of this mean low-latitude boundary with similar work done by Holzworth and Meng [1975] for Q=2 and Q=3 shows the boundaries found by independent data sets and analysis methods to be nearly equivalent. The Holzworth and Meng equation for the low-latitude boundary is within the limits of

error of the estimations of the oval found here. The Holzworth and Meng LLB is calculated from

$$\Theta = A_1 + A_2 \cos(\varphi + A_3) + A_4 \cos(2\varphi + 2A_5) + A_6 \cos(3\varphi + 3A_7)$$

Where Θ is the corrected geomagnetic colatitude, φ is the angular value for the magnetic local time, and the coefficients A_i are given for each value of Q. A possible dependence of the location of the center of the oval on various measured geomagnetic parameters was investigated but none was found, possibly due to the small size of the data set used.

When overlaying these initial estimates of the low-latitude boundary on images that had been converted to arrays compatible with IDL it was found that there was an error of $\pm 3°$ in the location of the estimated boundaries. The error was not systematic in the sense that the boundaries were not consistently low or high. These errors arise from the difficulty of estimating the location of the low-latitude boundary visually. The LLB of the auroral oval has a steep emissions gradient. Although a sharp gradient defines the LLB well, visual estimation of the boundary is limited by the graphics software and hardware used. Even with the best resolution hardware, the software is limited to a finite number of points to define a line thus the placement may be off by a pixel or two (on the order of $1°\text{-}2°$) but appear to be at the correct location. An additional error on the order of a degree may arise from the fitting of the points placed at the LLB by the computer program. XSAI does a cubic-spline fit to the points marking the low-latitude edge of the oval. Such a fit smoothes over the 'rough' edges of the oval. Even with such errors the visually estimated low-latitude boundary is a good first-order approximation and compares favorably with findings of similar research.

After the initial investigation of the auroral oval dimensions, the images were averaged using several different techniques. The averaging was done to get a mean quiet-time auroral oval for AE < 100 nT. A simple average was done with no weighting or altering of the images as a baseline for comparison to the results of the other averaging techniques investigated, and because it is the type of averaging that has been used extensively in similar work. Other methods of averaging were investigated in an attempt to limit the amount of 'washing out' or blurring of auroral oval feature and boundaries and to compensate for decreasing auroral oval size after AE went below 100 nT. Of the several methods looked at, a translated average was deemed the more efficient and easiest technique to achieve the desired results.

The translated average used the mean visually estimated low-latitude boundary as the average dimension of the auroral oval. Each image low-latitude boundary was compared to this mean. The difference between the mean boundary and the individual image boundary at each local time defined a parameter that was used to translate sections of each image, toward or away from the pole, to overlay its low-latitude edge with the mean auroral oval. While this technique did sharpen the low-latitude edge of the mean oval image, differences between the simple average and the translated average proved to be negligible.

From the mean auroral image for AE < 100 nT one is able to discern relative maxima in the emission patterns at approximately 0800, 1430, and 2200 magnetic local time. In general the auroral oval emissions are low for the quiet-time images, ranging from ~½ to ~1.2 counts/pixel (~150-360 R), with a mean auroral emission of ~1 count/pixel. The maxima in the morning and afternoon sectors have emissions ~2.0 times greater then the mean auroral oval emissions. The maximum in the midnight sector may be as much as 2.5 times the mean emissions.

These maxima were investigated for a dependence on the orientation of the interplanetary magnetic field (IMF). The 13 imaging sequences were divided into four subsets corresponding to the orientation of the IMF B_x and B_y components. To eliminate possible influence from the IMF B_z component only those images where $B_z > 0$ nT were used. A comparison of the four average images, corresponding to the four quadrants of the IMF B_{xy} plane, showed the emission patterns to have a strong dependence on the B_x component.

When B_x is positive (sunward) the maxima in the morning and afternoon sectors are only 10-15% greater than the surrounding emissions. There is a marked increase in the brightness of the auroral oval emissions when B_x is negative. When $B_y > 0$ nT a comparison of quadrant 1 ($B_x > 0$ nT) and quadrant 2 ($B_x < 0$ nT) shows the two dayside maxima tripling in counts/pixel over the surrounding emissions.

When B_y is negative, a comparison of $B_x < 0$ nT to $B_x > 0$ nT (quadrant 3 to quadrant 4) shows an increase of ~45% in the maximum brightness in the afternoon sector and ~220% in the morning sector. Such dramatic changes in the precipitation pattern emissions are not exhibited when one compares changes in the B_y component with cases where the sign of the B_x component is the same (i.e., quadrant 1 to quadrant 4, quadrant 2 to quadrant 3).

The dependence of the auroral precipitation patterns on IMF orientation has been investigated by other researchers, directly and indirectly. Research done by Iijima and Potemra [1982] investigated the relationship between the IMF B_z and B_y components and the field aligned current densities, an indirect measure of the precipitation pattern. They concluded that there was a very poor correlation between the field aligned current density patterns and B_y when B_z was positive. From the data presented by this research one may reach a similar conclusion. Here a stronger overall dependence on the IMF B_x

component is shown, while a change in the sign of B_y has less impact on the precipitation pattern.

In earlier work Iijima and Potemra [1978] looked at the field aligned current density patterns for various stages of auroral substorm activity. They established a quiet-time current density profile showing two peaks, one in the morning sector and one in the afternoon sector. The peaks were for region 1 currents, or currents away from the ionosphere in the afternoon sector (i.e., downward moving electrons) and currents into the ionosphere in the morning sector. Their peaks were located at ~0900 and ~1300 MLT, at ~75° and ~77° latitude, respectively. The mean images produced in this study show peak emissions located at 0800-0900 MLT at 75°, and 1400-1500 MLT at 76°. These locations of the relative maxima compare favorably with the peaks in the field-aligned currents noted by Iijima and Potemra [1978].

The case study of December 3, 1981, where the IMF components change sign during the imaging sequence is a good example of how the precipitation patterns change with variations in IMF orientation. The changes in the B_x and B_y components correlated directly to rapid responses in the auroral precipitation patterns. These changes were as short lived as the changes in the IMF components. The changes in the precipitation patterns when the IMF B_z became negative for a short period appear to be longer lasting. The change in B_z also cause larger scale changes in the precipitation pattern of the oval. The source of precipitating particles associated with changes in B_z and subsequent substorm activity is from nightside regions of the magnetosphere. Dayside phenomena are not directly connected to these regions, so a different source must be looked for, such as the boundary plasma sheet.

Newell and Meng [1992] mapped to the boundary plasma sheet the regions of relative maxima in the dayside auroral oval si,ilar to those found here. The changes in the

B_x and B_y components may be the 'triggers' that enable particles from such a region of the magnetosphere to precipitate into the ionosphere. Researchers looking at the IMF component dependence for polar rain [Makita and Meng, 1987; Meng and Kroehl, 1977] find that there is an increase in the polar rain flux in the northern hemisphere for negative B_x (or positive B_y). Although, the maxima found here are not polar rain phenomena, a similar relation to IMF orientation appears to exist.

Comparison of the emission patterns found during this research was extended to similar research for precipitating electrons, as summarized in the works of Spiro *et al.* [1982] and Hardy *et al.* [1985]. An equation relating the count rate as seen at the spacecraft to the characteristic energy per unit energy flux was derived from the mean of a data set provided by Lummerzheim [1994]. This equation was used to convert the data set of characteristic energy and energy flux given by Spiro *et al.* [1982] for AE < 100 nT to a count rate that could be compared to the mean image established by this research.

The calculation using the data set from Spiro *et al.* [1982] resulted in an 'image' that, though somewhat narrower in the oval's latitudinal width, depicted the same relative maxima as the mean image determined by this research. The difference in latitudinal width of the oval is possibly the result of the difference in the type of data used to create the images. The particle detectors sampled only when the instrument was oriented towards the magnetic zenith, looking into the loss cone, and therefore measured only the downward moving particles [Spiro *et al.*, 1982]. The 'image' created from their data set is associated only with the precipitating particles are impacting the upper atmosphere, and not with the additional complications of emission and transport of light through the upper atmosphere. The DE-1 images are of the photons being emitted from the atmosphere in the presence of numerous collisions and scattering. This scattering broadens the emission

region detected by a photometer above the emitting region by as much as 1° or 2° in latitude.

This comparison of a particle data 'image' to the mean images found by this research verified that the emission patterns created from the photometric data directly correspond to global-scale precipitation patterns found by other researchers. The data sets for precipitating electrons used by Spiro *et al.* were not correlated to components of the IMF. For this reason a comparison of the Spiro *et al.* patterns' dependence on the IMF components was not accomplished. But the comparison showed that the relationship determined by Lummerzheim [1994] is valid.

From the mean images used for the particle data a comparison of the low-latitude and high-latitude boundaries was done. This second investigation of the auroral oval boundaries was done with more exacting thresholds for the 'edges' of the oval. Initially, the boundaries were calculated for a ½-count/pixel threshold and compared with the Holzworth and Meng [1975] Q=3 quiet-time oval. The low-latitude boundaries for the DE-1 averages and the particle data 'image' varied within 5° of latitude of the Q=3 oval. The high-latitude boundaries (HLB) differed by as much as 9°. The differences between the Q=3 boundaries and those of the images may be the result of how the boundaries were established by Holzworth and Meng, similar to the visual estimation problems outlined earlier.

For images obtained in magnetically quiet periods, the high-latitude 'edge' of the auroral oval may be very difficult to discern visually. Holzworth and Meng [1975] visually estimated their boundaries from DMSP images. The ½-count/pixel threshold borders on the minimum discernible signal for the eye in the DMSP images without the aid of false color imaging and selectable color bars. For this reason a second comparison of the oval boundaries was made using a threshold of 1-count/pixel. The low-latitude

boundaries moved to within 2° of the Q=3 LLB. The high-latitude boundary of the averaged image oval moved to within 5° of the Q=3 HLB at its worst in the afternoon sector, and within 3° for the rest of the oval. The exceptions to this are seen in a good part of the afternoon and evening sectors where the particle data 'image' values remained at less than 1-count/pixel.

Conclusions

This research is an initial investigation of the magnetically quiet global auroral precipitation patterns. It is a small part of a much larger project to create quantitative models of auroral electron precipitation patterns on a global scale for use with general circulation models of the coupled thermosphere and ionosphere. While the DE-1 far-ultraviolet images alone cannot provide these models they do provide a global scale pattern of the precipitation that is a necessary input to such electron energy precipitation models.

Established here are a set of mean global-scale auroral images for AE < 100 nT that can be used as inputs into the new global-scale auroral electron precipitation model for magnetically quiet periods. These images provide the mean auroral oval dimensions as a rough circle with its center offset from the geomagnetic pole. They also provide a view of the changes that take place in the precipitation pattern when the IMF B_x and B_y components change sign. Appendix B contains tables of the mean counts/pixel in 1° x 1 hour magnetic local time bins for the simple average image and the four IMF B_{xy} quadrant average images established by this work.

From the comparison of the two averages (simple and translated) presented here one can conclude that for the quiet-time images no significant improvement can be made over

a simple average. Although this result is unexpected, it is not unrealistic. For many quiet-time images there is little or no discernible structure other than the oval itself. Even the boundaries of the auroral oval are less distinct in the quiet-time images than in more active periods. The poleward boundary of the oval becomes very diffuse in images where the magnetic activity has been quiet for periods of more than four hours. The equatorward edge, although sharper then the poleward, can also become diffuse for periods of magnetic quiescence greater than 7-8 hours in duration.

The research done here has confirmed work done earlier by other researchers through an independent method and data set. The auroral oval dimensions for the low-latitude boundary laid out by this research confirm that the equations established by Holzworth and Meng [1975] are valid for the quiet time auroral oval. The comparison of the emission patterns with an 'image' from particle data given by Spiro *et al.* [1982] shows that their tables for characteristic electron energy and energy flux are still good approximations, although one may want to scale their afternoon emissions to higher values. Also provided here are methods and techniques that may be used in future work with DE-1 images and comparison with other studies done on the precipitating electron patterns.

Suggestions for Future Research

The experience and knowledge gained from this research is a valuable stepping stone towards global-scale models of the auroral electron precipitation patterns. The data set used here was confined to a narrow period of the northern hemisphere winter of 1981-82. Future work should include a comparison of southern hemisphere data set, with emphasis on the IMF B_x and B_y component dependence. One would expect a mirror image of the results shown here for such a dependence. This should be confirmed.

The mean auroral oval emission patterns established by this research should be compared with other DE-1 images that were acquired with different filters for the same conditions defined here. Such a comparison may lead to relationships similar to those established by Rees and Luckey [1974] using ratios of emissions to find the characteristic electron energies and energy fluxes.

The methods for averaging and presentation of mean auroral patterns should be used for more active auroral conditions. Mean emission patterns for substorm phases could be established with such methods. The orientation of the IMF and its influence on the precipitation patterns should be looked at during all phases of this research.

APPENDIX A

IMAGE			IMF			AREA	AE
yr	day	time	Bx	By	Bz	10^7 km^2	nT
81	304	0729:16	0.5	-5.5	3.2	1.84	45
		0753:32				1.79	40
		0806:23	2.1	-4.5	3.0	1.93	40
		0817:43				1.91	40
		0829:51				1.90	40
		0841:59				1.98	40
		0854:26				1.95	40
		0906:16	4.5	-4.3	1.6	1.86	40
81	305	0517:40	2.8	3.1	1.5	2.11	30
		0529:48				2.16	50
		0541:56				2.17	30
		0554:04				2.03	20
		0606:13	-4.3	-0.2	5.3	2.03	30
		0618:21				1.92	30
81	313	0431:32	3.5	-0.1	3.6	2.21	25
		0443:40				2.18	50
		0507:57	4.6	-1.2	2.3	2.08	20
		0520:05				2.22	35
		0532:13				2.02	40
		0544:22				2.02	30
81	317	1011:10	7.8	0.8	2.8	1.62	50
		1023:18				1.66	40
		1035:25				1.72	40
		1047:34				1.65	40
		1059:42				1.83	55
		1111:51	7.2	1.0	3.7	1.86	70
		1123:59				1.77	60
		1136:08				1.87	50
81	330	2102:44	3.4	-3.2	1.8	1.94	50
		2114:53				2.08	40
		2127:02				2.08	50
		2139:11				2.03	60
		2151:19				2.09	60
		2203:29	4.2	-1.6	2.3	2.07	70
		2215:38				2.00	60
		2227:46				2.06	70
		2239:55				1.90	50
81	336	0731:49	m	m	m	1.94	30
		0743:58				1.93	35
		0756:06				1.86	40
		0808:15	2.5	5.3	6.6	1.82	50
81	337	0343:40	4.0	-2.7	8.9	1.77	40
		0355:49				1.86	45
		0407:58	1.4	5.8	7.1	1.74	40

Table A.1 List of images used to determine the mean image and several parameters used in selection of these images.

103

IMAGE			IMF			AREA	AE
yr	day	time	Bx	By	Bz	10^7 km^2	nT
		0420:06				1.86	40
		0432:15				1.80	45
		0444:24				1.49	50
		0456:33				1.84	45
		0508:42	-0.6	0.7	1.0	1.76	50
81	345	1002:56	-0.6	-3.6	4.3	1.68	50
		1014:59				1.70	60
		1027:08				1.74	55
		1039:17				1.73	60
		1051:26				1.77	70
		1103:32	-1.2	-4.7	2.2	1.68	80
	·	1115:43				1.80	60
		1140:01				1.70	40
81	351	0320:05	0.3	-2.0	-0.1	1.48	30
		0332:14				1.49	30
		0344:23				1.62	30
		0356:32				1.58	30
		0408:41	0.3	-1.1	1.0	1.65	30
		0421:26				1.42	30
		0432:59				1.41	30
		0445:08				1.58	30
81	351	0927:41	-2.0	-0.5	1.3	1.71	30
		0939:50				1.67	35
		0951:59				1.62	30
		1004:08	-2.1	-0.8	1.2	1.58	35
		1016:17				1.63	40
		1028:26				1.59	40
82	013	0531:03	2.1	-4.6	-0.2	1.70	30
		0543:12				1.57	25
		0555:21				1.67	25
82	014	0231:02	3.8	-1.8	4.9	1.55	5
		0243:12				1.57	10
		0255:21				1.51	20
		0307:30	4.1	-0.7	4.1	1.42	10
		0319:39				1.44	20
		0331:49				1.46	15
82	019	0604:12	0.6	2.3	1.7	1.97	30
		0616:22				2.11	35
		0628:32				1.90	40
		0640:41				2.04	35
		0652:50				2.02	40
		0705:00	0.7	0.8	1.7	1.89	40

Lat	12	13	14	15	16	17	18	19	20	21	22	23	00	01	02	03	04	05	06	07	08	09	10	11
90	0.0	0.0	0.0	0.0	0.0	0.0	0.0	0.1	0.0	0.0	0.0	0.0	0.0	0.0	0.1	0.0	0.0	0.0	0.1	0.0	0.0	0.0	0.0	0.0
89	0.0	0.0	0.0	0.0	0.0	0.0	0.0	0.1	0.1	0.1	0.0	0.0	0.0	0.0	0.1	0.0	0.0	0.1	0.1	0.0	0.0	0.0	0.0	0.0
88	0.0	0.1	0.1	0.1	0.1	0.1	0.1	0.1	0.1	0.1	0.1	0.1	0.1	0.1	0.1	0.1	0.1	0.1	0.1	0.1	0.1	0.1	0.1	0.1
87	0.1	0.1	0.1	0.2	0.2	0.1	0.1	0.1	0.1	0.1	0.0	0.1	0.1	0.1	0.1	0.1	0.1	0.1	0.1	0.1	0.1	0.1	0.1	0.1
86	0.1	0.1	0.2	0.3	0.3	0.2	0.2	0.2	0.2	0.1	0.1	0.1	0.1	0.1	0.1	0.1	0.2	0.2	0.2	0.2	0.2	0.1	0.1	0.1
85	0.1	0.2	0.3	0.5	0.5	0.3	0.2	0.4	0.2	0.2	0.1	0.0	0.1	0.1	0.1	0.2	0.3	0.3	0.3	0.3	0.2	0.3	0.2	0.1
84	0.2	0.3	0.6	0.8	0.7	0.4	0.4	0.5	0.3	0.3	0.1	0.1	0.1	0.1	0.2	0.2	0.3	0.4	0.4	0.5	0.4	0.4	0.3	0.2
83	0.2	0.6	0.8	1.3	1.0	0.6	0.6	0.6	0.4	0.4	0.1	0.1	0.1	0.1	0.3	0.3	0.4	0.5	0.6	0.8	0.5	0.6	0.4	0.2
82	0.4	0.8	1.2	1.5	1.3	0.7	0.7	0.7	0.6	0.4	0.2	0.1	0.2	0.2	0.4	0.4	0.5	0.6	0.8	1.0	0.7	0.8	0.5	0.3
81	0.4	1.2	1.4	1.8	1.6	0.9	0.9	0.9	0.7	0.6	0.2	0.2	0.2	0.3	0.5	0.5	0.6	0.8	0.9	1.8	1.1	1.1	0.8	0.5
80	0.6	1.5	1.7	1.9	1.8	1.0	1.0	0.9	0.8	0.7	0.3	0.2	0.3	0.5	0.6	0.8	0.7	0.9	1.1	1.9	1.6	1.5	1.1	0.8
79	1.3	1.8	2.0	1.8	1.8	1.1	1.4	1.1	0.9	1.0	0.4	0.4	0.6	0.7	0.8	1.0	0.8	1.2	1.3	1.8	2.0	1.8	1.5	1.1
78	1.6	1.4	1.6	1.4	1.5	1.3	1.5	1.3	1.2	1.4	0.5	0.8	0.9	1.3	1.5	1.4	0.9	1.4	1.5	1.9	2.2	1.3	1.6	1.4
77	1.9	1.0	1.2	0.9	1.0	1.6	1.7	1.5	1.4	1.5	0.9	1.1	1.1	1.8	1.7	1.5	1.1	1.6	1.5	1.8	1.8	1.7	1.6	1.9
76	0.6	0.6	0.7	0.5	0.6	1.8	1.8	1.9	1.8	2.1	1.6	1.5	1.5	1.9	1.6	1.7	1.3	1.4	1.1	1.4	1.2	1.3	0.6	0.5
75	0.2	0.2	0.3	0.4	0.5	1.5	1.5	2.1	2.2	2.4	2.4	2.0	1.8	1.9	1.2	1.1	1.3	1.7	1.0	1.1	0.8	0.7	0.2	0.2
74	0.0	0.0	0.2	0.2	0.4	1.1	1.1	1.7	1.7	2.3	2.5	2.5	2.1	1.9	0.8	0.7	1.0	1.4	0.6	0.5	0.5	0.4	0.0	0.0
73	0.0	0.0	0.0	0.2	0.3	0.7	0.6	1.0	1.0	1.5	2.5	2.2	2.0	1.3	0.5	0.5	0.7	0.7	0.5	0.4	0.3	0.0	0.0	0.0
72	0.0	0.0	0.0	0.2	0.3	0.5	0.4	0.6	0.5	0.9	1.3	1.9	1.6	0.8	0.3	0.3	0.5	0.5	0.4	0.2	0.1	0.0	0.0	0.0
71	0.0	0.0	0.0	0.0	0.2	0.3	0.3	0.4	0.3	0.5	0.7	1.1	0.9	0.5	0.3	0.3	0.4	0.4	0.4	0.1	0.0	0.0	0.0	0.0
70	0.0	0.0	0.0	0.0	0.0	0.3	0.2	0.3	0.3	0.3	0.5	0.6	0.6	0.3	0.2	0.2	0.3	0.3	0.3	0.0	0.0	0.0	0.0	0.0
69	0.0	0.0	0.0	0.0	0.0	0.3	0.2	0.2	0.2	0.3	0.3	0.4	0.3	0.2	0.2	0.2	0.2	0.3	0.4	0.0	0.0	0.0	0.0	0.0
68	0.0	0.0	0.0	0.0	0.0	0.2	0.2	0.2	0.2	0.2	0.2	0.2	0.2	0.2	0.1	0.2	0.2	0.2	0.3	0.2	0.0	0.0	0.0	0.0
67	0.0	0.0	0.0	0.0	0.0	0.2	0.2	0.2	0.2	0.2	0.2	0.1	0.1	0.2	0.1	0.2	0.2	0.2	0.3	0.1	0.0	0.0	0.0	0.0
66	0.0	0.0	0.0	0.0	0.0	0.2	0.2	0.2	0.2	0.2	0.1	0.1	0.1	0.2	0.1	0.2	0.2	0.2	0.3	0.0	0.0	0.0	0.0	0.0
65	0.0	0.0	0.0	0.0	0.0	0.2	0.2	0.2	0.2	0.2	0.1	0.1	0.1	0.1	0.1	0.2	0.2	0.2	0.2	0.0	0.0	0.0	0.0	0.0
64	0.0	0.0	0.0	0.0	0.0	0.2	0.2	0.2	0.1	0.1	0.1	0.1	0.1	0.1	0.0	0.1	0.1	0.1	0.3	0.0	0.0	0.0	0.0	0.0
63	0.0	0.0	0.0	0.0	0.0	0.2	0.2	0.2	0.2	0.1	0.1	0.1	0.1	0.1	0.0	0.1	0.1	0.1	0.2	0.0	0.0	0.0	0.0	0.0
62	0.0	0.0	0.0	0.0	0.0	0.1	0.1	0.1	0.2	0.1	0.1	0.1	0.0	0.1	0.0	0.0	0.1	0.1	0.2	0.0	0.0	0.0	0.0	0.0
61	0.0	0.0	0.0	0.0	0.0	0.1	0.1	0.1	0.1	0.1	0.1	0.1	0.1	0.1	0.1	0.1	0.1	0.1	0.2	0.0	0.0	0.0	0.0	0.0
60	0.0	0.0	0.0	0.0	0.0	0.1	0.1	0.1	0.1	0.1	0.0	0.1	0.1	0.1	0.1	0.1	0.1	0.1	0.2	0.0	0.0	0.0	0.0	0.0
59	0.0	0.0	0.0	0.0	0.0	0.1	0.1	0.1	0.1	0.1	0.1	0.0	0.1	0.1	0.1	0.0	0.1	0.1	0.2	0.0	0.0	0.0	0.0	0.0
58	0.0	0.0	0.0	0.0	0.0	0.1	0.1	0.1	0.1	0.1	0.1	0.1	0.0	0.1	0.1	0.1	0.1	0.1	0.1	0.0	0.0	0.0	0.0	0.0
57	0.0	0.0	0.0	0.0	0.0	0.1	0.1	0.1	0.1	0.1	0.0	0.1	0.1	0.1	0.1	0.0	0.0	0.0	0.0	0.0	0.0	0.0	0.0	0.0
56	0.0	0.0	0.0	0.0	0.0	0.1	0.1	0.1	0.1	0.0	0.0	0.0	0.0	0.0	0.0	0.0	0.0	0.0	0.1	0.0	0.0	0.0	0.0	0.0

Table B.1   Mean counts/pixel in 1-hour magnetic local time x 1 geomagnetic latitude bins for the Simple average image when AE < 100 nT.

Lat	12	13	14	15	16	17	18	19	20	21	22	23	00	01	02	03	04	05	06	07	08	09	10	11
90	0.0	0.0	0.0	0.0	0.0	0.0	0.0	0.0	0.0	0.0	0.0	0.0	0.0	0.0	0.0	0.0	0.0	0.0	0.0	0.0	0.0	0.0	0.0	0.0
89	0.0	0.0	0.0	0.0	0.0	0.0	0.0	0.0	0.0	0.0	0.0	0.0	0.0	0.0	0.0	0.0	0.0	0.0	0.1	0.0	0.0	0.0	0.0	0.0
88	0.1	0.1	0.1	0.1	0.1	0.1	0.1	0.1	0.1	0.1	0.1	0.1	0.1	0.1	0.1	0.1	0.1	0.1	0.1	0.1	0.1	0.1	0.1	0.1
87	0.1	0.2	0.2	0.2	0.1	0.1	0.1	0.2	0.1	0.1	0.1	0.1	0.1	0.1	0.1	0.1	0.1	0.1	0.1	0.1	0.1	0.4	0.1	0.1
86	0.2	0.5	0.5	0.4	0.2	0.2	0.2	0.3	0.2	0.2	0.1	0.0	0.1	0.1	0.1	0.1	0.2	0.1	0.2	0.2	0.2	0.7	0.2	0.2
85	0.3	0.6	0.6	0.7	0.3	0.3	0.3	0.4	0.3	0.3	0.1	0.1	0.1	0.2	0.1	0.1	0.2	0.2	0.5	0.4	0.3	1.0	0.5	0.5
84	0.4	0.8	0.9	1.1	0.6	0.6	0.5	0.5	0.4	0.3	0.2	0.1	0.2	0.2	0.1	0.1	0.4	0.2	0.5	0.5	0.6	1.2	0.8	0.7
83	0.8	1.3	1.3	1.3	0.8	0.9	0.7	0.8	0.6	0.3	0.2	0.2	0.2	0.1	0.1	0.2	0.4	0.4	0.7	0.6	0.8	1.8	1.0	0.9
82	1.0	1.7	1.5	1.5	1.3	1.1	0.9	0.9	0.7	0.4	0.3	0.2	0.2	0.2	0.3	0.5	0.6	0.6	0.8	0.8	1.2	1.9	1.0	1.3
81	1.3	1.1	1.7	1.7	1.4	1.5	1.0	0.8	0.8	0.4	0.4	0.2	0.2	0.2	0.4	0.5	0.6	0.5	0.9	1.0	1.4	2.0	1.8	1.9
80	1.7	1.6	1.5	1.5	1.6	1.2	0.8	0.8	0.7	0.7	0.7	0.3	0.3	0.3	0.5	0.6	0.6	0.6	1.0	1.6	1.9	1.8	1.3	1.5
79	1.1	1.4	1.8	1.2	1.2	1.3	0.9	0.9	0.8	0.8	1.6	0.5	0.4	0.4	0.6	0.7	0.7	0.8	1.2	1.5	1.7	0.7	1.7	1.1
78	0.9	1.1	0.8	1.1	1.1	0.1	0.9	1.1	1.2	1.0	2.4	1.7	0.8	0.7	1.2	0.8	0.9	0.9	1.4	1.6	1.4	0.5	0.5	0.8
77	0.8	0.9	0.6	1.0	1.9	1.2	1.0	1.5	1.3	1.4	2.9	2.6	1.5	1.3	1.3	1.0	0.8	1.2	1.4	1.6	0.8	0.4	0.5	0.6
76	0.7	0.7	0.5	0.7	0.7	1.0	1.1	1.5	1.7	1.8	1.1	2.4	2.2	1.8	1.4	1.1	1.2	1.2	1.9	1.3	0.6	0.3	0.2	0.3
75	0.4	0.7	0.4	0.6	0.6	0.9	1.1	1.3	1.7	1.8	1.1	1.5	2.4	2.0	1.3	1.5	1.2	0.8	0.7	1.7	0.6	0.2	0.0	0.1
74	0.2	0.5	0.4	0.4	0.4	0.6	0.6	1.0	1.5	1.7	0.6	0.8	2.0	2.1	0.8	1.3	0.8	0.6	0.7	0.7	0.4	0.1	0.0	0.0
73	0.0	0.2	0.3	0.3	0.4	0.4	0.5	0.7	1.3	1.1	0.4	0.3	1.4	1.2	0.6	1.8	0.6	0.6	0.7	0.6	0.4	0.0	0.0	0.0
72	0.0	0.0	0.2	0.2	0.3	0.4	0.3	0.5	0.5	0.7	0.1	0.2	0.6	0.7	0.4	0.7	0.6	0.4	0.6	0.5	0.2	0.0	0.0	0.0
71	0.0	0.0	0.1	0.2	0.3	0.3	0.3	0.4	0.3	0.5	0.1	0.1	0.4	0.5	0.4	0.5	0.5	0.4	0.5	0.4	0.3	0.0	0.0	0.0
70	0.0	0.0	0.1	0.3	0.2	0.3	0.3	0.3	0.3	0.3	0.1	0.1	0.3	0.3	0.2	0.4	0.4	0.3	0.4	0.4	0.2	0.0	0.0	0.0
69	0.0	0.0	0.0	0.3	0.2	0.3	0.2	0.2	0.2	0.2	0.1	0.1	0.2	0.3	0.2	0.4	0.3	0.2	0.4	0.3	0.1	0.0	0.0	0.0
68	0.0	0.0	0.0	0.2	0.0	0.3	0.2	0.2	0.2	0.2	0.1	0.1	0.1	0.2	0.1	0.2	0.2	0.2	0.3	0.3	0.1	0.0	0.0	0.0
67	0.0	0.0	0.0	0.3	0.1	0.3	0.2	0.1	0.1	0.1	0.0	0.0	0.1	0.1	0.1	0.2	0.2	0.2	0.3	0.3	0.1	0.0	0.0	0.0
66	0.0	0.0	0.0	0.2	0.2	0.3	0.1	0.2	0.2	0.1	0.0	0.0	0.0	0.1	0.1	0.1	0.2	0.2	0.3	0.3	0.0	0.0	0.0	0.0
65	0.0	0.0	0.0	0.3	0.3	0.3	0.2	0.2	0.1	0.0	0.0	0.0	0.0	0.1	0.0	0.1	0.2	0.2	0.3	0.2	0.0	0.0	0.0	0.0
64	0.0	0.0	0.0	0.2	0.2	0.3	0.2	0.1	0.1	0.1	0.0	0.0	0.0	0.1	0.0	0.1	0.2	0.0	0.3	0.0	0.0	0.0	0.0	0.0
63	0.0	0.0	0.0	0.1	0.3	0.0	0.0	0.2	0.2	0.0	0.0	0.0	0.0	0.0	0.0	0.2	0.2	0.0	0.0	0.0	0.0	0.0	0.0	0.0
62	0.0	0.0	0.0	0.0	0.0	0.0	0.0	0.1	0.1	0.0	0.0	0.0	0.0	0.0	0.0	0.0	0.2	0.0	0.0	0.0	0.0	0.0	0.0	0.0
61	0.0	0.0	0.0	0.0	0.0	0.0	0.0	0.0	0.0	0.0	0.0	0.0	0.0	0.0	0.0	0.0	0.0	0.0	0.0	0.0	0.0	0.0	0.0	0.0
60	0.0	0.0	0.0	0.0	0.0	0.0	0.0	0.0	0.0	0.0	0.0	0.0	0.0	0.0	0.0	0.0	0.0	0.0	0.0	0.0	0.0	0.0	0.0	0.0
59	0.0	0.0	0.0	0.0	0.0	0.0	0.0	0.0	0.0	0.0	0.0	0.0	0.0	0.0	0.0	0.0	0.0	0.0	0.0	0.0	0.0	0.0	0.0	0.0
58	0.0	0.0	0.0	0.0	0.0	0.0	0.0	0.0	0.0	0.0	0.0	0.0	0.0	0.0	0.0	0.0	0.0	0.0	0.0	0.0	0.0	0.0	0.0	0.0
57	0.0	0.0	0.0	0.0	0.0	0.0	0.0	0.0	0.0	0.0	0.0	0.0	0.0	0.0	0.0	0.0	0.0	0.0	0.0	0.0	0.0	0.0	0.0	0.0
56	0.0	0.0	0.0	0.0	0.0	0.0	0.0	0.0	0.0	0.0	0.0	0.0	0.0	0.0	0.0	0.0	0.0	0.0	0.0	0.0	0.0	0.0	0.0	0.0

Table B.2 Quadrant 1 mean counts/pixel in 1-hour magnetic local time x 1 geomagnetic latitude bins for AE < 100 nT.

Lat	12	13	14	15	16	17	18	19	20	21	22	23	00	01	02	03	04	05	06	07	08	09	10	11
90	0.1	0.1	0.0	0.0	0.0	0.0	0.0	0.0	0.0	0.0	0.1	0.0	0.0	0.0	0.0	0.0	0.0	0.0	0.0	0.0	0.0	0.0	0.0	0.0
89	0.2	0.3	0.1	0.1	0.2	0.2	0.0	0.0	0.0	0.0	0.0	0.1	0.0	0.0	0.1	0.0	0.1	0.1	0.0	0.1	0.1	0.1	0.1	0.1
88	0.0	0.2	0.0	0.1	0.0	0.5	0.1	0.1	0.1	0.0	0.1	0.0	0.0	0.0	0.1	0.1	0.1	0.0	0.3	0.4	0.2	0.2	0.0	0.1
87	0.0	0.2	0.0	0.0	0.1	0.2	0.3	0.2	0.1	0.1	0.1	0.2	0.1	0.1	0.4	0.4	0.2	0.6	0.4	0.9	0.5	0.4	0.3	0.4
86	0.3	0.3	0.7	0.5	0.5	0.3	0.5	0.5	0.3	0.1	0.1	0.1	0.1	0.3	0.3	0.5	0.5	0.5	0.5	0.7	0.8	1.1	0.5	0.7
85	0.2	0.5	0.4	0.5	0.8	0.4	0.7	0.5	0.3	0.0	0.2	0.3	0.1	0.1	0.1	0.5	1.3	0.2	0.4	1.6	0.1	1.4	1.3	1.3
84	0.5	0.3	0.7	0.0	0.7	1.1	0.6	1.1	0.0	0.3	0.3	0.1	0.1	0.3	0.3	1.2	1.0	1.0	1.1	1.3	0.7	1.9	0.8	1.4
83	1.5	0.7	0.5	0.7	0.9	1.3	1.0	1.7	0.7	0.4	0.4	0.2	0.2	0.4	0.2	1.4	0.8	2.6	1.6	1.6	1.3	2.7	1.2	3.1
82	1.2	1.4	1.1	0.9	1.4	0.6	0.2	1.3	0.6	0.6	0.3	0.1	0.3	1.3	0.4	3.0	2.1	1.8	1.9	1.9	3.8	3.1	2.4	5.3
81	1.2	2.3	1.1	1.6	0.6	0.7	0.7	0.8	0.7	0.3	0.7	0.4	0.5	0.4	1.5	1.1	2.0	1.6	0.7	1.5	3.6	4.4	2.5	4.9
80	4.1	3.2	0.8	1.2	0.8	0.4	0.5	1.0	3.6	1.2	1.7	0.2	0.6	0.3	3.2	1.8	1.9	1.3	1.8	3.2	2.0	3.6	4.8	3.6
79	5.4	4.1	1.8	3.4	0.5	0.6	1.0	0.7	2.7	1.7	1.6	0.3	0.6	0.6	1.9	1.6	2.7	2.3	3.2	3.0	5.0	5.5	3.6	3.4
78	1.9	3.4	3.4	2.7	1.3	0.9	2.4	0.6	2.4	1.1	0.8	0.4	0.7	0.3	2.0	2.5	4.6	3.5	2.9	2.9	2.6	4.9	3.6	1.2
77	1.8	3.4	5.7	4.0	2.5	0.5	3.3	0.6	1.1	1.6	1.4	1.1	0.8	0.6	2.5	3.3	2.8	2.8	2.9	2.0	1.2	2.7	0.8	1.3
76	1.7	2.0	3.6	3.3	1.6	1.2	3.0	1.6	1.3	0.7	1.6	1.1	0.6	0.6	3.4	4.9	1.9	2.6	3.9	0.9	1.2	2.6	1.7	1.4
75	1.5	1.8	3.0	1.9	2.8	2.4	1.9	2.9	1.9	1.9	0.8	2.1	1.9	1.5	3.7	2.0	0.9	1.0	1.6	0.4	0.7	2.4	0.7	0.8
74	1.7	1.2	2.5	1.3	1.5	2.5	0.9	3.6	2.1	1.3	1.7	1.1	0.9	1.9	4.5	1.7	0.9	1.3	2.0	0.6	0.4	1.5	1.3	0.5
73	1.3	1.1	1.2	1.5	0.7	1.6	0.5	2.1	2.4	3.0	1.7	2.7	2.7	1.7	2.3	1.2	0.6	0.6	0.8	0.6	0.0	1.1	1.0	0.2
72	0.4	1.3	1.1	0.7	0.5	1.8	0.5	1.2	2.5	3.5	2.7	3.7	3.7	2.9	1.1	0.3	0.4	0.5	0.7	1.0	0.6	1.0	1.0	0.1
71	0.2	1.3	1.2	1.5	0.7	0.7	0.2	0.5	0.4	3.1	3.5	3.3	3.3	4.3	0.8	0.4	0.1	0.7	0.9	1.1	0.5	1.3	0.7	0.2
70	0.2	1.2	1.1	0.4	0.4	0.5	0.3	0.6	4.4	1.9	1.9	2.1	2.2	3.9	0.2	0.4	0.3	0.5	0.4	0.7	1.2	1.1	0.7	0.3
69	0.1	0.2	0.7	0.9	0.7	0.6	0.4	0.3	2.0	0.7	1.3	1.5	1.3	2.5	0.1	0.2	0.4	0.3	0.8	0.3	1.0	1.1	0.2	0.2
68	0.4	0.6	1.5	0.5	0.4	0.7	0.1	0.3	1.1	0.8	1.0	0.8	1.2	1.7	0.3	0.4	0.2	0.1	0.5	0.4	1.5	0.2	0.1	0.2
67	0.0	0.4	0.9	0.3	0.5	0.6	0.4	0.3	1.0	0.7	0.8	0.3	0.5	0.2	0.1	0.3	0.3	0.3	0.2	1.0	1.0	0.1	0.1	0.7
66	0.0	0.6	1.2	0.9	0.4	0.1	0.1	0.3	0.5	0.3	0.4	0.1	0.1	0.4	0.3	0.0	0.0	0.3	0.5	0.6	1.7	0.0	0.0	0.1
65	0.2	0.1	0.8	0.9	0.6	0.2	0.3	0.1	0.4	0.2	0.0	0.3	0.0	0.3	0.1	0.4	0.1	0.0	0.3	0.1	0.8	0.0	0.0	0.8
64	0.2	0.2	0.7	0.8	0.1	0.0	0.1	0.2	0.3	0.1	0.3	0.0	0.0	0.0	0.1	0.3	0.3	0.2	0.0	0.5	0.4	0.5	0.2	0.2
63	0.0	0.0	0.2	0.8	0.5	0.3	0.2	0.1	0.3	0.2	0.1	0.0	0.0	0.1	0.1	0.0	0.1	0.1	0.4	0.2	1.0	0.1	0.0	0.2
62	0.1	0.1	1.2	0.6	0.6	0.1	0.1	0.0	0.3	0.3	0.2	0.0	0.0	0.0	0.1	0.4	0.3	0.3	0.2	0.5	1.1	0.2	0.2	0.2
61	0.2	0.1	0.3	1.4	0.3	0.2	0.0	0.1	0.2	0.2	0.0	0.0	0.0	0.0	0.1	0.2	0.4	0.1	0.6	0.4	0.5	0.0	0.1	0.0
60	0.3	0.3	0.1	1.2	0.4	0.2	0.3	0.2	0.0	0.0	0.1	0.0	0.0	0.0	0.1	0.4	0.2	0.3	0.1	0.3	0.1	0.5	0.2	0.7
59	1.1	0.0	0.3	0.3	0.1	0.2	0.1	0.1	0.3	0.3	0.1	0.0	0.0	0.0	0.0	0.3	0.4	0.3	0.3	0.6	0.7	0.1	0.0	0.1
58	0.5	0.7	0.3	0.0	0.3	0.2	0.0	0.1	0.0	0.0	0.0	0.0	0.0	0.0	0.0	0.3	0.2	0.1	0.3	0.1	0.8	0.2	0.2	0.8
57	0.0	0.0	0.0	0.0	0.0	0.0	0.0	0.0	0.0	0.0	0.0	0.0	0.0	0.0	0.0	0.0	0.0	0.0	0.0	0.0	0.0	0.0	0.0	0.0
56	0.0	0.0	0.0	0.0	0.0	0.0	0.0	0.0	0.0	0.0	0.0	0.0	0.0	0.0	0.0	0.0	0.0	0.0	0.0	0.0	0.0	0.0	0.0	0.0
Lat	12	13	14	15	16	17	18	19	20	21	22	23	00	01	02	03	04	05	06	07	08	09	10	11

Table B.3 Quadrant 2 mean counts/pixel in 1-hour magnetic local time x 1 geomagnetic latitude bins for AE < 100 nT.

	11	10	09	08	07	06	05	04	03	02	01	00	23	22	21	20	19	18	17	16	15	14	13	12
90	0.0	0.0	0.0	0.0	0.0	0.0	0.1	0.0	0.0	0.0	0.0	0.0	0.0	0.0	0.0	0.1	0.0	0.1	0.0	0.0	0.0	0.0	0.0	0.0
89	0.0	0.0	0.0	0.0	0.0	0.0	0.1	0.0	0.0	0.1	0.0	0.1	0.0	0.1	0.0	0.1	0.0	0.1	0.0	0.0	0.0	0.0	0.0	0.0
88	0.0	0.0	0.1	0.1	0.1	0.1	0.1	0.1	0.1	0.1	0.0	0.1	0.1	0.1	0.1	0.1	0.1	0.1	0.1	0.1	0.1	0.1	0.1	0.1
87	0.1	0.1	0.0	0.0	0.1	0.1	0.1	0.0	0.1	0.1	0.1	0.1	0.1	0.1	0.1	0.1	0.1	0.2	0.1	0.1	0.1	0.1	0.1	0.1
86	0.1	0.1	0.1	0.1	0.1	0.2	0.1	0.1	0.1	0.1	0.1	0.2	0.1	0.1	0.1	0.1	0.2	0.3	0.1	0.2	0.1	0.1	0.1	0.1
85	0.1	0.1	0.1	0.2	0.1	0.3	0.1	0.2	0.2	0.1	0.1	0.1	0.1	0.1	0.1	0.2	0.6	0.4	0.4	0.4	0.6	0.6	0.4	0.4
84	0.1	0.1	0.1	0.2	0.2	0.4	0.3	0.2	0.2	0.1	0.2	0.1	0.1	0.2	0.2	0.4	0.7	0.6	0.5	0.7	0.8	0.8	0.6	0.6
83	0.2	0.2	0.2	0.2	0.3	0.5	0.3	0.3	0.3	0.2	0.3	0.2	0.2	0.2	0.3	0.6	0.9	0.8	0.9	1.2	0.8	1.2	0.8	0.8
82	0.4	0.3	0.4	0.4	0.6	0.9	0.7	0.4	0.4	0.3	0.4	0.4	0.4	0.4	0.6	0.8	0.8	1.1	1.3	1.4	0.8	1.2	1.0	1.0
81	0.5	0.5	0.7	0.8	0.9	1.1	1.0	0.7	0.6	0.5	0.7	0.4	0.6	0.5	0.6	0.9	0.8	1.2	1.7	1.4	1.4	1.4	1.4	1.6
80	1.0	1.1	1.0	1.4	1.3	1.6	1.3	0.8	0.7	0.8	1.0	0.7	0.7	0.7	0.9	1.1	1.0	1.3	1.8	1.9	1.7	1.8	1.7	1.5
79	1.6	1.5	1.8	2.4	2.5	1.6	1.3	0.9	0.6	0.8	1.9	1.9	1.2	1.3	1.1	1.1	1.1	1.3	1.5	2.0	2.0	2.3	1.8	0.9
78	1.1	1.3	2.0	3.6	3.4	2.9	1.4	0.8	0.7	1.3	2.8	2.7	2.4	1.8	1.5	1.8	1.8	1.7	2.3	2.5	2.8	1.9	1.8	1.6
77	0.7	0.8	1.9	2.2	3.6	2.2	1.4	0.9	0.6	2.1	2.5	2.1	2.5	2.7	1.6	2.7	2.5	2.3	2.4	2.6	2.1	1.5	1.1	1.5
76	0.5	0.6	0.7	1.2	2.6	1.9	2.0	0.8	1.1	1.8	1.2	1.8	2.1	2.5	1.8	2.0	1.9	2.2	1.8	3.1	1.1	1.2	1.1	0.9
75	0.2	0.5	0.6	0.6	1.9	1.7	1.7	1.3	1.4	0.5	0.6	1.0	1.6	1.6	2.7	2.7	1.2	1.3	1.2	1.4	1.5	1.5	0.9	0.6
74	0.1	0.2	0.2	0.4	0.8	1.0	1.0	1.7	1.6	0.4	0.4	0.8	0.7	1.8	1.8	2.0	0.7	0.7	0.8	0.8	0.5	1.0	0.6	0.4
73	0.0	0.2	0.1	0.0	0.7	0.7	0.9	1.4	1.0	0.2	0.2	0.4	0.4	0.7	1.6	1.0	0.4	0.6	0.4	0.6	0.7	0.6	0.4	0.3
72	0.0	0.0	0.0	0.1	0.4	0.6	0.6	0.6	0.6	0.1	0.1	0.2	0.3	0.4	1.1	0.4	0.3	0.5	0.3	0.5	0.4	0.3	0.2	0.1
71	0.0	0.0	0.0	0.0	0.3	0.5	0.4	0.4	0.4	0.1	0.1	0.1	0.2	0.3	0.3	0.3	0.3	0.4	0.3	0.5	0.5	0.2	0.1	0.0
70	0.0	0.1	0.0	0.0	0.3	0.4	0.4	0.3	0.4	0.2	0.1	0.2	0.1	0.2	0.2	0.2	0.2	0.3	0.3	0.5	0.4	0.1	0.1	0.0
69	0.0	0.0	0.0	0.0	0.2	0.3	0.2	0.2	0.2	0.2	0.2	0.2	0.1	0.2	0.2	0.2	0.3	0.2	0.3	0.4	0.3	0.0	0.0	0.0
68	0.0	0.0	0.0	0.0	0.2	0.2	0.2	0.2	0.2	0.2	0.1	0.1	0.1	0.2	0.2	0.2	0.2	0.2	0.3	0.3	0.2	0.0	0.0	0.0
67	0.1	0.0	0.0	0.0	0.1	0.2	0.2	0.2	0.2	0.1	0.2	0.0	0.1	0.1	0.1	0.2	0.2	0.2	0.2	0.3	0.1	0.0	0.0	0.0
66	0.1	0.1	0.0	0.0	0.1	0.2	0.2	0.2	0.2	0.2	0.2	0.1	0.1	0.1	0.1	0.2	0.2	0.2	0.2	0.2	0.0	0.0	0.0	0.0
65	0.1	0.0	0.0	0.0	0.1	0.2	0.2	0.2	0.1	0.1	0.2	0.1	0.1	0.1	0.1	0.2	0.3	0.2	0.2	0.2	0.0	0.0	0.0	0.0
64	0.1	0.0	0.0	0.0	0.1	0.2	0.2	0.1	0.1	0.1	0.2	0.1	0.1	0.1	0.1	0.2	0.2	0.2	0.2	0.2	0.1	0.1	0.0	0.0
63	0.1	0.0	0.1	0.0	0.1	0.2	0.1	0.1	0.1	0.1	0.1	0.0	0.0	0.1	0.1	0.2	0.2	0.2	0.1	0.0	0.1	0.1	0.0	0.0
62	0.1	0.0	0.0	0.0	0.0	0.2	0.2	0.2	0.1	0.1	0.2	0.1	0.0	0.0	0.0	0.2	0.2	0.2	0.2	0.0	0.0	0.0	0.1	0.1
61	0.1	0.1	0.0	0.0	0.0	0.3	0.2	0.2	0.2	0.1	0.1	0.0	0.1	0.0	0.0	0.2	0.2	0.2	0.3	0.0	0.0	0.1	0.1	0.1
60	0.1	0.0	0.0	0.0	0.1	0.2	0.2	0.1	0.2	0.1	0.1	0.0	0.0	0.1	0.1	0.1	0.2	0.1	0.2	0.0	0.0	0.0	0.1	0.3
59	0.1	0.0	0.0	0.0	0.1	0.3	0.2	0.1	0.1	0.1	0.1	0.0	0.1	0.1	0.1	0.2	0.1	0.2	0.2	0.0	0.0	0.0	0.0	0.4
58	0.1	0.0	0.0	0.0	0.0	0.2	0.2	0.2	0.1	0.1	0.1	0.1	0.1	0.1	0.1	0.1	0.2	0.2	0.2	0.0	0.0	0.1	0.1	0.1
57	0.1	0.1	0.0	0.0	0.1	0.1	0.1	0.1	0.1	0.1	0.1	0.1	0.1	0.1	0.1	0.1	0.2	0.0	0.0	0.0	0.0	0.0	0.1	0.1
56	0.2	0.1	0.1	0.0	0.1	0.2	0.1	0.1	0.1	0.1	0.0	0.1	0.0	0.0	0.0	0.0	0.0	0.0	0.0	0.0	0.0	0.0	0.0	0.0
	11	10	09	08	07	06	05	04	03	02	01	00	23	22	21	20	19	18	17	16	15	14	13	12

Table B.4 Quadrant 3 mean counts/pixel in 1-hour magnetic local time x 1 geomagnetic latitude bins for AE < 100 nT.

Lat	12	13	14	15	16	17	18	19	20	21	22	23	00	01	02	03	04	05	06	07	08	09	10	11
90	0.0	0.0	0.0	0.0	0.0	0.0	0.0	0.0	0.0	0.0	0.0	0.0	0.0	0.0	0.0	0.0	0.0	0.0	0.0	0.0	0.0	0.0	0.0	0.0
89	0.0	0.0	0.0	0.0	0.0	0.0	0.0	0.0	0.0	0.0	0.0	0.0	0.0	0.0	0.0	0.0	0.0	0.0	0.0	0.0	0.0	0.0	0.0	0.0
88	0.0	0.1	0.1	0.1	0.1	0.1	0.1	0.1	0.1	0.0	0.0	0.0	0.0	0.0	0.0	0.0	0.1	0.1	0.1	0.0	0.0	0.0	0.0	0.0
87	0.1	0.1	0.1	0.1	0.1	0.1	0.2	0.1	0.1	0.1	0.1	0.1	0.0	0.0	0.0	0.1	0.1	0.1	0.1	0.0	0.0	0.0	0.0	0.0
86	0.1	0.1	0.2	0.2	0.2	0.1	0.4	0.2	0.2	0.1	0.1	0.1	0.1	0.0	0.1	0.1	0.2	0.1	0.1	0.0	0.0	0.0	0.0	0.0
85	0.1	0.3	0.3	0.4	0.5	0.4	0.5	0.2	0.2	0.2	0.2	0.2	0.1	0.0	0.1	0.1	0.2	0.2	0.2	0.1	0.1	0.1	0.1	0.1
84	0.3	0.4	0.4	0.5	0.6	0.5	0.6	0.4	0.4	0.2	0.5	0.4	0.1	0.0	0.1	0.2	0.2	0.2	0.4	0.1	0.2	0.1	0.1	0.1
83	0.6	0.7	0.7	0.6	0.7	0.6	0.8	0.7	0.6	0.4	0.8	0.7	0.2	0.1	0.2	0.2	0.3	0.5	0.5	0.2	0.3	0.3	0.2	0.1
82	0.9	1.4	0.8	0.9	0.8	0.9	1.0	0.6	0.7	0.5	0.9	1.0	0.5	0.2	0.3	0.3	0.4	0.7	0.6	0.3	0.4	0.4	0.3	0.2
81	1.2	1.8	1.7	1.2	1.2	1.1	1.1	0.8	0.7	0.8	1.1	1.4	0.8	0.4	0.3	0.4	0.5	0.8	0.8	0.5	0.7	0.6	0.3	0.2
80	1.1	1.4	2.1	1.5	1.5	1.5	1.4	0.9	0.8	0.9	1.4	1.4	1.2	0.5	0.4	0.6	0.8	1.1	1.0	0.9	1.0	0.9	0.7	0.4
79	1.0	0.6	2.0	1.8	1.8	1.8	1.5	0.9	0.9	0.9	1.7	1.2	1.2	0.5	0.4	1.0	1.1	1.3	1.3	1.2	1.4	1.3	1.2	0.8
78	0.3	0.2	1.1	1.7	1.8	1.7	1.4	1.2	1.1	1.4	2.5	1.8	1.3	0.7	0.6	1.2	1.1	1.5	1.2	1.5	1.7	1.7	1.7	1.1
77	0.0	0.0	0.6	1.5	1.7	1.4	1.1	1.5	1.3	1.5	2.2	2.0	1.7	1.4	1.4	1.2	1.0	0.8	1.0	1.5	1.8	1.5	1.1	1.1
76	0.0	0.0	0.2	1.6	1.0	1.2	0.7	1.5	1.5	1.7	2.3	2.8	1.8	1.6	1.6	1.2	0.7	0.4	0.5	1.4	0.7	0.3	0.4	1.6
75	0.0	0.0	0.0	0.3	0.8	0.6	0.5	1.3	1.7	1.6	2.9	2.6	1.5	1.4	1.3	0.7	0.5	0.3	0.4	1.0	0.4	0.1	0.0	0.2
74	0.0	0.0	0.0	0.2	0.4	0.5	0.4	1.4	1.6	2.1	1.4	1.3	1.2	1.5	1.1	0.6	0.4	0.2	0.3	0.7	0.1	0.0	0.0	0.0
73	0.0	0.0	0.0	0.0	0.3	0.3	0.3	0.9	1.1	1.8	1.1	0.9	0.7	1.8	0.8	0.2	0.2	0.1	0.2	0.3	0.0	0.0	0.0	0.0
72	0.0	0.0	0.0	0.0	0.3	0.3	0.2	0.5	0.9	1.6	0.6	0.5	0.4	0.8	0.3	0.2	0.2	0.1	0.2	0.1	0.0	0.0	0.0	0.0
71	0.0	0.0	0.0	0.0	0.2	0.3	0.2	0.4	0.4	1.0	0.4	0.3	0.3	0.5	0.3	0.2	0.1	0.1	0.2	0.1	0.0	0.0	0.0	0.0
70	0.0	0.0	0.0	0.0	0.2	0.3	0.2	0.3	0.3	0.4	0.3	0.2	0.2	0.3	0.2	0.1	0.1	0.1	0.2	0.0	0.0	0.0	0.0	0.0
69	0.0	0.0	0.0	0.0	0.1	0.3	0.2	0.2	0.2	0.3	0.2	0.1	0.1	0.2	0.2	0.1	0.1	0.0	0.1	0.0	0.0	0.0	0.0	0.0
68	0.0	0.0	0.0	0.0	0.0	0.2	0.2	0.2	0.2	0.3	0.2	0.1	0.1	0.1	0.1	0.1	0.0	0.0	0.1	0.0	0.0	0.0	0.0	0.0
67	0.0	0.0	0.0	0.0	0.0	0.3	0.2	0.2	0.2	0.2	0.2	0.1	0.0	0.1	0.1	0.0	0.0	0.0	0.0	0.0	0.0	0.0	0.0	0.0
66	0.0	0.0	0.0	0.0	0.0	0.3	0.2	0.2	0.2	0.2	0.1	0.0	0.0	0.0	0.1	0.0	0.0	0.0	0.0	0.0	0.0	0.0	0.0	0.0
65	0.0	0.0	0.0	0.0	0.0	0.0	0.0	0.2	0.2	0.2	0.1	0.0	0.0	0.0	0.0	0.0	0.0	0.0	0.0	0.0	0.0	0.0	0.0	0.0
64	0.0	0.0	0.0	0.0	0.0	0.0	0.0	0.2	0.2	0.2	0.0	0.0	0.0	0.0	0.0	0.0	0.0	0.0	0.0	0.0	0.0	0.0	0.0	0.0
63	0.0	0.0	0.0	0.0	0.0	0.0	0.0	0.2	0.0	0.1	0.0	0.0	0.0	0.0	0.0	0.0	0.0	0.0	0.0	0.0	0.0	0.0	0.0	0.0
62	0.0	0.0	0.0	0.0	0.0	0.0	0.0	0.0	0.0	0.1	0.0	0.0	0.0	0.0	0.0	0.0	0.0	0.0	0.0	0.0	0.0	0.0	0.0	0.0
61	0.0	0.0	0.0	0.0	0.0	0.0	0.0	0.0	0.0	0.0	0.0	0.0	0.0	0.0	0.0	0.0	0.0	0.0	0.0	0.0	0.0	0.0	0.0	0.0
60	0.0	0.0	0.0	0.0	0.0	0.0	0.0	0.0	0.0	0.0	0.0	0.0	0.0	0.0	0.0	0.0	0.0	0.0	0.0	0.0	0.0	0.0	0.0	0.0
59	0.0	0.0	0.0	0.0	0.0	0.0	0.0	0.0	0.0	0.0	0.0	0.0	0.0	0.0	0.0	0.0	0.0	0.0	0.0	0.0	0.0	0.0	0.0	0.0
58	0.0	0.0	0.0	0.0	0.0	0.0	0.0	0.0	0.0	0.0	0.0	0.0	0.0	0.0	0.0	0.0	0.0	0.0	0.0	0.0	0.0	0.0	0.0	0.0
57	0.0	0.0	0.0	0.0	0.0	0.0	0.0	0.0	0.0	0.0	0.0	0.0	0.0	0.0	0.0	0.0	0.0	0.0	0.0	0.0	0.0	0.0	0.0	0.0
56	0.0	0.0	0.0	0.0	0.0	0.0	0.0	0.0	0.0	0.0	0.0	0.0	0.0	0.0	0.0	0.0	0.0	0.0	0.0	0.0	0.0	0.0	0.0	0.0

Table B.5 Quadrant 4 mean counts/pixel in 1-hour magnetic local time x 1 geomagnetic latitude bins for AE < 100 nT.

REFERENCES

Akasofu, S.I., Auroral phenomena, in *Auroral Physics*, ed. by C.-I. Meng, M.J. Rycroft and L.A. Frank, 3-12, Cambridge University Press: Cambridge, England, 1991.

Akasofu, S.I., *Polar and Magnetospheric Substorms*, D. Reidel Publishing Company, Dordrecht, Holland, 1968.

Akasofu, S.I., The development of the auroral substorm, *Planetary Space Sci.*, 12, 273-282, 1964.

Craven, J.D., and L.A. Frank, Diagnosis of auroral dynamics using global auroral imaging with emphasis on large-scale evolution, in *Auroral Physics*, ed. by C.-I. Meng, M.J. Rycroft and L.A. Frank, 273-288, Cambridge University Press: Cambridge, England, 1991.

Davis, N., *The Aurora Watchers Handbook*, University of Alaska Press, Fairbanks, AK, 1992.

Eather, R.H., *Majestic Lights--The Aurora in Science, History, and the Arts*, Amer. Geophys. Union, Washington, DC, 1980.

Feldman, P.D., and E.P. Gentieu, The ultraviolet spectrum of an aurora 530-1520 Å, *J. Geophys. Res.*, 87, 2453-2458, 1982.

Frank, L.A., and J.D. Craven, Imaging results from Dynamics Explorer, *Rev. Geophys.*, 26(2),249-283,1988.

Frank, L.A., J.D. Craven, K.L. Ackerson, M.R. English, R.H. Eather and R.L. Carovillano, Global auroral imaging instrumentation for the Dynamics Explorer mission, *Space Sci. Instrum.*, 5, 369-393, 1981.

Fukushima, N. and J. Bartels, A Q-index for the geomagnetic activity in quarter-hourly intervals, *Abh. Akad. Wiss. Göttingen Math. Phys. Kl.*, 2, 36, 1956.

Gorney, D.J., Overview of auroral spatial scales, in *Auroral Physics*, ed. by C.-I. Meng, M.J. Rycroft and L.A. Frank, 325-334, Cambridge University Press: Cambridge, England, 1991.

Hardy, D.A., M.S. Gussenhoven and E. Holeman, A statistical model of auroral electron precipitation, *J. Geophys. Res.*, 90, 4229-4248, 1985.

Hedin, A.E., Extension of the MSIS thermosphere model into the middle and lower atmosphere, *J. Geophys. Res.*, 96, 1159-1172, 1991.

Holzworth, R.H. and C.-I. Meng, Mathematical representation of the auroral oval, *Geophys. Res. Lett.*, 2, 377-380, 1975.

Hoffman, R.A., and E.R. Schmerling, Dynamics explorer program: an overview, *Space Sci. Instrum.*, 5, 345-348, 1981.

Iijima, T. and T.A. Potemra, The relationship between interplanetary quantities and Birkeland current densities, *Geophys. Res. Lett.*, 9, 442-445, 1982.

Iijima, T. and T.A. Potemra, Large-scale characteristics of field-aligned currents associated with substorms, *J. Geophys. Res.*, 83, 599-615, 1978.

Lummerzheim, D., and J. Lilensten, Electron transport and energy degradation in the ionosphere: evaluation of the numerical solution, comparison with laboratory experiments and auroral observations, *Ann. Geophys.*, accepted for publication 1994.

Lummerzheim, D., M.H. Rees, J.D. Craven and L.A. Frank, Ionospheric conductances derived from DE-1 images, *J. Atmos. Terr. Phys.*, 53, 281-292, 1991.

Makita, K., and C.-I. Meng, Long-period polar rain variations, solar wind and hemispherically symmetric polar rain, *J. Geophys. Res.*, 92, 7,381-7,393, 1987.

Mayaud, Pierre N., *Derivation, Meaning, and Use of Geomagnetic Indices*, Amer. Geophys. Union, Washington, DC, 1980.

Meng, C.-I., and H.W. Kroehl, Intense uniform precipitation of low-energy electrons over the polar cap, *J. Geophys. Res.*, 82, 2,305-2,313, 1977.

Meier, R.R., and D.J. Strickland, Auroral emission processes and remote sensing, in *Auroral Physics*, ed. by C.-I. Meng, M.J. Rycroft and L.A. Frank, 37-49, Cambridge University Press: Cambridge, England, 1991.

Newell, P.T., and C.-I. Meng, Mapping the dayside ionosphere to the magnetosphere according to particle precipitation characteristics, *Geophys. Res. Lett.*, 609-612, 1992.

Newell, P.T., C.-I. Meng and D.A. Hardy, Overview of electron and ion precipitation in the auroral oval, in *Auroral Physics*, ed. by C.-I. Meng, M.J. Rycroft and L.A. Frank, 85-95, Cambridge University Press: Cambridge, England, 1991.

Nicholas, A.C., Spatial and temporal variations of the FUV dayglow with geomagnetic activity, Masters Thesis, University of Alaska Fairbanks, 1993.

Rees, M.H., *Physics and Chemistry of the Upper Atmosphere*, Cambridge Press, Cambridge, England, 1989.

Rees, M.H., D. Lummerzheim, R.G. Roble, J.D. Winningham, J.D. Craven and L.A. Frank, Auroral energy deposition rate, characteristic electron energy, and ionospheric parameters derived from Dynamics Explorer 1 images, *J. Geophys. Res.*, 93, 12,841-12,860, 1988.

Rees, M.H. and D. Luckey, Auroral electron energy derived from ratio of spectroscopic emissions--1. model computations, *J. Geophys. Res.*, 79, 1974.

Robinson, R.M., R.R. Vondrak, J.D. Craven, L.A. Frank and K. Miller, A comparison of ionospheric conductances and auroral luminosity's observed simultaneously with the Chatinika radar and the DE 1 auroral imagers, *J. Geophys. Res*, 94, 5383-5396, 1989.

Rostoker, G., Overview of observations and models of auroral substorms, in *Auroral Physics*, ed. by C.-I. Meng, M.J. Rycroft and L.A. Frank, 257-271, Cambridge University Press: Cambridge, England, 1991.

Sojka, J.J., M. Bowline, R.W. Schunk, J.D. Craven, L.A. Frank, J.R. Sharber, J.D. Winningham and L.H. Brace, Ionospheric simulation compared with Dynamics Explorer observations for November 22, 1981, *J. Geophys. Res.*, 97, 1245-1256, 1992.

Spiro, R.W., P.H. Reiff and L.J. Maher, Jr., Precipitating electron energy flux and auroral zone conductances--an empirical model, *J. Geophys. Res.*, 87, 8215-8227, 1982.

Stringer, W., and L. Schreurs, *Understanding the Aurora*, Geophysical Institute, Fairbanks, AK, 1975.

Wallace, J.M. and P.V. Hobbs, *Atmospheric Science--An Introductory Survey*, Academic Press, New York, NY, 1977.